ANALYSIS OF MECHANICAL BEHAVIOR OF HIGH PERFORMANCE CEMENT BASED COMPOSITE SLABS UNDER IMPACT LOADING

A THESIS SUBMITTED TO
THE GRADUATE SCHOOL OF NATURAL AND APPLIED
SCIENCES
OF
MIDDLE EAST TECHNICAL UNIVERSITY

BY

AZİZE CEREN SATIOĞLU

IN PARTIAL FULFILLMENT OF THE REQUIREMENTS
FOR
THE DEGREE OF MASTER OF SCIENCE
IN
CIVIL ENGINEERING

SEPTEMBER 2009

Approval of the thesis:

ANALYSIS OF MECHANICAL BEHAVIOR OF HIGH PERFORMANCE CEMENT BASED COMPOSITE SLABS UNDER IMPACT LOADING.

submitted by **AZİZE CEREN SATIOĞLU** in partial fulfillment of the requirements for the degree of **Master of Science in Civil Engineering Department, Middle East Technical University** by,

Prof. Dr. Canan Özgen _____
Dean, Graduate School of **Natural and Applied Sciences**

Prof.Dr. Güney Özcebe _____
Head of Department, **Civil Engineering**

Prof. Dr. Polat Gülkan _____
Supervisor, **Civil Engineering Dept, METU**

Examining Committee Members

Prof. Dr. Mehmet Utku _____
Civil Engineering Dept., METU

Prof. Dr. Polat Gülkan _____
Civil Engineering Dept., METU

Prof. Dr. Turgut Tokdemir _____
Engineering Sciences Dept., METU

Assoc. Prof. Dr. Ahmet Yakut _____
Civil Engineering Dept., METU

Asst. Prof. Dr. Özgür Kurç _____
Civil Engineering Dept., METU

Date: _____

I hereby declare that all information in this document has been obtained and presented in accordance with academic rules and ethical conduct. I also declare that, as required by these rules and conduct, I have fully cited and referenced all material and results that are not original to this work.

Name, Last name : Azize Ceren SATIOĞLU

Signature :

ABSTRACT

ANALYSIS OF MECHANICAL BEHAVIOR OF HIGH PERFORMANCE CEMENT BASED COMPOSITE SLABS UNDER IMPACT LOADING

Satıoğlu, Azize Ceren

M.S., Department of Civil Engineering

Supervisor: Prof. Dr. Polat Gülkan

Studies on the behavior of steel fiber reinforced concrete (SFRC) and slurry infiltrated fibrous concrete (SIFCON) to impact loading have started in recent years. Using these relatively new materials, higher values of tensile and compressive strength can be obtained with greater fracture toughness and energy absorption capacity, and therefore they carry a considerable importance in the design of protective structures. In this thesis, computational analyses concerning impact loading effect on concrete, steel fiber reinforced concrete (SFRC) and slurry infiltrated fibrous concrete (SIFCON) are conducted by the aid of ANSYS AUTODYN 11.0.0 software. In the simulations, the importance of the concrete compressive and tensile strengths, and the fracture energy, together with the target and projectile erosion parameters, were investigated on the response of concrete target and projectile residual velocity. The obtained results of the simulation trials on concrete, SFRC and SIFCON have been compared with the experimental outcomes of three concrete, two SFRC and two SIFCON specimens in terms of deformed target crater radius, depth volume and striking projectile residual velocities.

The simulation analyses have shown that, compressive as well as tensile strengths of the concrete, SFRC and SIFCON specimens are of great importance on the crater volume while erosion parameters have a significant effect on the projectile residual velocity. Simulation outcomes possess a higher accuracy for concrete simulations when comparisons are made with available experimental results. This accuracy deteriorates for SFRC and SIFCON specimens. It was further concluded that related material tests of the specimens must be available in order to obtain higher accuracy.

Key words: AUTODYN simulation, impact loading, crater volume, residual velocity, steel fiber reinforced concrete (SFRC), slurry infiltrated fibrous concrete (SIFCON).

ÖZ

YÜKSEK PERFORMANSLI ÇİMENTODAN İMAL EDİLMİŞ BETONARME DÖŞEMELERİN YÜKSEK HIZLI MERMİ ETKİSİ ALTINDAKİ HESABI

Satıoğlu, Azize Ceren

Yüksek Lisans, İnşaat Mühendisliği Bölümü

Tez Yöneticisi: Prof. Dr. Polat Gülkan

Eylül 2009, 192 sayfa

Çelik tel donatılı betonunun ve şerbet kıvamlı lifli betonun çarpma yüklemesi altındaki davranışları son yıllarda incelenmeye başlanmıştır. Göreceli olarak yeni olan bu malzemeler kullanımı daha eskiye dayananlara kıyasla daha yüksek basınç ve çekme dayanımlarına sahiptirler aynı zamanda enerji emme kapasiteleri ve kırılma sertlikleri de kullanımı eski olanlara oranla daha yüksektir. Bu yüksek lisans tezinde ANSYS AUTODYN 11.0.0. programının yardımıyla beton, çelik tel donatılı beton ve şerbet kıvamlı lifli betonun çarpma yüklemesi altındaki davranışlarını incelemek için analizler yapılmıştır. Simulasyonlarda, betonun basınç ve çekme dayanımlarının, kırılma enerjisinin, hedef ve mermi için kullanılan erozyon değerlerinin hedefte oluşan deformasyonları ve çarpma sonrası merminin hızını nasıl etkilediği incelenmiştir. Analiz sonuçları, simulasyonları yapılan deney sonuçlarıyla krater çapı, krater derinliği, krater hacmi ve çarpma sonrası mermi hızı parametreleri bakımından karşılaştırılmıştır.

Simulasyon sonuçları, beton, çelik tel donatılı beton ve şerbet kıvamlı lifli betonun basınç ve çekme dayanımlarının çarpma yüklemesi sonucunda oluşan krater hacmi açısından oldukça önemli olduğunu, merminin ve hedefin

modellenmesinde kullanılan erozyon değerlerinin ise merminin çarpma sonrası hızını büyük ölçüde etkilediğini göstermiştir. Deney sonuçlarıyla kıyaslandığında beton numumelerin simulasyon sonuçlarında daha yüksek tutarlılık görülmüştür. Ne var ki çelik donatılı beton ve şerbet kıvamlı betonda bu tutarlılık yüzdesi daha azdır. Deney ve analizlerin birbirine daha yakın sonuçlar verebilmesi için simulasyonlarda kullanılacak malzeme değerlerinin elde edilmesi amacıyla ilişkili testlerin yapılması gerektiği kanısına varılmıştır.

Anahtar Kelimeler: AUTODYN simulasyonu, çarpma yüklemesi, krater hacmi, çarpma sonrası hız, çelik tel donatılı beton, şerbet kıvamlı lifli beton.

To My Family

ACKNOWLEDGEMENT

TABLE OF CONTENTS

LIST OF FIGURES

FIGURES

LIST OF TABLES

TABLES

LIST OF SYMBOLS AND ABBREVIATIONS

SYMBOLS

Roman upper case letters

A	: basic yield stress at low strains
A_s	: shear surface of the concrete plug
B	: bright fiber
B	: represents effect of strain hardening
C	: glued fiber
D	: diameter of the projectile
D^*	: the missile caliber density
E	: Young's modulus of the target
E_c	: critical impact energy of the projectile
E_{cp}	: critical impact energy for perforation
E_{cs}	: critical impact energy for scabbing
E_m	: Young's modulus of the missile
F_R	: resisting force on the nose of the projectile
F_s	: total resistance force on the shear surface
G	: shear modulus
G_f	: fracture energy
$G_{F.NSC}$	: fracture energy of normal concrete
G_{Fmax}	: maximum calculated fracture energy
G_{Fmin}	: minimum calculated fracture energy
H_p	: plugging depth
I	: impact factor
I_1	: mean normal strain
J_2	: octahedral shearing strain.
K	: bulk modulus
K^*	: fracture toughness
L	: length of the projectile, loose fiber

L_f	: fiber length
L_R/L	: normalized residual projectile length
M	: projectile mass, moment
N	: low carbon fiber
N^*, N_2	: nose shape factor
P	: pressure
P/L	: normalized penetration depth
R	: hooked end fiber
S, S_1, S_2	: slope of the equation
T	: thickness of the target
T	: tension cut-off limit
T_H	: homologous temperature
$U, U_1, U_2,$	: shock wave speed
V_c	: critical impact velocity of the projectile
V_{BL}	: ballistic velocity limit
V_f	: volume fraction
VB	: low shock compression limit
VE	: high shock compression limit
$V_P, V0, V_0$	: projectile impact velocity
W	: weight of thr projectile
Xe/R	: ejection position scaled by the average final crater radius

Roman lower case letters

a	: characteristic size of aggregate
a_1	: rate of decrease in stress directly after tensile stress
a_2	: rate of stress decrease related to fiber length
c	: soundspeed
c_0	: soundspeed in the surrounding un-shocked medium
c_s	: bulk soundspeed of the solid, fully compacted material

c_{por}	: bulk soundspeed of the porous material
d	: diameter of the projectile
e	: perforation depth
e_0, e_1	: internal energy of the state ahead and behind the shock
e_0	: thickness of the target
f_c	: quasi-static uniaxial compressive strength of concrete
f_{cn}	: nominal strength of the concrete
f_t	: quasi-static uniaxial tensile strength of concrete
hs	: scabbing limit
k	: coefficient of the conical crater
k^*	: stability fraction
k^{**}	: positive material constants
l	: fiber length
l^*	: smallest mesh dimension
l_{el}	: crack extension length
n	: represents effect of strain hardening
n_{fibers}	: number of fibers per cm^2
p	: pressure
p	: missile perimeter
p_1, p_{10}	: ten pressure items for piecewise-linear plastic compaction path
r	: average percentage amount of reinforcement on ewef
s	: slope of the equation
s_{ij}	: deviatoric stress tensor.
$s_{mn} * de_m$	: rate of work due to distortion
$\dfrac{t}{d}$	: ratio of the target thickness and projectile diameter
v	: normal expansion velocity
v_s	: shock wave speed
v_0, v_1	: particle velocity of the state ahead and behind the shock

Greek upper case letters

$\varDelta t$	: time difference
$t+\varDelta t$	: next time step
Γ	: Gruneisen Gama coefficient

Greek lower case letters

α	: cone plugging angle
α^{**}	: dilatancy factor
α^{*}	: positive material constants
χ	: curvature
δ	: eleongation
δ_{ij}	: Kronecker delta
ε_{ij}	: strain in ij direction
ε_{kk}^{p}	: plastic volumetric strain
ε_{u}	: crack strain
ε_{p}	: effective plastic strain
ε_{p}^{*}	:normalized effective plastic strain rate
ϕ	: diameter of the reinforcement bar
θ	: obliquity
ρ	: density
$\rho_{ref,}\ \rho_{s,}$	: reference or solid density
$\rho_{1},\ \rho_{10}$	: ten density items for piecewise-linear plastic compaction path
$\rho_{0,}\ \rho_{1}^{*}$	: density of the state ahead and behind the shock
σ_{max}	: assumed maximum tensile stress
σ_{n}	: normal compressive stress
σ_{t}	: dynamic crushing stress
τ_{f}	: pure shear strength of concrete target
ξ	: crater depth

ABBREVIATIONS

ADI   : austempered ductile iron
AISI   : American Iron and Steel Industry
ASTM   : American Society for Testing and Materials
BHN   : Brinnel hardness number
CHR   : caliber head radius
DRC   : double reinforced concrete
EOS   : equation of state
ewef   : each-way-each-face
FRC   : fiber reinforced concrete
NDRC   : National Defence Research Committee
PCC   : plain cement concrete
RCC   : reinforced cement concrete
RHA   : rolled homogeneous armor
SFRC   : steel fiber reinforced concrete
SIFCON   : slurry infiltrated fiber concrete
TÜBİTAK   : Scientific and Technological Research Council of Turkey
UMIST   : University of Manchester Institute of Science and Technology
VPN   : Vickers pyramid number (hardness)

CHAPTER 1

INTRODUCTION

1.1   Statement of the Problem

The design of protective structures has gained considerable importance starting with the Second World War. With the awareness of the destructive effects of war on humans because of the inadequately designed structures for extreme loading, remedial studies were initiated. In TM5-855-1 (1986), the origins of these researches are given as the Effects of Impact and Explosions Program which was conducted in 1940s by the National Defense Research Committee (NDRC). The results of this project were published in 1949 originally as the army manual TM5-855-1. Nowadays, the possibility of terrorist attacks suggests inevitably that the work and study on this topic should be accelerated, with new methods and use of different materials in addition to existing ones.

One of the oldest materials of concern in this area was plain concrete. Both experimental and computational studies have been conducted in order to obtain knowledge about the behavior of this material under impact loading. Nowadays, in many computer codes that use the explicit integration, more than one material model for concrete material exists. It has captured attention because of its wide range usage in the construction world and due to being a versatile material. Concrete has advantages such as economy, higher compressive strength compared to primitive construction materials, and resistance to heat-temperature rise. Unfortunately it also has disadvantages such as being semi-brittle and weak in tension. By the help of construction technology development, the cure for these weaknesses was found by the use of reinforcement steel in concrete, thus

producing reinforced concrete. Since steel has the same strength both in compression and in tension, it seemed to be a good solution. In quasi-static type of loading which is the general case in civil engineering, it is a good solution but when the case is extreme loading, it was realized that, effect of these reinforcement bars appeared to be quite local instead of increasing the total resistance of the material.

Since overall structural resistance was the necessity, this homogeneity was tried to be gained by the addition of fibers to the reinforced concrete, obtaining FRC and by the use of a different material called slurry-infiltrated fibrous concrete (SIFCON). However, experimental and computational work done related to these materials are limited compared to plain or reinforced concrete studies, so there exists a necessity to improve both of them by increasing the number of experiments related with the impact loading response of the material and the introduction of new simulation techniques and material models which would reflect the experimental behavior in a more realistic way.

1.2 Previous Studies[1]

As might be expected in an area of wide civil and military application, there is a vast amount of literature on all aspects of impact loading, protective design and projectiles. Only a limited literature survey has been made of references directly related to the present dissertation, and this summary of the previous work in this area is given below:

Most of the researches related with protective design have their origin from TM5-855-1, "Fundamentals of Protective Design for Conventional Weapons", which was first published in 1949.This manual is the first document which collects design guidelines in a single handbook [TM5-855-1, (1986)]. The first publication of this manual also coincides the use of the "particle in cell" method at Los Alamos National Laboratory in 1950 with the birth of hydrocodes [Zukas, (2004)], the definition of which is given in the book of Klinkrad (2006) as

---

[1] Details of sources cited in this section are given in the "References" at the end.

programs which could solve a set of conservation equations together with adjoining equation of state (EOS) that include the shock phenomena under consideration of material response with the change of state. After the 1950s, several research programs have been carried out in terms of extreme loadings and their effects on structures. Unfortunately many of them are not in the public domain, so the ones that could be accessed for the thesis work will be mentioned here.

An important document that examines the theory of impact loading is the book "Impact-Theory and Physical Behavior of Colliding Solids" [Goldsmith, (1960)]. Later on, research concerning how ballistic performances of projectiles are affected by the change in the hardness and density parameters, are conducted for Ballistic Research Laboratories [Grabarek, (1971), (1973)]. Work of other researchers were also conducted for Ballistic Research Laboratories considering the effect of nose shape of the projectile on ballistic performance of it [Lambert and Jonas, (1976), Lambert, (1978)].

Another publication that had a crucial importance in the area of impact loading is the book "Impact Dynamics" [Zukas et al., (1982)]. The present dissertation has benefited greatly from this work with respect to the question of how the change in projectile and impact condition parameters would affect the ballistic performance. Two years later, studies concerning the revision and publishing of TM5-855-1 were accomplished. This is the version of TM5-855-1 that is referred to throughout the thesis [TM5-855-1, 1984].

While these developments were achieved in the ballistic performance field, in 1983 a new material named SIFCON was demonstrated to the Air Force Weapons Laboratory. Meanwhile, in 1985, Fanella and Naaman investigated the stress-strain properties of fiber reinforced mortar in compression [Fanella and Naaman, (1985)].

During the 1990's, studies concerning concrete technology and the response of this material to blast and impact loading accelerated. In 1992, Ezeldin and Balaguru studied the compression behavior of normal and high strength fiber reinforced concrete [Ezeldin and Balaguru, (1992)]. In the same year, others

investigated perforation of concrete slabs with 48 MPa and 140 MPa unconfined compressive strength [Hanchak et al., (1992)]. In 1993, a team worked on non-linear analysis of RC beams using a SIFCON matrix [Naaman et al., (1993)]. Forrestal and his co-workers conducted research on the development of an empirical equation for penetration depth of ogive-nose projectiles into concrete targets in 1994 [Forrestal et al., (1994)].Two years later, the ACI 544 document " A State of the Art Report on Fiber Reinforced Concrete" was published [ACI 544(1996)]. Yankelevsky, [Yankelevsky, (1997)] studied the local response of concrete slabs to low velocity missile impact and Dancygier published a paper about the effect of the reinforcement ratio on the reinforced concrete resistance to hard projectile impact in 1997 [Dancygier, (1997)]. Work of Dancygier also continued in 1998 by investigating the rear face damage of normal and high-strength concrete elements caused by hard projectile impact Dancygier, (1998)]. In the same year, tests and analysis of the localized response of SIFCON and conventional reinforced concrete (CRC) subjected to blast and fragment loading were done, [Marchand et al., (1998)] while in 1999, Barros and Figueiras studied the flexural behavior of SFRC by the methods of testing and modeling

Studies concerning ballistic performance also progressed during the 1990s. Research about the L/D effect for the long-rod penetrator was reported [Anderson and Walker, (1996)]. Others worked on the ballistic impact effects of austempered ductile iron in [Chinella et al., (1998)] and studies concerning the influence of projectile hardness on ballistic performance were reported in 1999 [Anderson et al., (1999)].

Research to determine the concrete response to extreme loading has also continued after 2000. Predicting penetration, cone cracking, scabbing and perforation of reinforced concrete targets struck by flat-faced projectiles study was conducted [Reid and Wen, (2001)]. In 2003, work on the dimensionless formulae for penetration depth of concrete target impacted by a non-deformable projectile was carried out [Li and Chen, (2003)], and a prediction of perforation thickness and ballistic limit of concrete target subjected to rigid projectile impact was developed [Li and Tong, (2003)]. In 2004, the book "Introduction to

Hydrocodes" was published [Zukas, (2004)]. Several empirical formulas were collected under the study of "Local Impact Effects of Hard Missiles on Concrete Targets" [Li et al., (2005)]. In the same year, a doctoral thesis under the title "Fiber-Reinforced Concrete for Industrial Construction- a Fracture Mechanics Approach to Material Testing and Structural Analysis" [Löfgren, (2005)] was submitted to the Chalmers University of Technology. The bilinear approach for the calculation of SFRC fracture energy was used in this work [Nystöm, (2008)]. A paper under the name of' Reinforced Concrete Perforation and Penetration Simulation Using AUTODYN-3D" [Tham, (2005)] is of great importance since the 48 MPa Drucker-Prager strength data which is used throughout the computations were found by the help of this document. In the same year Chahn also published a paper named "Steel Fiber Reinforced Concrete" which was quite useful in order to determine the increase in tensile strength of SFRC compared to the plain concrete according to use of fibers with different aspect ratios [Chahn, (2005)]. In 2006, by Li, Reid and Ahmad-Zaidi, critical impact energies for scabbing and perforation of concrete target were examined [Li et al., (2006)].

The work done under the licentiate thesis named Concrete Structures Subjected to Blast and Fragment Impacts submitted by Nyström in 2008 [Nyström, (2008)] to the Chalmers University of Technology was relevant for this thesis study, since the method used there in reference to Löfgren, (2005) for the calculation of SFRC fracture energy, forms the basis of the SIFCON and SFRC materials fracture energy calculations in our thesis. In 2009, the response of SIFCON two-way slabs under impact loading was studied and comparisons of different materials including SIFCON in terms of strength and energy absorption capacities are searched [Rao et al., (2009)].

1.3 Object

A major aim of this study was making the simulations of field experiments where a high speed kinetic energy projectile was fired on high strength concrete, SFRC and SIFCON slab specimens. In parallel, another aim was the development

and fine tuning of a suitable computer tool which would adequately provide a model for the experimental data available.

Other aims of this work included making a comparison between crater radius-depths for deformed specimens and the computational model results, obtaining residual velocities of the projectiles from the simulations in order to compare them with the experimental values and gathering these comparisons to determine if such simulation models reflect the experimental behavior and could be used both in practice and for further studies.

1.4   Scope

Within the scope of this thesis, a computational investigation of the effects of the impact of a high speed projectile on high strength concrete, SFRC, and SIFCON specimens was completed. Both modeling and 2D perforation simulations were accomplished. Simulations could not be done in 3D since it requires enormous computation time and the given limited computer resources were not available. ANSYS AUTODYN 11.0 was chosen to be the appropriate software for these modeling and simulation studies.

The computational work of this study consists of impact simulations on three different groups of materials which are struck by a high speed projectile with an average velocity of 1460 m/s. The first target group consists of three concrete specimens stacked one after the other. The second target group contains two SFRC specimens placed in the same fashion as in the first group, and finally, the third group of targets consists of two SIFCON specimens layered sequentially as in the first and second groups. In each group of simulation, the projectile deformed and was eroded as a result of striking the first wall. It is used for the input for the next one. The reason behind using a deformed projectile was to represent the actual test conditions as closely as possible.

Because of the limitations of the software, the goal of perfection and accuracy could not be satisfied at every point in the simulation. Rectangular axisymmetry was replaced by cylindrical axisymmetry in the simulations. There

are reinforcing bars both in reinforced concrete and SFRC specimens in the experiments, but the use of 2D axisymmetry for the computation forced the bars not to be modeled explicitly. Effects of strain rate on the material characteristics were not taken into account since the material strength model (Drucker-Prager) used for target specimens did not allow this facility.

Another limitation was use of the material data found through the literature survey and not being able to work with specific ones belonging to the actual specimens since related material tests from which data would have been collected did not exist.

Simulation results of crater diameter-depth of deformed target and residual velocities of the deformed projectile were compared with the outcomes of the experiments that were supported by TÜBİTAK under Project No: 106M497.

1.5 Outline

The following narrative covers the topics listed below:

In Chapter 1, an introduction for the thesis has been given, and previous studies consulted in the thesis described. The object and the scope of the thesis are stated.

In Chapter 2, the reader is given relevant information about how ballistic performance is affected by changes in parameters of projectile, striking condition and target characteristics.

In Chapter 3, the experimental work impact of projectiles on concrete plates and the main characteristics of the materials used in these experiments plain and reinforced concrete, FRC and SIFCON are explained.

In Chapter 4, details of the modeling and computational simulation which is the core of this thesis are presented.

In Chapter 5, results gained from both computational simulations and experimental studies are introduced, and compared.

In Chapter 6, a summary of the thesis work, conclusions and recommendations for further studies are given.

CHAPTER 2

IMPACT OF FIRED MISSILES ON CONCRETE TARGETS: A REVIEW

2.1   Introduction

The purpose of this chapter is to provide a general introduction to the effects of fired missiles on concrete targets, the most commonly encountered form of protective structure in many applications. The account is descriptive and has been assembled from many acknowledged sources that are in the public domain.

2.2   General Concepts of Impact Loading

While strain rates for creep tests are in the range of 10^{-9} 1/s, static tension tests are 10^{-4}-10^{-2} 1/s and dynamic strain tests are in 10^{-1}-10^{1} 1/s in impact loading, strain rates varies from 10^{2} to 10^{3} 1/s for bullet deformation, 10^{4} 1/s to 10^{5} 1/s for shaped charge and 10^{6} 1/s to 10^{9} 1/s for meteorites (Yıldırım, private communication). Impact of bodies is accompanied by penetration of one member into another and the strain domains of this loading range from static loading to fluid material behavior, impinging on methods of hydrodynamics [Goldsmith, (1960)].

The striking of a high velocity projectile to the target produces impact loading and the kinetic energy computed on such an occasion is huge. This energy is dissipated producing strain and heat and also in deforming the target material. The energy is expended through a local action and a small amount of it is

transmitted to the structure but the magnitude and distribution depends on characteristics of that specific system [TM5-855-1, (1984)].

Possible deformations in the target part of intermediate velocity impact phenomena will be mentioned in the following section. In order to obtain accurate results from impact models, an adequate theoretical treatment and knowledge about the dynamic behavior of a specifically treated body must be gained through suitable experiments [Goldsmith (1960)].

2.3   Penetration-Perforation-Failure Modes

When there is an impact loading, deformation both in the target and penetrator occurs. Target parts of these effects are:

Penetration: Tunneling into target up to some depth which is called penetration depth. [Lia et al., (2005)]. However, in connection with what we call complete penetration and partial penetration, there are some different approaches shown in Figure 2.1 from Zukas et al., (1982) given below with explanations.
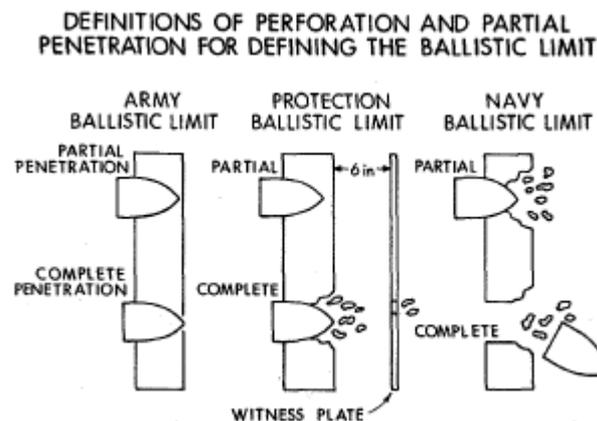
Figure 2.1: Different approaches for complete penetration [Zukas et al., (1982)]

1- Target must be deformed in the way that light could pass through it.

2- Plate which is placed behind the target would perforate

3- At least one half of the missile must get through the target.

9

Perforation: This requires complete penetration of the penetrator into the target; there may or may not be some residual velocity. [Lia et al., (2005)]

Spalling: Spalling requires material ejaculation from the rear face of the target as a result of the reflection of the initial compressive wave from the free surface causing tensile one. Information of spalling, scabbing, plugging, fracture (except radial one) and petaling are gained through Zukas et al., (1982). Scabbing and spalling are shown in Figure 2.3.

Scabbing: is similar to spalling in appearance, but here fracture is produced by large deformations and its surface is determined by local inhomogeneity and anisotropy.

Plugging: As a result of impact of a blunt or hemispherical nose projectiles (plugging is very sensitive to the nose shape and angle of strike), velocities which are close to ballistic limit, cause plugging. This separation may occur in a mode of fracture: formation of voids and growth in shear or by adiabatic shearing. Plugging, fracture, and petaling are shown in Figure 2.2.

Fracture: Initial stress wave which is above the ultimate strength of the material. Fracture can occur in a low density target.

- Brittle Fracture: When ductility of the material is very low, fracture occurs in this manner.
- Radial Fracture: When cracks develop through the target thickness, then from the impact point radial cracks may appear on either the front or rear face of the concrete slab or both. [Lia et al., (2005)]

Petaling: After the ogival or conical low impact velocity bullet or blunt projectile with a ballistic limit hits a thin plate, large plastic flow with permanent flexure occurs, after tensile strength of the material is reached, and the view seen in Figure 2.2 is obtained.
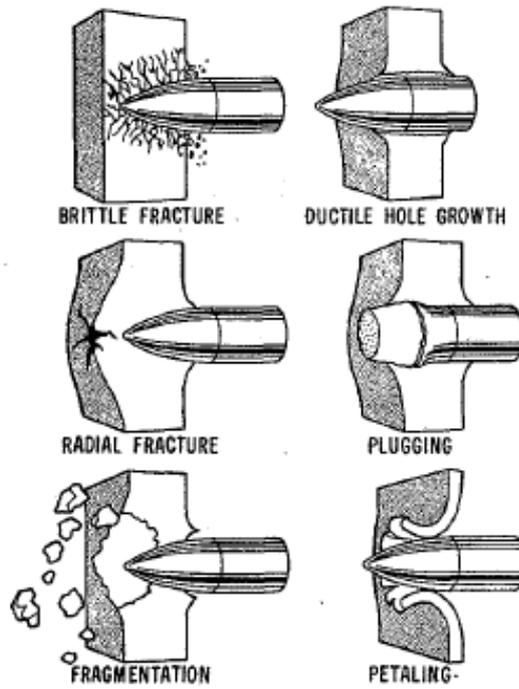
Figure 2.2: Images of possible failure models [Zukas et al., (1982)]

a-Spall   b-Scabbing
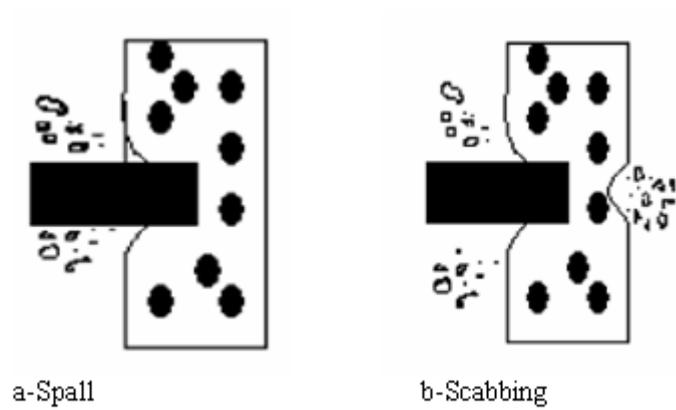
Figure 2.3: Possible spalling and scabbing views [Lia et al., (2005)]

11

2.4   Parameters Which Effect Penetration and Perforation

When there is an impact loading, then whether there is going to be a penetration-perforation or what type of failure would take place depends on the target and projectile characteristics along with striking conditions. Parameters that are in the range of these characteristic and conditions are given by TM5-855-1, (1984) and Zukas et al., (1982).

Penetration and perforation depend on following:

- Projectile Characteristics
    - Basic Shape-Diameter (L/D Ratio): Projectile can be in the basic shape of solid rod, sphere, hollow shell or irregular solid and diameter of it may vary.
    - Nose Configuration: The nose of the projectile can be a cone, ogive, hemisphere, or it can be blunt
    - Hardness
    - Density: Projectile can be made of lightweight (wood, plastic, ceramic, and aluminum), intermediate (steel, copper) or heavy (lead, tungsten) material.
- Striking Conditions
    - Impact Velocity: Ranges of velocity which creates impact can be divided as low velocity (<250 m/s), intermediate-high velocity (0.5-2 km/s and 2-3 km/s), hypervelocity (3-12 km/s) and ultra high velocities (>12 km/s).
    - Angle of Incidence
    - Yaw: The flight path perturbation
- Target Characteristics
    - Strength
    - Density
    - Ductility
    - Reinforcement
    - Thickness: Target can be thin, intermediate, thick or semi-infinite.

12

Ballistic Limit: Definition of ballistic limit must be given when penetration-perforation is being considered. Ballistic limit is the minimum velocity that projectile can perforate through the target and it is affected by many parameters. Techniques to reach ballistic limit can be either deterministic or probabilistic. For the former one, conservations laws and material constituents must be used, during calculations, in order to simplify complex partial differential equations, and empirical determinations need to be made for one or two constants. For the latter, over a large amount of data of striking-residual velocity and either penetration or perforation occurs is taken as basis and arranged in a statistical-probabilistic environment. Velocity for 50 percent of possibility for perforation occurrence is named as V_{50} or, in other words, the ballistic limit. [Zukas et al., (1982)]

2.4.1 Projectile Characteristics

2.4.1.1 L/D Ratio of the Projectile

Daneshjou et al. (2005) implied that, as L/D ratio increases penetration depth increases, normalized penetration depth which is the ratio of penetration depth to penetrator length, decreases. Adding to this, the effect of L/D over the hydrodynamic velocity (the velocity that the object's resistance is no longer important and the materials have fluid behavior) is quite negligible. Anderson and Walker (1996) mention that, around ordinance velocities of 1.0 – 1.9 km/s, the projectile loses efficiency significantly in terms of P/L, as L/D increases. But for higher velocities like 2-4.5 km/s, the mechanism of the L/D effect changes. Efficiency of the penetration versus impact velocity for different L/D ratios is shown in Figure 2.4.
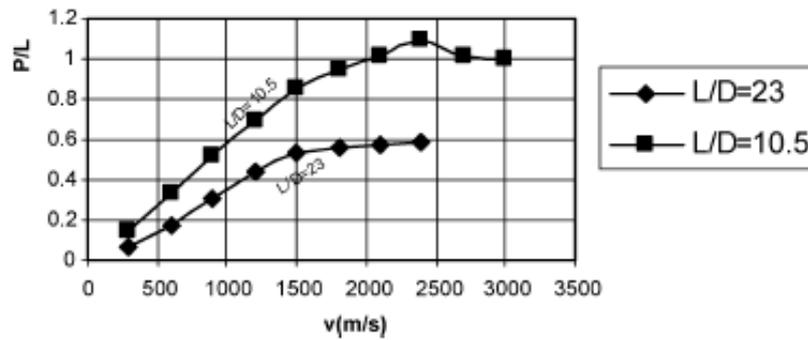
Figure 2.4: Efficiency of the penetration versus impact velocity for different L/D ratios [Daneshjou et al. (2005)]

Zukas et al., (1982), mention work by Lambert and Jonas, (1976) and Lambert, (1978) where several measurements were obtained in terms of impact of hemispherical nosed steel rods to RHA (Rolled Homogeneous Amour) plates with different thickness and obliquities. Results for ballistic limit- normalized target thickness for different L/D ratios are shown in Figure 2.5. The parameter e/D stands for

$$\frac{e}{D} = \frac{T}{D} * \left(\frac{1 + 2 * \sec\theta}{3} \right) \tag{2.1}$$

Where θ is obliquity, T is thickness and D is diameter.
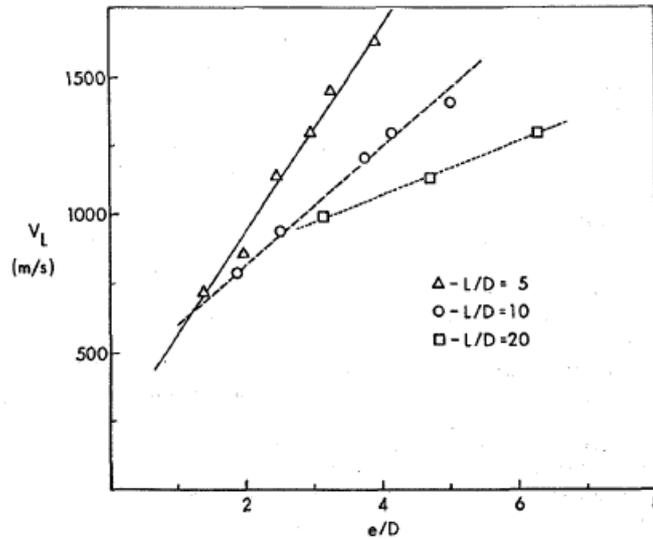
Figure 2.5: Ballistic limit versus normalized target thickness for different L/D
ratios [Zukas et al., (1982)]

2.4.1.2 Nose Configuration of the Projectile

In the Phillabaum II et al. (2008) project report, several experiments
concerning efficiency of nose configuration under impact loading were conducted.
Projectiles used were hemispherical (caliber head radius (CHR)= 0.5) and ogive
nosed (CHR=2). Both types of projectiles were made of same material (Viscomax
300 maraging steel) and the target was thin slab of double reinforced concrete
(DRC). The obliquity was 0 degrees.

There were 6 shots with hemispherical nosed projectiles which had
velocities between 230-730 m/s. In two of the highest velocity experiments, the
projectiles deformed severely, while the 400 m/s velocity projectile experienced
only little plastic deformation. Cases involving velocities below 300 m/s did not
deform at all. Outcomes of the experiments can be seen in Table 2.1 deformed
images of the projectiles are shown below Figure 2.6, Figure 2.7 and Figure 2.8.

15

Table 2.1: Outcomes of the experiments for hemispherical nosed projectiles
[Phillabaum II et al.,(2008)]

Projectile	Striking Velocity (m/s)	Total Yaw (degrees)	Residual Velocity (m/s)	Remarks
CRH 0.5	300	No Data	231*	
CRH 0.5	721	0.3	535*	Projectile failed
CRH 0.5	529	1.9	423*	Projectile failed
CRH 0.5	232	8.3	133*	
CRH 0.5	304	0.9	235	
CRH 0.5	400	0.7	313	Slight deformation
			* Debris Velocity	

Figure 2.6: CRH=0.5 projectile pieces from the 529 m/s experiment. [Phillabaum II et al.,(2008)]

Figure 2.7: CRH=0.5 projectile pieces from the 721 m/s experiment. [Phillabaum II et al.,(2008)]
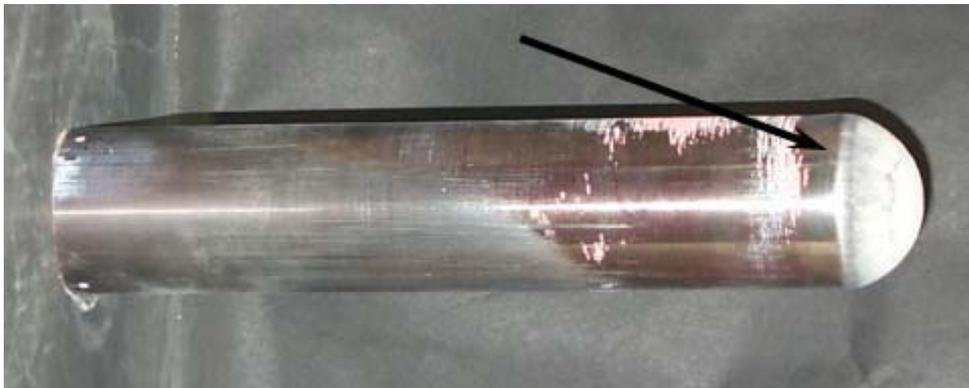
Figure 2.8: CRH=0.5 projectile pieces from the 400 m/s experiment. [Phillabaum II et al.,(2008)]

In the ogive nosed projectiles used experiments, striking velocities were 707 and 784 m/s. Results of those experiments and high speed camera views of exiting projectiles can be viewed inTable 2.2 , Figure 2.9 and Figure 2.10.

Table 2.2: Outcomes of the experiments for ogive nosed projectiles [Phillabaum II et al.,(2008)]

Projectile	Striking Velocity (m/s)	Total Yaw (degrees)	Residual Velocity (m/s)	Remarks
CRH 2	707	0.8	634	Intact
CRH 2	784	3.1	719	Intact
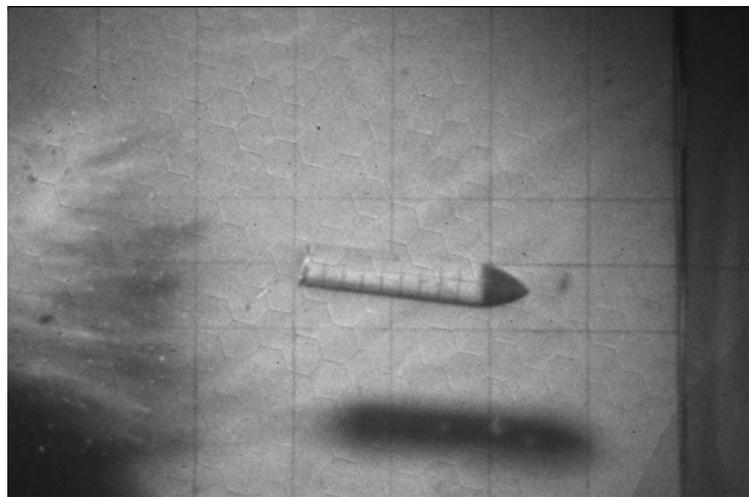
Figure 2.9 : High-speed camera image of the CRH=2 projectile after exiting the DRC target in the 707-m/s experiment [[Phillabaum II et al.,(2008)]
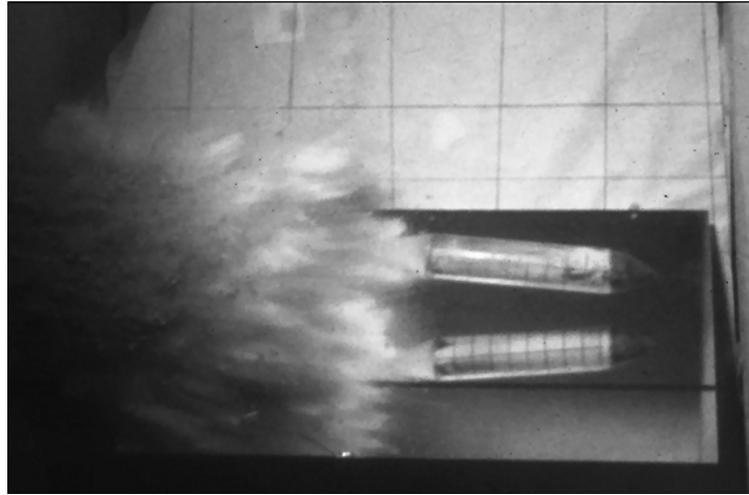
Figure 2.10: High-speed camera image of the CRH=2 projectile after exiting the
DRC target in the 784-m/s experiment [[Phillabaum II et al.,(2008)]

After experiments and analysis of the project it was concluded that, in
normal (0° obliquity) impacts at higher impact velocities, the CRH=2
configuration has a greater residual velocity being a more efficient penetrator than
the blunt-nose CRH=0.5 configuration. From these results, one might also
conclude that the change in nose shape from CRH=0.5 to CRH=2 significantly
improves integrity of the projectile for normal impact for these targets at high
velocity. [Phillabaum II et al.,(2008)]

In Zukas et al., (1982), studies about nose-shape are also conducted and
the nose shape of the projectile is said to be very important for ballistic limit
under dynamic yield strength of the rod, although, it does not have a significant
effect for velocities over the dynamic yield strength. Tests were made to see this
nose shape effect in ballistic limit. Fixed weight steel rods of 14.6 g with L/D=10
and BHN 555 were tested for 0 degree and 60 degree obliquity. Their nose shapes
were blunt, 40 degree conical, hemisphere and 2.1-caliber tangent ogive. Though
ballistic limits for ogival, conical and hemispherical are close to each other within
4 percent, blunt nose projectile was the one which needed the most energy. Its
ballistic limit is about 6.5 percent higher than the lowest one which came to be

hemispherical in those experiments. Outcomes for that experiment are shown in Table 2.3 below:

Table 2.3: Results of the experiments concerning ballistic limit velocity and nose-shape [Zukas et al., (1982)]

Nose Shape (Rod Diameter=6.35 mm)	Ballistic-Limit Velocity, m/s 12.7 mm RH Armor, BHN 380	
	0°	60°
Hemisphere	875	1213
Conical	892	1262
Blunt Nose	942	1273
2.1-Caliber Tangent Ogive	—	1225

2.4.1.3   Material Hardness of the Projectile

In the Anderson Jr. et al., (1999) paper, Grabarek C.L., (1971), was said to have studied the effect of penetrator hardness on ballistic performance and concluded that stronger materials would penetrate better than softer ones. Further research was carried out about hardness of the penetrator and ballistic performance, in Anderson et al., (1999) paper again, experiments done with 17 different types of materials including 5 different type of steel with different hardness and one tungsten projectiles having L/D ratio of 10 subjected to finite-thick armor steel targets were mentioned. It was found that both residual length of the target and ballistic limit are affected by the material hardness. When hardness of the projectile is greater than hardness of the target, ballistic limit velocity decreases significantly, adding to this residual length of the projectile increases as the hardness of the material increases. Another finding of this article was that although numerical simulation predicted otherwise, experimental work showed that, as strength of the projectile increases, residual velocity either stayed constant or increased a bit. Normalized residual length-impact velocity for different hardness is shown in Figure 2.11.
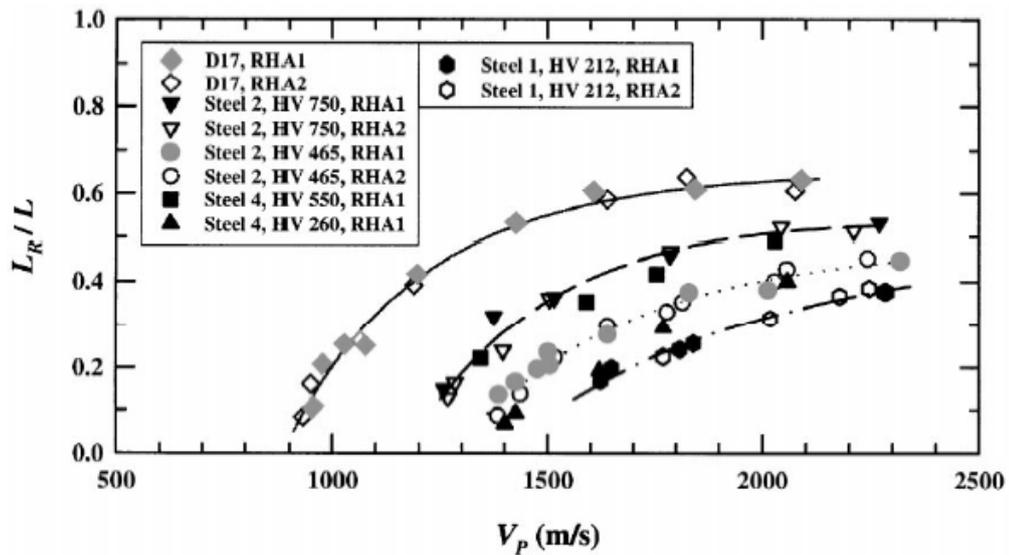
Figure 2.11: Normalized residual length versus impact velocity [Anderson Jr. et al., (1999)]

In Zukas et al., (1982), it was mentioned that, soft rod (Brinnel Hardness Number (BHN)-200) experiences a large plastic deformation after impact takes place and loses 7 percent of its mass while an intermediate hardness rod (BHN-285) has a less plastic damage but more of mass loss (28 percent) in the experiments. For the case where rod has the biggest hardness (BHN-600), plastic damage is smaller than the intermediate hardness rod but it breaks during penetration. When largest of two pieces were brought together, it was found that, only 66 percent remained, in other words, there was 34 percent mass loss. Another experiment from the same reference showed that with minimum velocity of 625m/s of penetrators with different hardness struck at thick targets (AISI 6150 steel alloy, BHN 190, 7.6cm thick) and after small penetration, BHN 220 and 375 rods were deformed significantly while BHN 600 rod penetrated 13 times greater than the softest one and did not deform at all.

Figures of striking velocity-residual velocity for different hardness, rod hardness-ballistic limit and striking velocity-residual rod weight are given below in Figure 2.12, Figure 2.13, Figure 2.14. During experiments, AISI 1066 rods with hardness of BHN 255-285, BHN 375-430, BHN 555-600 with 5.6 mm diameter

21

and L/D 10 ratio were used, striking velocities ranged through 635-1375 m/s. As can be seen in Figure 2.12 over 1200 m/s, the rod hardness does not have a significant effect on velocity.
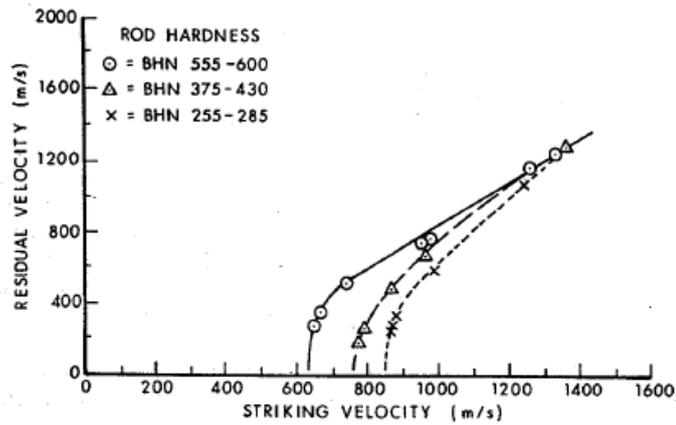
Figure 2.12: Outcomes of the experiments for residual velocity versus striking velocity for different rod hardness [Zukas et al., (1982)]
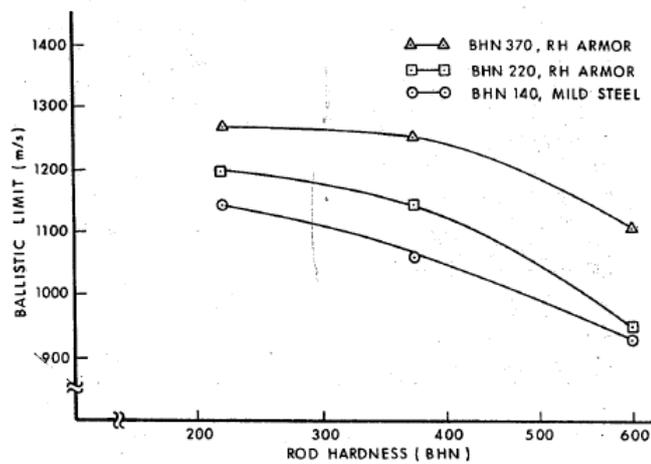
Figure 2.13: Outcomes of the experiments for ballistic limit versus rod hardness [Zukas et al., (1982)]

22
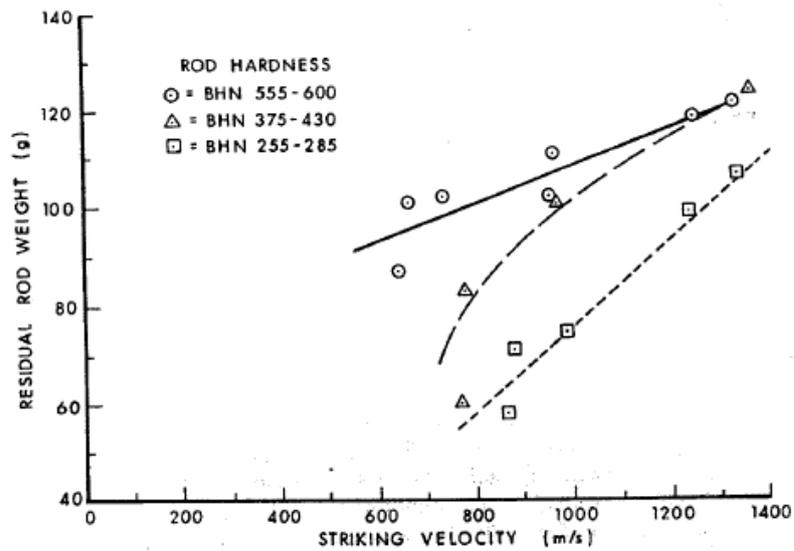
Figure 2.14: Outcomes of the experiments for residual rod weight versus striking velocity [Zukas et al., (1982)]

2.4.1.4   Material Density of the Projectile

In Anderson and Schultz, (2005), 90 degree strikes of projectiles with different densities were tested. The target was sand and its bulk density was 1.62 gr/cc. Characteristics of the projectiles are shown in Table 2.4 below.

Table 2.4: Characteristics of the projectile [Anderson and Schultz, (2005)]

	Projectile		Impact
Type	Diameter	Density	Velocity
Aluminum	3.13 mm	2.80 g/cc	5.5 km/s
Aluminum	6.35 mm	2.80 g/cc	1.0 km/s
Copper	3.13 mm	8.97 g/cc	1.0 km/s
Pyrex	6.35 mm	2.17 g/cc	1.0 km/s

The same paper showing the reference [Schultz P.H., (2003)] mentions that, higher density projectiles would penetrate deeper into the target material and transport their momentum farther in the target. In the experiments of the same paper, results have shown that the effect of projectile momentum is more obvious in low velocity (here what is called low velocity is 1000 m/s) and deep penetration impact and the reason ~~is~~ given is the time increasing of projectile transferring momentum to the target. Results have also indicated that: ejection angle can be used as a measure for projectile target density ratio or penetration depth: higher angle showing deeper penetration. Ejection angles as a function of ejection position scaled by the average final crater radius for the same four projectiles are shown in Figure 2.15 below.
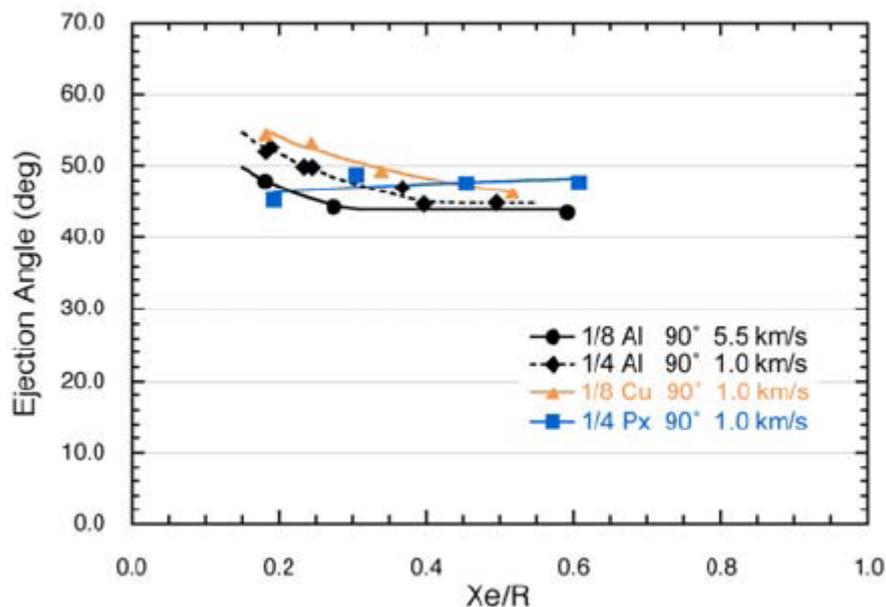
Figure 2.15: Result of experiments in terms of ejection angles versus ejection position scaled by the average final crater radius [Anderson and Schultz, (2005)]

In Zukas et al., (1982), experiments conducted with projectiles of constant L/D ratio (10), constant mass (65 g) but different nose made materials (tungsten carbide, tungsten alloy, depleted uranium and steel) and the same, deep steel target plates, have shown that, in the manner of ballistic limit velocities to thick

target plates, denser projectiles have shown better performance than comparatively low density projectiles. However in thinner targets, low density projectiles have shown better results. Figure 2.16 shows the result of experiments in terms of ballistic velocity versus target thickness:
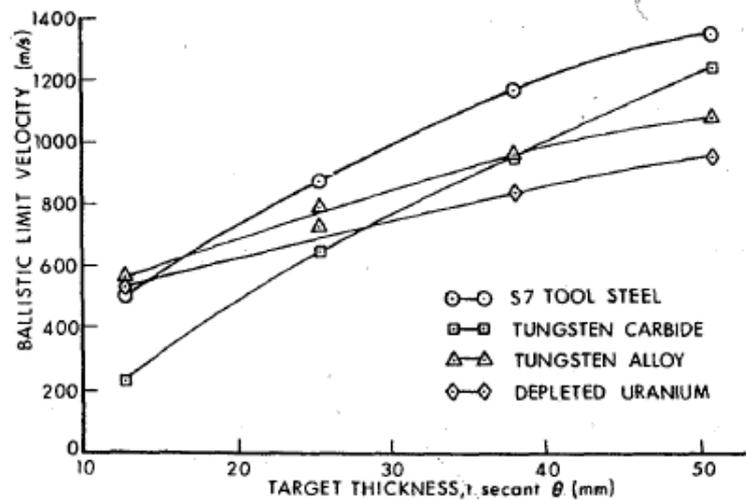
Figure 2.16: Experiment results for ballistic limit versus target thickness for different densities [Zukas et al., (1982)]

Furthermore in the same reference, Grabarek, C., (1973) was reported to have conducted an experiment in which same weight and L/D projectiles with different densities versus ballistic limit were mentioned. The result of the experiment is shown in Figure 2.17 below:
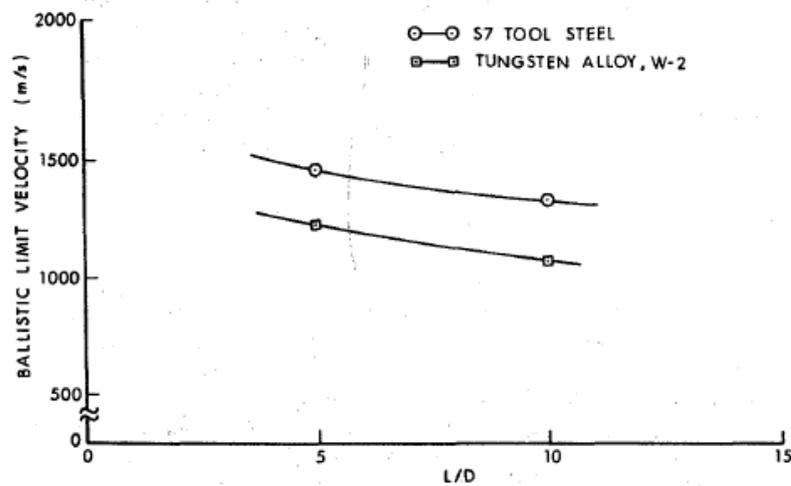
Figure 2.17: Experimental outcomes for same weight, different density projectiles
in terms of ballistic limit versus L/D [Zukas et al., (1982)]

2.4.2 Striking Conditions

2.4.2.1 Impact Velocity

Impact loading has different velocity regimes and the response of the structure changes among these regimes. In fact, if the problem falls in low-velocity regime (<250m/s) local indentation or penetrations are strongly related to the overall deformation of the structure, when it is in the intermediate velocity regime, (0.5-2km/s), instead of response of the whole system, behavior of the material within the impact area 2-3 diameter of the projectile becomes dominant. Effects of velocity, geometry, material characteristics, and localized plastic flow, failure and strain rates are quite of importance and total incident time is defined in microseconds. Impact velocity of 2-3 km/s(upper limit of this range is the lower limit of the hypervelocity impact of 3-12 km/s) makes localized pressures above the strength of the material by an order of magnitude and colliding solids act like fluid in early stages of impact. For ultra-high velocity impact (>12km/s), explosive vaporization of the materials takes place because of very high strain

26

rates. [Zukas et al., (1982)]. Figure 2.18 explains the effect of impact with the method of loading and strain rate.
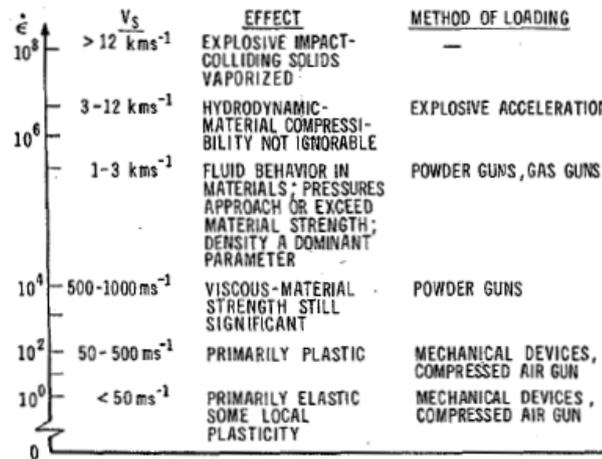
Figure 2.18: Effect of impact with method of loading and strain rate [Zukas et al., (1982)]

If material is shocked to very high pressures, it behaves like a fluid, but otherwise strength parameters control response of the material. Examples for responses can be given as follows: projectile making a deep tunnel in low strength targets, projectile ricochet on target surface which either remains undeformed or subjected to strength related failures of cracking and scabbing [Zukas et al., (1982)].

In a paper of Li et al., (2006) from which information has been taken to compose this section, concrete scabbing and perforation related with impact energy was studied. In this paper, it was mentioned that, when a flat nose projectile strikes a concrete target, for less than the perforation time, scabbing occurs because of the tensile wave which is the reflection of the compressive one. Minimum target thickness to prevent scabbing is named as the scabbing limit (hs).

$$h\text{s} = G\left(M,\ V0,\ d,\ \rho,\ f\text{c},\ f\text{t}, E,\ a,\ r\right) \tag{2.2}$$

where ρ, E and f_c and f_t are the density, Young's modulus and unconfined compressive and tensile strengths of the concrete target, a is the characteristic size of aggregate and r is the average percentage amount of reinforcement each-way-each-face (ewef). M is mass, $V0$ is the initial impact velocity of a projectile and d is the (cylindrical) projectile shank diameter. Generally amount of aggregate and reinforcement are neglected since light or moderate reinforcement do not have much effect on penetration and scabbing. Formulation may be set for scabbing limit thickness but since for a given target, the minimum energy and velocity which causes scabbing is also very important, equation can be converted as:

$$\frac{E_c}{d^3 * f_c} = G * \left(M\frac{\rho}{d^3}, \frac{H}{d}, \frac{f_t}{f_c}, \frac{\tau_f}{f_c} \frac{E}{f_c} \right) \tag{2.3}$$

$$E_c = \frac{1}{2} * M * V_c^2 \tag{2.4}$$

When perforation is our main concern, shear strength must be added to the scabbing parameters.

$$\frac{E_c}{d^3 * f_c} = G * \left(M\frac{\rho}{d^3}, \frac{H}{d}, \frac{f_t}{f_c}, \frac{\tau_f}{f_c} \frac{E}{f_c} \right) \tag{2.5}$$

Again in the same paper, empirical and semi-empirical formulas were studied to see their correlation with the experimental values where UMIST (The University of Manchester Institute of Science and Technology) formulae of scabbing and perforation are among the concerned formulas. Further explanations are as given below:

When critical impact energies for local impact damage of concrete investigated in Reid and Wen, (2001), a collection of formulae are derived from Central Electricity Generating Board (CEGB) data were used and implemented in R3 Impact Assessment Procedure for nuclear facilities in BNFL, (2003). Due to the complexity and uncertainty of the local failure mechanisms, the methodology

employed in Reid and Wen, (2001) is based on the formulation of empirical equations correlated with test results.

In these formulations, parameter ranges are considered as $22 < d < 600$ (mm), $1 < M < 2622$ (kg), $0 < V0 < 427$ (m/s), $19.9 < f_c < 78.5$, $0 < r < 4$ (percentEWEF) and $50.8 < H < 640$ (mm) for thin targets $\frac{H}{d} \leq 5$ and $\frac{H}{d} > 5$ separately. In the following equations, target is assumed to be non-reinforced. E_{cs} is critical impact energy for scabbing and E_{cp} is critical impact energy for perforation, σ_t is the crushing stress. The formulation for scabbing turns out to be:

$$0.34 \leq \frac{H}{d} \leq 1 \quad \text{for } 0.4 \leq \left(\frac{H}{d}\right) \leq 5 \tag{2.6}$$

$$\frac{E_{cs}}{d^3 * f_c} = \frac{\pi}{4} * \left(\frac{\sigma_t}{f_c}\right) * \left[\frac{H}{d} - 4.3\right] \text{ for } \left(\frac{H}{d}\right) > 5 \tag{2.7}$$

$$\sigma(Pa) = 4.2 * f_c(Pa) + 135 * 10^6 + [0.014 * f_c(Pa) + 0.45 * 10^6] * V_c(m/s) \tag{2.8}$$

While the formulation for perforation is:

$$\frac{E_{cs}}{d^3 * f_c} = \frac{1}{2} * \frac{\sigma_t}{f_c} * \left(-0.00506 * \left(\frac{H}{d}\right) + 0.01506 * \left(\frac{H}{d}\right)^2\right) \text{ for } 0.34 \leq \frac{H}{d} \leq 1 \tag{2.9}$$

$$\frac{E_{cs}}{d^3 * f_c} = \frac{1}{2} * \frac{\sigma_t}{f_c} * \left(-0.01 * \left(\frac{H}{d}\right) + 0.02 * \left(\frac{H}{d}\right)^3\right) \quad \text{for } 0.1 < \frac{H}{d} \leq 5 \tag{2.10}$$

$$\frac{E_{cs}}{d^3 * f_c} = \frac{\pi}{4} * \left(\frac{\sigma_t}{f_c}\right) * \left[\frac{H}{d} - 3\right] \quad \text{for } 5 < \frac{H}{d} \tag{2.11}$$

The relationships between $\frac{E_{cs}}{d^3 * f_c}$ and $\frac{H}{d}$ for scabbing and perforation are derived using the NDRC, (1946) expression. Empirical formulae of penetration, scabbing and perforation, are further developed into semi-empirical

29

formulae when the NDRC penetration formula is replaced by the Li and Chen, (2003) penetration formula.

NDRC empirical formulae of scabbing and perforation after arranged concerning critical impact energy for scabbing becomes:

$$\frac{E_{cs}}{d^3 * f_c} = \left(\frac{V_0}{d}\right)^{0.2} * f_c^{-\frac{1}{2}} * \left[52.84 - \sqrt{2789.4 - 903.9\left(\frac{H}{d}\right)}\right]^2 \tag{2.12}$$

for $\left(\dfrac{H}{d}\right) \leq 3$

$$\frac{E_{cs}}{d^3 * f_c} = \left(\frac{V_0}{d}\right)^{0.2} * f_c^{-\frac{1}{2}} * \left[51.35\left(\frac{H}{d}\right) - 105.34\right]^2 \tag{2.13}$$

for $3 < \left(\dfrac{H}{d}\right) \leq 4.84$

$$\frac{E_{cs}}{d^3 * f_c} = \left(\frac{V_0}{d}\right)^{0.2} * f_c^{-\frac{1}{2}} * \left[1.389 * 10^4 \left(\frac{H}{d}\right) - 4.677 * 10^4\right]^2 \tag{2.14}$$

for $4.84 < \left(\dfrac{H}{d}\right) \leq 18$

NDRC empirical formulae of scabbing and perforation after arranged concerning critical impact energy for perforation become:

$$\frac{E_{cp}}{d^3 * f_c} = \left(\frac{V_0}{d}\right)^{0.2} * f_c^{-\frac{1}{2}} * \left[150.0 - \sqrt{22.53 * 10^3 - 6.36 * 10^3\left(\frac{H}{d}\right)}\right]^2 \tag{2.15}$$

for $\left(\dfrac{H}{d}\right) \leq 3$

$$\frac{E_{cp}}{d^3 * f_c} = \left(\frac{V_0}{d}\right)^{0.2} * f_c^{-\frac{1}{2}} * \left[54.46\left(\frac{H}{d}\right) - 71.96\right]^2 \tag{2.16}$$

for $3 < \left(\dfrac{H}{d}\right) \leq 3.8$

$$\frac{E_{cp}}{d^3 * f_c} = \left(\frac{V_0}{d}\right)^{0.2} * f_c^{-\frac{1}{2}} * \left[1.473*10^4\left(\frac{H}{d}\right) - 3.774*10^4\right]^2 \qquad (2.17)$$

for $3.8 < \left(\dfrac{H}{d}\right) \leq 18$

As mentioned earlier, NDRC empirical formulas of scabbing and perforation are further developed into semi-empirical formulae when the NDRC penetration formula is replaced by the Li and Chen, (2003).

According to these semi-empirical formulae, critical impact energy for the scabbing is given as follows where $S = 72 * \left(f_c (Mpa)\right)^{-0.5}$.

:

$$\frac{E_{cs}}{d^3 * f_c} = 0.196 * S * \left[0.782 - \sqrt{0.611 - 0.198\left(\frac{H}{d}\right)}\right]^2 \quad \text{for } \left(\frac{H}{d}\right) \leq 3 \qquad (2.18)$$

$$\frac{E_{cs}}{d^3 * f_c} = 0.106 * S * \left[\left(\frac{H}{d}\right) - 2.12\right]^2 \quad \text{for } 3 < \left(\frac{H}{d}\right) \leq 4.84 \qquad (2.19)$$

$$\frac{E_{cs}}{d^3 * f_c} = 0.577 * S * \left[\left(\frac{H}{d}\right) - 3.48\right] \quad \text{for } 4.84 < \left(\frac{H}{d}\right) \leq 18 \qquad (2.20)$$

Again according to these semi-empirical formulas, critical impact energy for the perforation becomes:

$$\frac{E_{cp}}{d^3 * f_c} = 0.196 * S * \left[2.222 - \sqrt{4.935 - 1.393\left(\frac{H}{d}\right)}\right]^2 \quad \text{for } \left(\frac{H}{d}\right) \leq 3 \qquad (2.21)$$

$$\frac{E_{cp}}{d^3 * f_c} = 0.128 * S * \left[\left(\frac{H}{d}\right) - 1.32\right]^2 \quad \text{for } 3 < \left(\frac{H}{d}\right) \leq 3.8 \qquad (2.22)$$

$$\frac{E_{cp}}{d^3 * f_c} = 0.633 * S * \left[\left(\frac{H}{d}\right) - 2.56\right] \quad \text{for } 3.8 < \left(\frac{H}{d}\right) \leq 18 \qquad (2.23)$$

In the Li et al., (2006) paper, comparison of these empirical, semi-empirical formulae outcomes with experimental values in Bainbridge, (1988) is given. The results for scabbing are given in Figure 2.19:
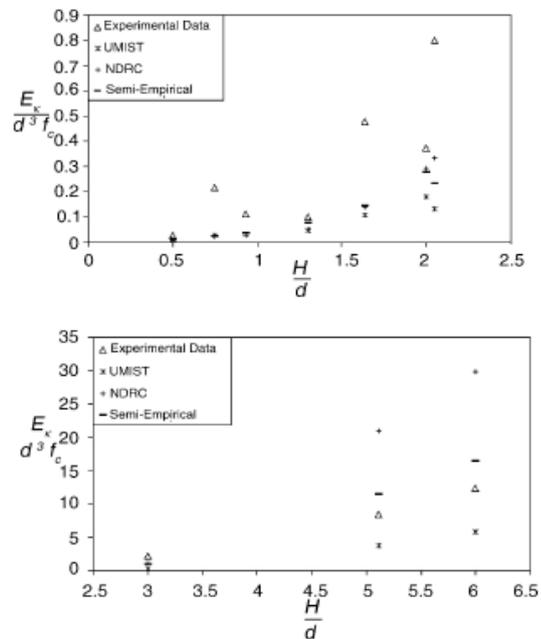
Figure 2.19: Comparison of these empirical, semi-empirical formulae outcomes with experimental values in Bainbridge, (1988)[Li et al., (2006)]

As a result, Li et al., (2006) concluded that, UMIST formula values are the lowest of all equations, so, those formulas do not need a safety factor for the applications while the NDRC and semi-empirical formulae sometimes overestimate the critical impact energy for the impact damage. Since NDRC formulae have wide range of applications and a long history, it is still worth making use of them as references. The semi-empirical formulae for perforation presented in the paper better depict the physics of the damage than fully empirical formulae so they also have good accuracy with experimental results.

2.4.2.2　Angle of Incidence

In the paper of Khan et al., (2003), hardened steel projectiles were impacted to thin aluminum targets of different thicknesses with different striking angles. Velocity limit was up to 150 m/s, and obliquity varied through 0, 15, 30, 45, and 60 degrees. Target thicknesses were 0.81 mm, 1.52 mm, and 1.91 mm thin aluminum with yield strength of 110 MPa. Projectile used in the experiment has 12.8 mm diameter and 25.6 mm length. In the experiments, ballistic limits for different angle of incidence and different target thicknesses were determined firstly. Results can be seen in Table 2.5:

Table 2.5: Experimental outcomes for ballistic limit and obliquity [Khan et al., (2003)]

| Angle of obliquity (deg) | Ballistic limit (m/s) of the plates | | |
| | Plate thickness (mm) | | |
	0.81	1.52	1.91
0	28.8	45.3	51.0
15	24.4	40.3	50.8
30	23.4	39.3	55.7
45	37.3	45.3	57.0
60	48.8	52.9	79.3

Effect of obliquity is shown by plotting impact and residual velocities for different angles of incidence .It was decided that residual velocity decreases with an increasing obliquity and this effect is much more significant in lower impact velocities than higher ones. Results of the experiments are shown in Figure 2.20

33
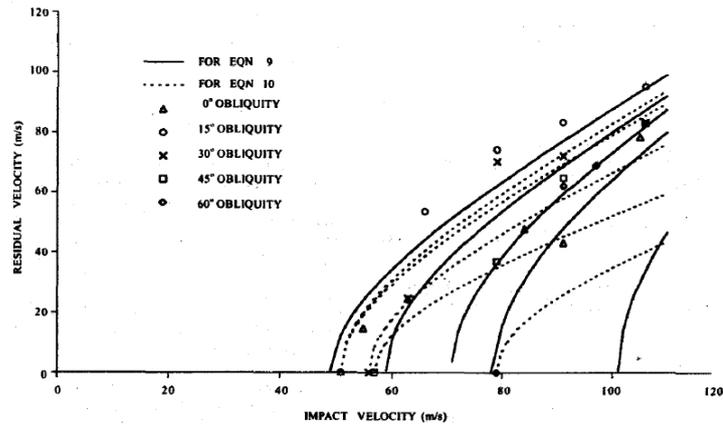
Figure 2.20: Outcomes of the experiments for residual versus impact velocity
point of view   [Khan et al., (2003)]

For a particular thickness, energy absorbed by the target is almost constant
in different impact energy levels but it increases with increasing as striking angle
changes. Absorbed energy versus impact energy for different thicknesses are
shown in Figure 2.21 and Figure 2.22 for two different obliquity values.
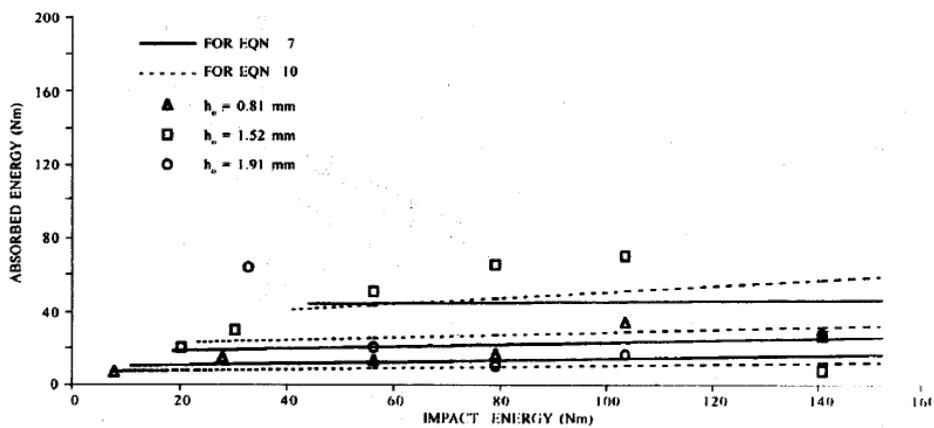
Figure 2.21: In obliquity of 15 degrees, absorbed energy versus impact energy
[Khan et al., (2003)]
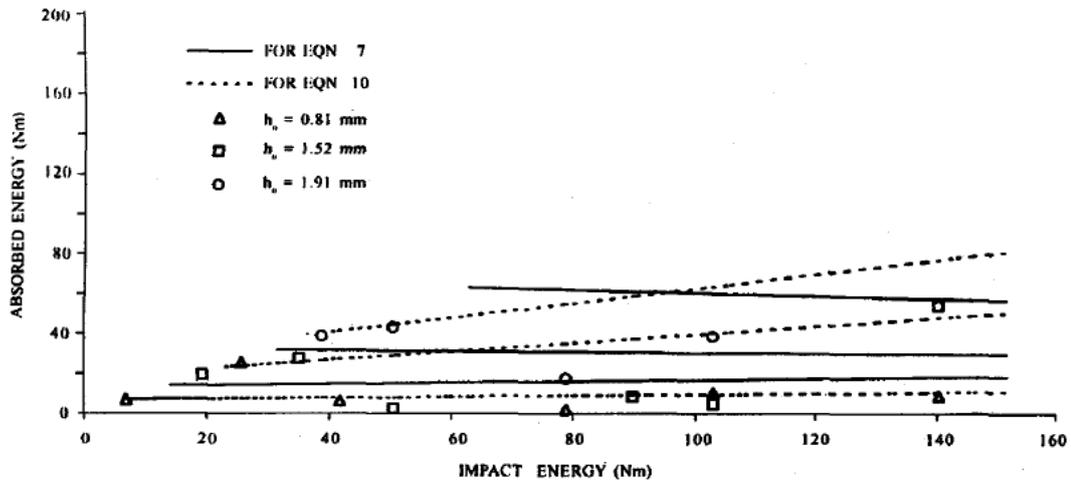
Figure 2.22: In obliquity of 30 degrees, absorbed energy versus impact energy
[Khan et al., (2003)]

Another experimental study of normal and oblique impact is conducted in Madhu et al., (2003). In the study, ogive shaped, hard steel projectiles on single target were used. Armour piercing projectile velocity range was around 820 m/s. Plates which were made of mild steel, RHA steel and aluminum had varied thicknesses of 10 mm to 40 mm. Plate thicknesses to diameter length ranges from 1.5 to 6.5. Properties of the materials are shown below in Table 2.6:

Table 2.6: Characteristics of the materials used in the experiment [Madhu et al., (2003)]

Material	Thickness (mm)	Hardness (VPN)	Yield stress (MPa)
Mild steel	10, 12, 16, 20, 25	140-145	327
RHA steel	8, 12, 16, 20	280-300	940
Aluminium	10, 20, 30, 40	30-35	135

In this study, the striking angle was increased incrementally from 0 to 60 degrees or until ricocheting occurred. Results of the experiments concerning different thicknesses and different obliquities for two different materials are shown in Figure 2.23 and Figure 2.24.
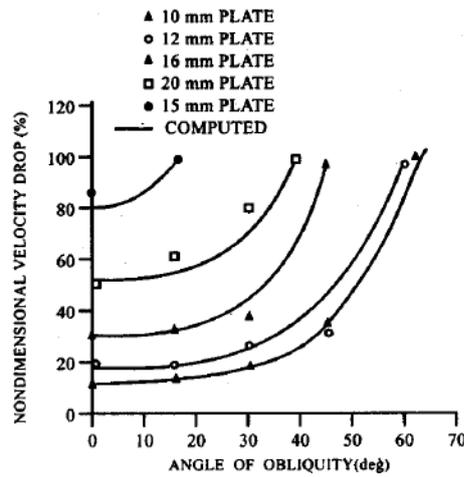
Figure 2.23: Angle of obliquity versus non-dimensional velocity drop for mild steel target [Madhu et al., (2003)]
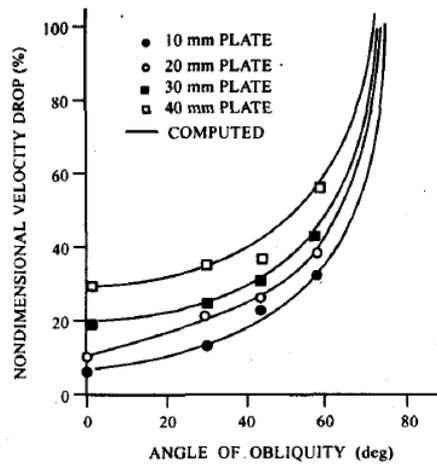
Figure 2.24: Angle of obliquity versus non-dimensional velocity drop for aluminum target [Madhu et al., (2003)]

Here also it can be seen that, as obliquity increases, the non dimensional velocity drop increases for plates of the same thicknesses.

2.4.2.3   Yaw

Zukas et al., (1982), defines yaw as perturbation of the flight path and it is shown as in Figure 2.25.
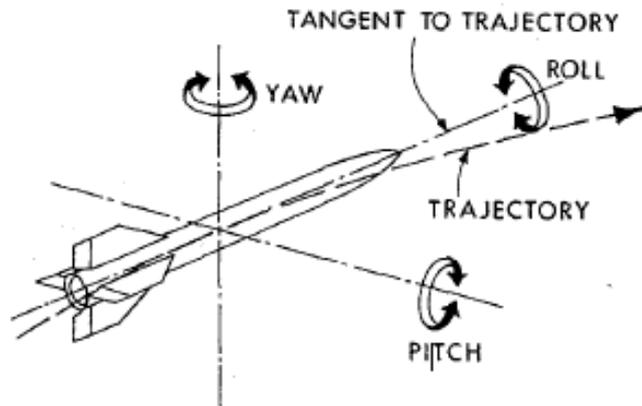
Figure 2.25 Description of yaw [Zukas et al., (1982)]

In the same reference it has been mentioned that when the projectile yaw increases, thick target penetration degraded and projectile deformation or break-up can be seen. Grabarek (1973) worked on the effect of yaw for long rod on ballistic limit concerning residual velocity and different yaw angles. In Figure 2.26 below, the result of Grabarek's work is shown in Zukas (1982) as increase in ballistic limit versus yaw (degrees). It was underlined that, for small yaw angles up to 3 percent, increase in the ballistic limit is around 1 percent while for high angles of obliquity; this critical yaw angle may become less than 1 percent. Another outcome was that, when yaw angles become greater, the effect on the increase in ballistic limit appears to be significant.
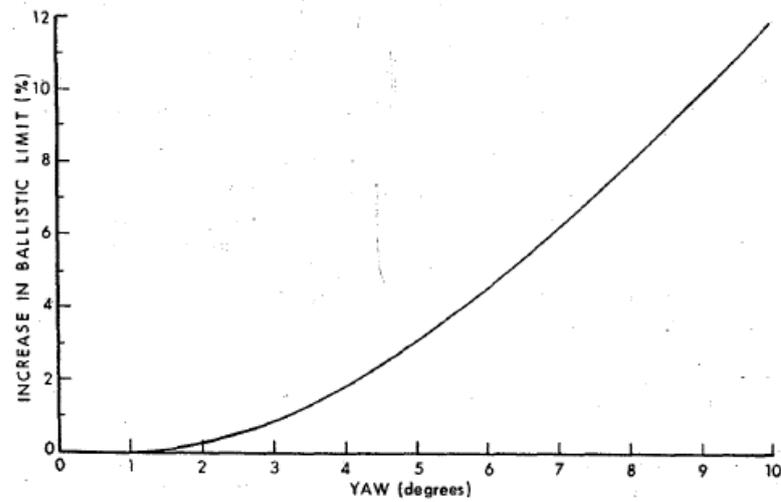
Figure 2.26: Effect of yaw on ballistic limit [Zukas et al., (1982)]

2.4.3   Target Characteristics

2.4.3.1   Material Strength

In impact loading, as the strength of target increases, it becomes harder for the projectile to penetrate, so target material strength, especially concerning concrete, is a very important parameter for the study of penetration and perforation. Many publications and studies are available on this topic and one of them is Li and Tong, (2003). The summary below is based on information gathered from this paper.

In the penetration stage of the projectile, the resisting force on its nose plays an important role determining its motion. The damage of the concrete target impacted with a rigid projectile consists of a conical crater with kd (here, k is assumed to be 2) depth and a tunnel with the projectile shank diameter d. The projectile is assumed to be a rigid body where Newton's second law is applied as:

$$M * \frac{dV}{dt} = F_R \qquad\qquad (2.24)$$

38

F_R is resisting force applied on the nose of the projectile, which is a very important issue in terms of penetration mechanics.

$F_R = \xi * c$, while ξ is crater depth and $< kd$

The axial resistant force on the projectile nose has the form of Poncelet's formula. The dynamic cavity expansion analysis shows the following relation between the normal compressive stress σ_n and normal expansion velocity v as given by Forrestal et al., (1994) with Li and Chen, (2003).

$$\sigma_n = S * f_c + \rho * v^2 \tag{2.25}$$

$$v = V_0 * \cos\theta \tag{2.26}$$

ρ is density f_c is compressive strength of the concrete

$$S = 82.6 * f_c^{-0.544} \tag{2.27}$$

After calculations, c becomes:

$$c = \frac{\pi * d}{4 * k} * \left(\frac{N^* * \rho * V_0^2 + S * f_c}{1 + \frac{\pi * k * d^3}{4 * M} * N^* * \rho} \right) \tag{2.28}$$

N^* is a nose shape factor.

From the equation it can be realized that, as the concrete strength increases, the resisting force increases, which makes it harder for the projectile to penetrate. A sketch of the nose and angles discussed can be seen in Figure 2.27
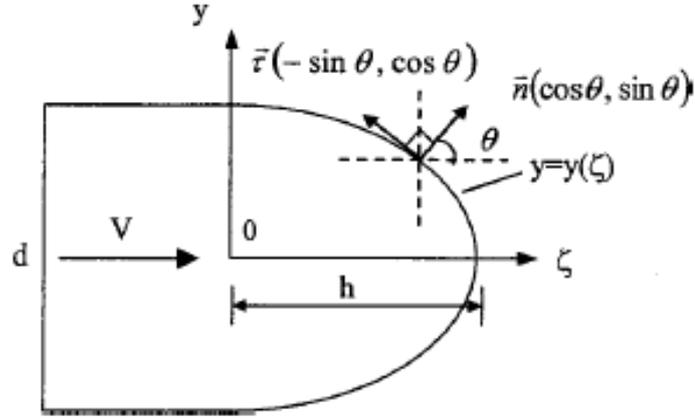
Figure 2.27: A view of the nose named in the study [Li and Tong, (2003)]

If impact velocity is high enough, plug formation occurs. The shape of the plug can be considered as a cone. α, the cone plugging angle, is an important parameter for the shape of the plug. H_p is the plugging depth In the study of Dancygier, (1998), for normal strength concrete, 66 degrees and for high strength concrete, 76 degrees are taken as average values for α. In the formulae used below, α is taken as 70 degrees. Plug formation is related to shear failure in the formulation, as maximum shear stress under uniaxial compression increases, the total resistance force on the shear surface increases. The corresponding shear stress is given as:

$$\tau_f = \frac{1}{\sqrt{3}} * f_c \tag{2.29}$$

$$F_s = \tau_f * A_s * \cos\alpha \tag{2.30}$$

$$A_s = \frac{1}{\cos\alpha} * (d * H_p * \pi + H_p^2 * \pi * \tan\alpha) \tag{2.31}$$

Perforation thickness which is named as minimum thickness of the target resisting projectile impact is determined by.

$$F_S = F_R \tag{2.32}$$

40

τ_f is maximum shear stress under uniaxial compression and as can be seen when concrete strength increases, shear stress increases, which results in increase in resisting force and making penetration harder. The scheme of the plugging work is shown in Figure 2.28 below.
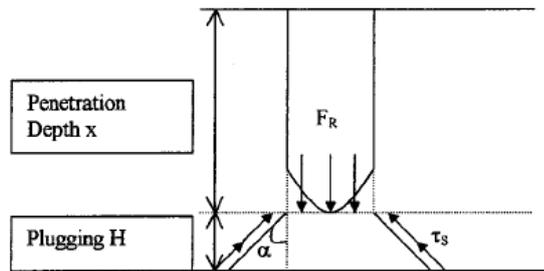
Figure 2.28: Scheme of the plugging work [Li and Tong, (2003)]

In Figure 2.29, which contains test results of Hanchak et al., (1992), dimensionless ballistic limit and different $\dfrac{t}{d}$ for different concrete strengths are plotted. V_{BL} is ballistic limit, d is diameter of the projectile, M is projectile mass, f_{cn} is nominal strength of the concrete target. The same figure shows that there is an increase in concrete strength as the dimensionless ballistic limit increases.
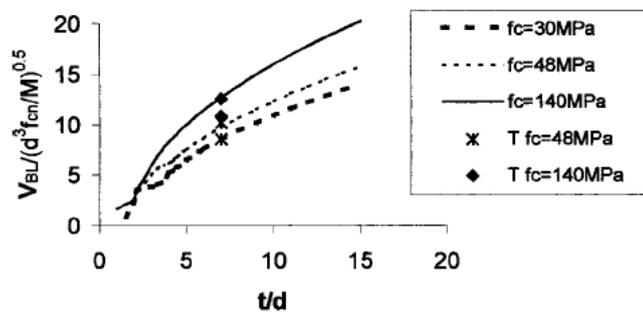
Figure 2.29 Effect of concrete strength on dimensionless ballistic limit [Hanchak et al., (1992)]

41

2.4.3.2   Density

In penetration dynamics the density of target and projectile play an important role. Their effect depends on which velocity regime the impact loading takes place. When the target density increases, depth of penetration decreases, and hydrodynamic velocity (where the target behaves like a fluid and material resistance can be ignored), comes into being at lower velocities. For lower velocities, the density of the target is less important, while around the hydrodynamic velocity, it has a significant importance. [Daneshjou et al., (2005)]

With regard to specific studies related with concrete which are mentioned in Yankelevsky, (1997), for normalized penetration depth and perforation velocity in the U.K. Atomic Energy Authority formula recommends that:

$$G = \frac{3.8 * 10^{-5} * N * m * V_i^{1.8}}{f_c^{0.5} * d^{2.8}} \tag{2.33}$$

$$G = 0.55 * z - z^2 \quad \text{for} \quad z = \frac{x}{d} < 0.22 \tag{2.34}$$

$$G = \left(\frac{z}{2}\right)^2 + 0.0605 \ \text{for} \ 0.22 < z < 2 \tag{2.35}$$

$$G = z - 0.9395 \quad \text{for } z > 2 \tag{2.36}$$

$$V_c = 1.3 * \rho^{1/6} * f_c^{1/2} * \left(\frac{p * e^2}{\pi * m}\right)^{2/3} * (r + 0.3)^{1/2} \tag{2.37}$$

ρ = concrete density (kg/m3),

p = missile perimeter (m),

d = missile diameter (m),

e = concrete thickness (m),

m = missile mass (kg),

r = reinforcement quantity (percent) and,

f_c = ultimate compressive strength of concrete (Pa)

V_c = Perforation velocity

As can be seen, increase in concrete density results in increase in perforation velocity.

2.4.3.3   Ductility

Toughness of a material is the amount of energy that can be absorbed by it. Energy required for the fracture of a brittle material is smaller than that required for a ductile one.

In Chinella et al., (1998), experiments conducted with austempered ductile irons (ADIs). To obtain an austempered ductile iron [ADI], heat treatment has to be applied. In the Warrick et al. (2000) paper, Figure 2.30 the difference between a ductile iron and an austempered ductile iron is shown clearly. In the same source again by the help of Figure 2.30, this information is given: The starting value for the strength data of austempered ductile iron is approximately where the point of strength of conventional iron grades does not exist. Plus, even softest ADI shows higher elongation than the harder and stronger ductile iron grades.
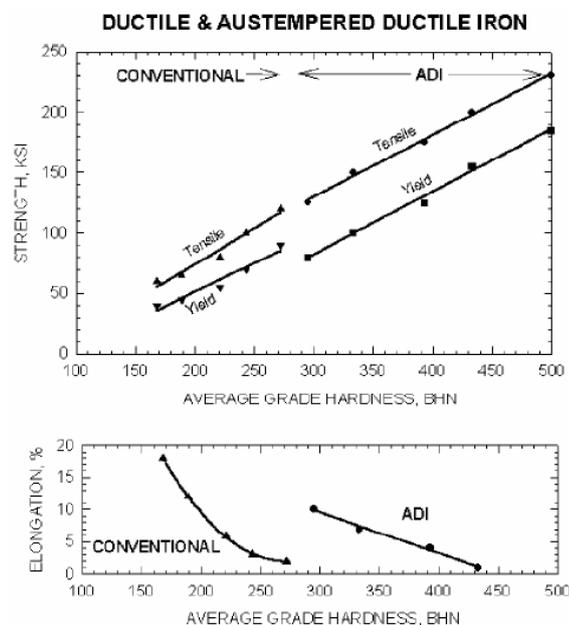
Figure 2.30 Differences of austempered and conventional ductile iron [Warrick et al. (2000)]

43

In the report Chinella et al., (1998), ballistic limit velocities obtained with the 0.50-cal. APM2 projectiles (AP, hardened steel core) struck at ADI targets which had been austempered to lower values of hardness and strength, but gaining greater toughness and ductility provided higher ballistic limit velocities than the one conducted with ADI target with higher values of hardness and strength.

In the report, it was concluded that as ductility of the target increases, ballistic limit velocity increases resulting in higher resistance to perforation. Concrete is the material used in the experiments, results from which are compared with the computation results from the present thesis. Concrete is a semi-brittle material. In order to increase toughness, fracture energy and ductility of the concrete, steel fibers can be added in the construction stage of it or a different material SIFCON (Slurry Infiltrated Fiber Concrete) can be used. Adding steel fiber to concrete results in higher ductility, fracture energy, toughness and tensile strength compared to plain concrete. By using SIFCON, much higher toughness, fracture energy, ductility values and a great amount of increase in tensile and compressive strength compared to steel fiber reinforced concrete (SFRC) can be obtained. The comparison of stress-strain curves can be seen in Figure 2.31. Brief information about the response of SIFCON and SFRC concerning impact loading parameters is given in the section titled Reinforcement Section. Further information about the characteristics of concrete, steel fiber reinforced concrete and SIFCON materials used in the experiments and computations will be given in Chapter 3.
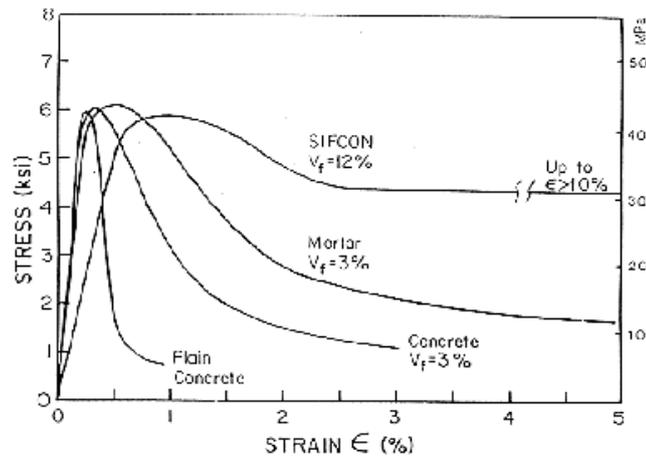
Figure 2.31: Comparison of experimentally observed stress-strain curves of plain concrete, fiber reinforced concrete and mortar, and SIFCON [Li et al., (1989)]

2.4.3.4   Reinforcement

Carrying tensile stresses, preventing crack formation, splintering, scabbing and spalling are said to be the primary functions of steel reinforcement when the target they are placed subjected to impact loading in TM5-855-1, (1984). Unfortunately, increase in percentage of steel along the projectile direction is not sufficient to warrant resistance to penetration. In general steel reinforcement would consist of the following three components, each of which contributes its own share toward inhibiting mass cracking and breaching of the concrete slabs, walls, or roofs subjected to direct hits. TM5-855-1, (1984) provides the following explanations:

- Front face mat: is used to reduce spall area where projectile hits the target and to hold some of the devastated front crater material in place. Taking as a whole, it increases the slab resistance to the repeated shots same general area subjected to.

45

- Back face mat: is used to decrease back scabbing and it also raises the scabbing limit velocity and increase target resistance to inward bending.

- Shear steel: ties both face mats to each other and with concrete body.

In Dancygier (1997), it was implied that the influence of the reinforcing mesh could be seen in the ultimate mode of deformation when a failure surface (crack) occurs, and makes reinforcement activate a dowel action. When steel deforms, a tension force is applied. This causes further cracking of the concrete cover and of the inner portion of the concrete at the crater plug as described in Figure 2.32. In Figure 2.33, the deformed shape of the target reinforcement used in the experiment can be seen.
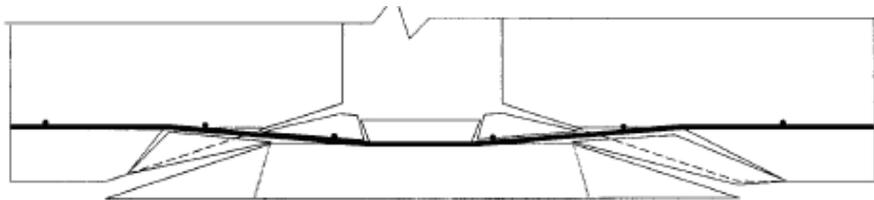
Figure 2.32: Failure process at rear faces [Dancygier, (1997)]
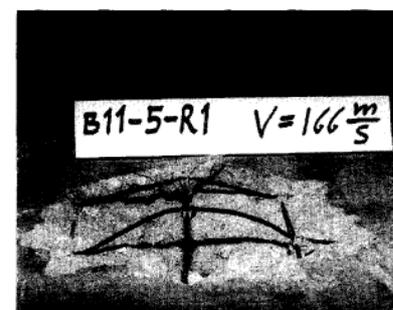
Figure 2.33: Deformed shape of the reinforcement after experiment of impact loading [Dancygier, (1997)]

46

It was concluded that there is a certain reinforcement ratio such that, over this ratio, the reinforcing steel becomes more effective, and improves the element resistance against perforation. When the reinforcement ratio is higher, the element perforation resistance to hard projectile impact becomes higher. Reinforcement inclination, normal to the cracked surface, at ultimate conditions also improves its contribution to the perforation resistance. The U.K. Atomic Energy Authority formula which is mentioned in the density part of this chapter also takes into account the effect of reinforcement quantity while perforation velocity is calculated.

2.4.3.4.1 SIFCON

Many studies have been conducted regarding SIFCON properties. One of them is Rao et al., (2009), information taken from which is summarized in this section. In this reference SIFCON is said to be a special fiber-reinforced concrete. In SIFCON, the matrix is made of flowing cement mortar slurry while it is aggregate concrete in normal fiber-reinforced concrete. Another difference is that fiber reinforced concrete contains 1–3 percent fibers by volume normally; SIFCON contains 6–20 percent of fibers. SIFCON may be a new construction material but it has found applications in the defense structures since it provides excellent energy-absorption capability and, because of its extraordinary ductility characteristics, it has great potential for applications in structures subjected to impact and dynamic loading.

In the same paper, in order to understand the magnitude of energy absorption which is a very important parameter for impact loading, experimental has also been conducted. The characteristics of the specimens and test results are shown in the following Table 2.7.

47

Table 2.7: Test results for different types of concrete impact strength [Rao et al., (2009)]

S.No	Nomenclature	Number of blows to cause first crack impact strength	Number of blows at ultimate impact strength	28-day compressive strength of control cubes (fck)	28-day split tensile strength of control cylinders (ft)
1	S-8	7516	40700	44.93	10.75
2	S-10	13750	67466	51.57	12.01
3	S-12	26950	82133	54.77	12.91
4	SR-8	94600	162800	44.93	10.75
5	SR-10	111100	192500	51.57	12.01
6	SR-12	137500	242000	54.77	12.91
7	FR-2	213	40150	32.0	4.62
8	F-2 100	7406	32.0	4.62	
9	RCC	27	11550	20.1	3.73
10	PCC	-	10	20.1	3.73

S-# = SIFCON slab without conventional steel reinforcement containing # percentage of volume fiber

SR-# = SIFCON slab with conventional steel reinforcement containing # percentage of volume fiber

F-# = FRC slab without conventional steel reinforcement and containing # percentage of volume of fibers

FR-# = FRC slab with conventional steel reinforcement and containing # percentage of volume of fibers

RCC = Reinforced Cement Concrete slab with Conventional steel reinforcement

PCC = Plain Cement Concrete slab

Failed SIFCON Specimens after test can be seen in Figure 2.34

S-8 After 40700 no of blows   S-10 After 67466 no of blows
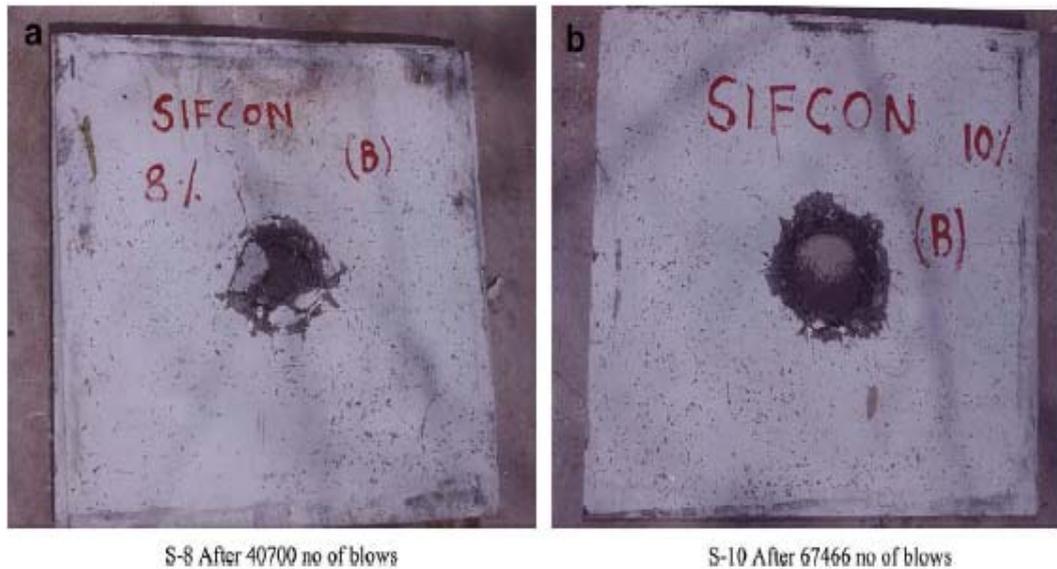
Figure 2.34: Failed SIFCON specimens without conventional reinforcement- a-) containing 8 percent fiber b-) containing 10 percent fiber [Rao et al., (2009)]

From an examination of the test results, it was concluded that: The SIFCON slabs can absorb more energy than the FRC and RCC slab specimens both at first crack and at ultimate impact strengths and energy-absorption capacity of SIFCON slabs increases with greater fiber volume values. In addition, energy-absorption capacity of unreinforced SIFCON slabs are 1.32 percent, 451 percent, 253 percent and 415,809 percent higher compared to unreinforced FRC, RCC and PCC slabs at ultimate stage. Damage under impact in reinforced SIFCON slabs is less than SIFCON slabs without conventional reinforcement while, damage in FRC and RCC slabs is more than that in SIFCON ones.

Further information about SIFCON will be given in the Chapter 3 of the thesis.

2.4.3.4.2 Steel Fibre Reinforced Concrete (SFRC)

Studies on SFRC have also been carried out to assess its impact resistance and, on this subject, many publications are available. The rest of the information

in this chapter has been obtained from Bentur and Mindess, (2006) and may be summarized as follows:

SFRC has much better properties under impact loading than plain concrete considering strength and fracture energy. The role of the fibers is essentially, controlling the crack by bridging them in the matrix. Also, under impact loading, fracture energy values of SFRC can be 70-80 percent and strength values can be 50-100 percent higher than those under static loading. Behavior of SFRC and plain concrete can be seen in Figure 2.35. In Bentur and Mindess, (2006), it is mentioned that as strain rates increases from $1.25*10^{-6}$ m/s to 20 m/s, SFRC tensile strength increases 70 percent , so as maximum strain by amount 25 percent and fracture energy by 60 percent does, which is quite favorable for impact loading. So, in Bentur and Mindess, (2006), it was stated that the ACI Committee 544 recommends SFRC to be used to improve dynamic and impact loading resistance. Behavior of SFRC and plain concrete can be seen in Figure 2.35.
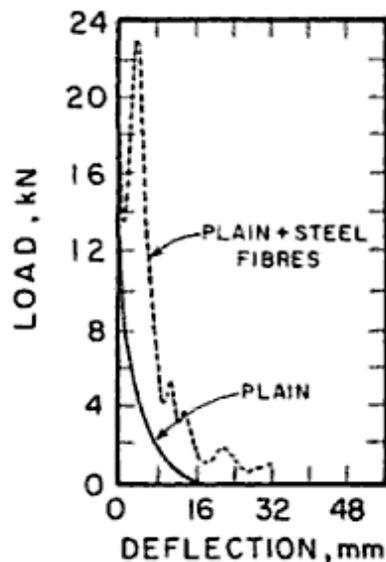
Figure 2.35: Behavior of plain concrete and SFRC under impact loading -drop-weight machine [Bentur and Mindess, (2006)]

In Bentur and Mindess, (2006) it is said to be shown by references that, steel fiber used with conventional reinforcement increases ultimate moment and ultimate deflection, however, from another reference of Bentur and Mindess, (2006), it is also expressed that use of compression steel reduces the beneficial effect of steel fibers. This phenomenon is illustrated in Figure 2.36.
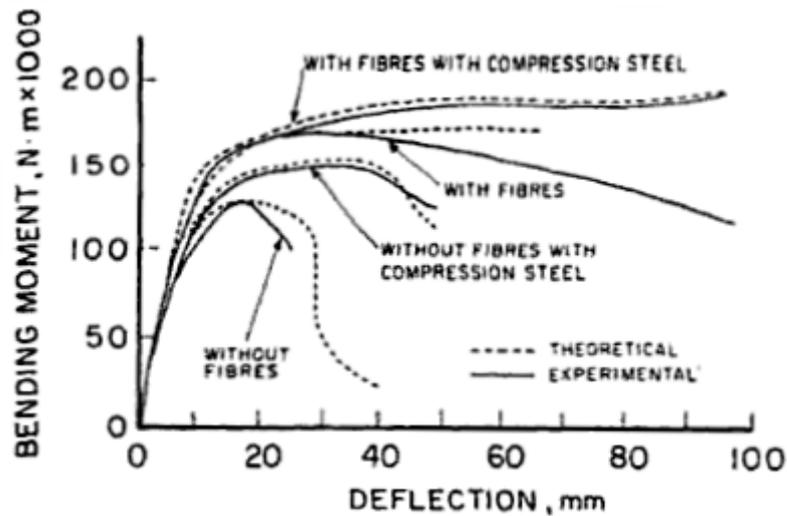
Figure 2.36: Bending moment versus deflection for different concrete forms[Bentur and Mindess, (2006)]

Further information related to SFRC will be given in the Experimental Environment Chapter of the thesis.

2.4.3.5   Thickness

The thickness of the target is an important parameter for perforation and penetration mechanics. As target thickness increases perforation of the projectile becomes harder as mentioned in TM5-855-1(1984), so formulas and nomograms are used to obtain approximate effects of projectiles and bombs on concrete targets.

51

In Yankelevsky, (1997), formulas of how concrete penetration, perforation depths are calculated depending on several parameters can be found and are listed below

- The Army Corps of Engineers Formula:

$$\frac{x}{d} = \frac{282 * D^* * d^{0.215}}{(f_c')^{1/2}} * (\frac{V_0}{1000})^{1.5} + 0.5$$

(2.38)

D^*: the missile caliber density (W/d^3) in (lbs/in^3)

f_c' = ultimate concrete compressive strength (psi)

e: perforation thickness

Perforation depth is given as:

$$\frac{e}{d} = 1.32 + 1.24 * (\frac{x}{d}) \quad for \quad 3 \leq \frac{e}{d} \leq 18$$

(2.39)

- The Modified NDRC Formula

$$G(\frac{x}{d}) = K * N * d^{0.2} * D * (\frac{V_0}{1000})^{1.8}$$

$$G(\frac{x}{d}) \begin{cases} \left(\frac{x}{2*d}\right)^2 for \frac{x}{d} \leq 2 \\ \left[\left(\frac{x}{d}\right) - 1\right] for \frac{x}{d} \geq 2 \end{cases}$$

(2.40)

$$K = 180 / (f_c')^{1/2}$$

(2.41)

N = 0.72 for flat nose-1.0 for average bullet nose

For large slab thickness/missile diameter formulae:

$$\frac{e}{d} = 1.32 + 1.24 * (\frac{x}{d}) \quad for \quad 3 \le \frac{e}{d} \le 18 \tag{2.42}$$

For small slab thickness/missile diameter formulae:

$$\frac{e}{d} = 3.19 * \left(\frac{x}{d}\right) - 0.718 * \left(\frac{x}{d}\right)^2 \quad for \frac{x}{d} \le 1.35 \tag{2.43}$$

- The Ballistic Research Laboratory Formula

In this formula, perforation thickness is proposed as:

$$\frac{e}{d} = \frac{427}{\left(f_c'\right)^{1/2}} * D * d^{0.2} * (\frac{V_0}{1000})^{1.33} \tag{2.44}$$

- The Ammann and Whitney Formula

This formulation is used to predict perforation of the penetration of small explosively generated fragments at relatively high velocities:

$$\frac{x}{d} = \frac{282 * N * D * d^{0.2}}{\left(f_c'\right)^{1/2}} * \left(\frac{V_0}{1000}\right)^{1.8} \tag{2.45}$$

- The Haldar Formula

All the parameters are identical with NDRC except an additional parameter called *I* (impact factor) is defined,

$$I = \frac{W * N * V^2}{g * d^3 * f_c'} \tag{2.46}$$

53

Correlation of experimental results and impact factor yielded penetration depth predicted to be:

$$\frac{x}{d} = -0.0308 + 0.25251 * I \quad \text{for} \quad 0.3 \le I \le 4 \tag{2.47}$$

$$\frac{x}{d} = 0.6740 + 0.567 * I \quad \text{for} \quad 4 \le I \le 21 \tag{2.48}$$

$$\frac{x}{d} = 1.1875 + 0.0299 * I \quad \text{for} \quad 21 \le I \le 455 \tag{2.49}$$

- The Kar Formula

By using regression analysis, Kar developed the formula below:

$$G(\frac{x}{d}) = \frac{180}{\left(f_c'\right)^{0.5}} * N_2 (\frac{E}{E_m})^{1.25} * \frac{W}{D^* * d^{1.8}} (\frac{V}{1000})^{1.8}$$

(2.50)

N_2 = nose shape factor

E, E_m = Modulus of elasticity of target and missile

Penetration depth x is calculated as:

$$G(\frac{x}{d}) = \begin{cases} \left(\frac{x}{2*d}\right)^2 & for \frac{x}{d} \le 2 \\ \left(\frac{x}{d} - 1\right) & for \frac{x}{d} \ge 2 \end{cases} \tag{2.51}$$

e is the depth which perforation is prevented while a is the half of the aggregate size in the concrete

$$\frac{e-a}{d} = 3.19 * \frac{x}{d} - 0.718 * (\frac{x}{d})^2 \quad \text{for} \quad \frac{x}{d} \le 1.35 \tag{2.52}$$

$$\frac{e-a}{d} = 1.32 + 1.24(\frac{x}{d}) \quad \text{for} \quad 3 \le \frac{x}{d} \le 18 \tag{2.53}$$

CHAPTER 3

EXPERIMENTAL WORK

3.1   Introduction

Analyses developed for this dissertation are compared with the experiments, details of which are explained in this chapter. These experiments have been supported by TÜBİTAK. In this chapter, firstly, general properties of the SFRC and SIFCON materials will be mentioned. Subsequently, characteristics of target specimens and projectile will be given. Material tests results for the target specimens will be presented at the end. Results of the experiments in terms of initial-residual velocities of the projectile, target front and back face crater volume-radius will be explained in Chapter 5.

3.2   General Information about SFRC and SIFCON

General information obtained through a literature survey about the main characteristics of the target materials used in the experiments will be mentioned in this section.

3.2.1   Steel Fiber Reinforced Concrete (SFRC)

As mentioned in Chapter 2, the main differences between SFRC and SIFCON are matrix and fiber volume. In Rao et al., (2009), differences are

explained as follows: the matrix of SIFCON is slurry flowing cement mortar, whereas in SFRC, this is aggregate concrete; the fiber volume content in SIFCON is between 6-20 percent, while, SFRC values of it is 1-3 percent by volume.

3.2.1.1   SFRC under Compressive Loading

Effect of steel fibers on ultimate strength of concrete is a slight increase up to volume fractions of 1.5 percent [Löfgren, (2005)]. In the paper of Barros and Figueiras (1999), it is claimed that, according to many researchers, the post peak response is different from normal concrete. Fanella and Naaman, (1985) proposed an expression for SFRC in compression using the experimental data and fiber geometry, volume fraction, and fiber shape. Four of eight parameters are used to define the ascending portion and the other four are used to express descending portion. This expression is one parameter dependent and shows the relationship between stress and strain like the expression proposed by Ezeldin and Balaguru, (1992). Methods of Fanella and Naaman, (1985) and Ezeldin and Balaguru, (1992) can be seen in the related papers. Comparison of SFRC compression curves gained by experimental and analytical work done in Barros and Figueiras (1999) are shown in Figure 3.1 for two different fiber contents.
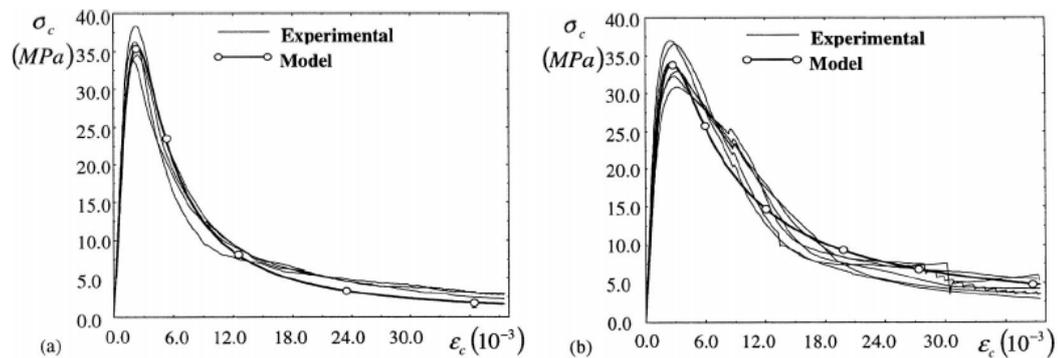
Figure 3.1: Comparison of experimental and analytical SFRC compression curves a-) 30 kg/m^3 of fibers, b-) 60 kg/m^3 of fibers [Barros and Figueiras (1999)]

3.2.1.2   SFRC under Tensile Loading

In Nyström, (2008), it is mentioned that ACI 544 (1996) implies that for 1.5 percent volume fraction of steel fibers, there exists a tensile strength increase of 30 to 40 percent. However the difference between peak loads of normal-strength concrete and SFRC is larger than the same difference in impact loading. In Nyström, (2008), it is said to indicate the decrease of the relative effect of fiber in the concrete.

In the paper of Barros and Figueiras (1999), studies of SFRC response in terms of tensile loading are also described. Three point bending tests were done on notched beams with dimensions 600* 150* 150 mm³ with 450 mm span. An actuator of maximum 250 kN capacity was applied in the test which is done under displacement control condition. Figure 3.2 shows the results obtained from a group of specimen for different fiber reinforcements. By using these curves, fracture energies can be calculated. Since these experimental curves are not available in our experiments, fracture energy is calculated is calculated by the procedure described in Nyström, (2008) in Chapter 4.
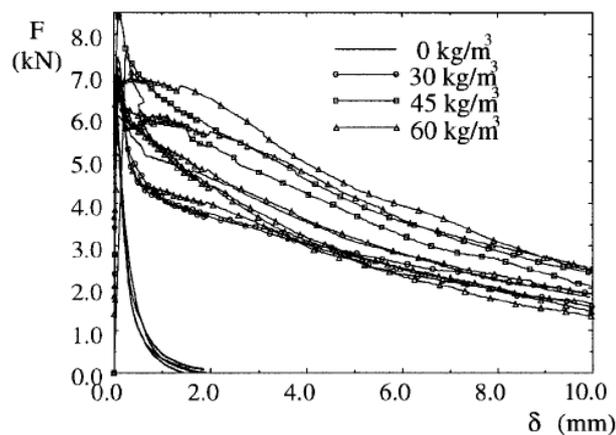
Figure 3.2: Load-displacement relationship obtained from a group of specimen in three-point bending tests of notched beams, [Barros and Figueiras (1999)]

3.2.1.3   SFRC under Bending

In order to examine the moment curvature relationship for slabs with different fiber reinforcement, experiments and modeling studies are conducted by Barros and Figueiras (1999)]. In the experiments, apart from steel fibers, wire meshes were also used and the cross section parallel to slab width contained 40 mm^2 of longitudinal reinforcement. The steel wires had ultimate strengths of 560 and 800 MPa. Fiber amounts for different slabs were 0, 30, 45, 60 kg/m^3. Comparison of modeling with the experimental results can be seen in the Figure 3.3.
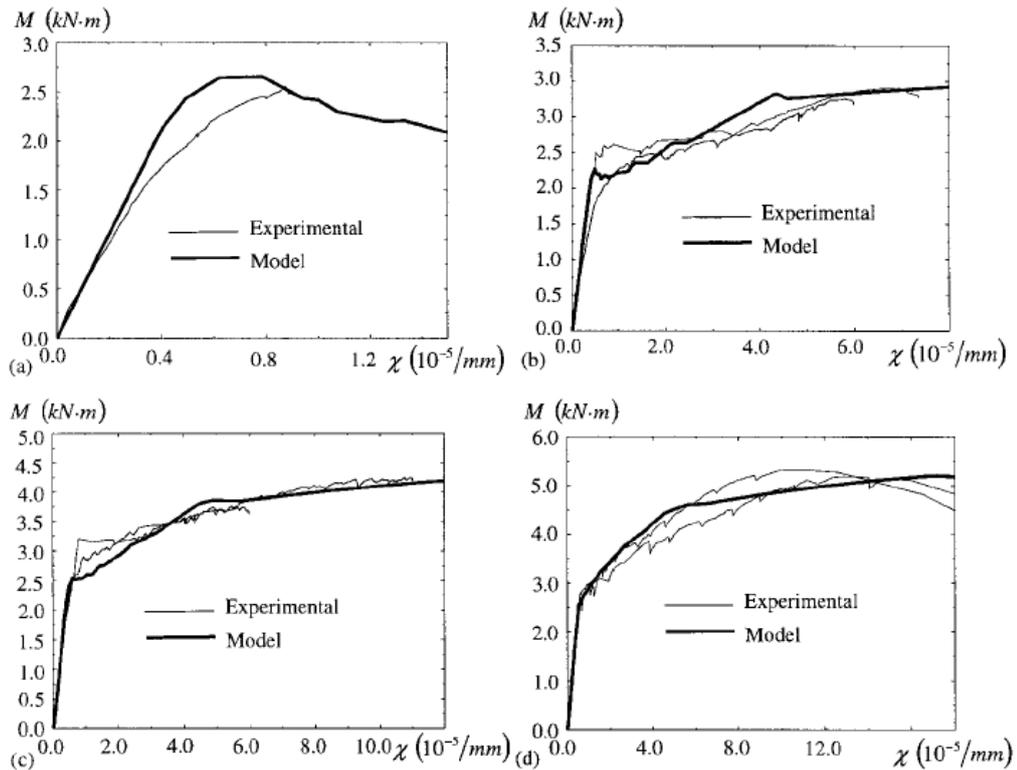
Figure 3.3: Moment-curvature relationship of slab strips reinforced with different amounts of fibers: (a)0 kg/m^3; (b) 30 kg/m^3; (c) 45kg/m^3; (d) 60 kg/m^3[Barros and Figueiras (1999)]

3.2.2 SIFCON

The material description of SIFCON (Slurry Infiltrated Fiber Concrete) mentioned in Marchand et al., (1998), is given as: consisting of high strength steel fibers with low viscosity slurry which has a construction process of 'rain in' the fiber and pouring it into the slurry which is composed of water, cement, fly ash, super plasticizer, and micro silica. At the end of this process, a high strength ductile material which is resistant to dynamic loads is obtained. Many characteristics of SIFCON have been studied but here primary features of compression, tension, bending of it are explained. The energy absorption capacity of SIFCON is treated in Chapter 2.

3.2.2.1   SIFCON under Compressive Loading

A schematic representation of the compression curve of SIFCON is shown in Figure 3.4.
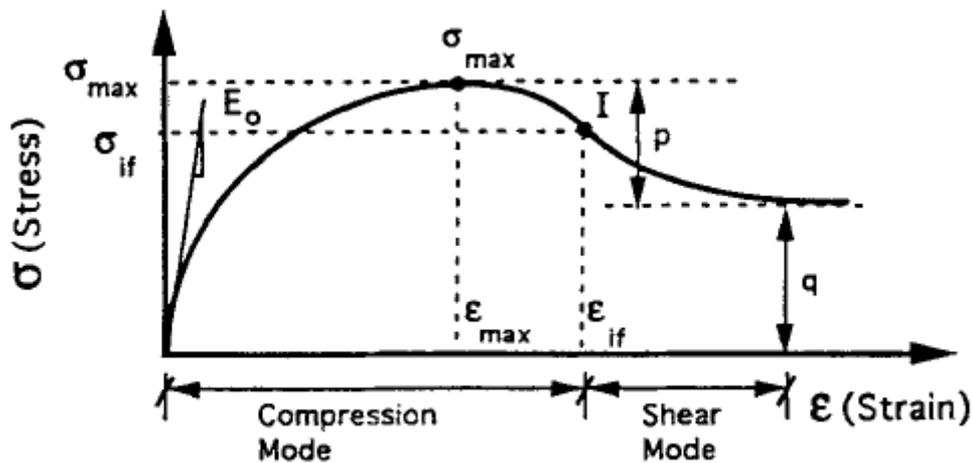
Figure 3.4: Compression curve of SIFCON [Naaman et al., (1993)]

As mentioned in Naaman et al., (1993), the ascending portion of the curve is like plain concrete with the difference of large strain of ε_{max}, at the peak load. The descending portion of the curve reaches a large plateau after an inflection

59

point. This inflection point shows the change in mode of failure from compression to shear. The tail part shows shear sliding along the main inclined crack. In Marchand et al., (1998), for the higher strength SIFCON compressive strength can be seen as 53.78-89.63 MPa are reported. At increasing dynamic strain rates of 100 -200/sec., the ratio of compressive strength at strain rate to f_c is 1.4 to 1.0. Compressive modulus of different types of SIFCON varies from 6895-12066 MPa whereas this value is 27579 -34474 MPa for normal concrete. This difference results in higher strain energy absorbtion in SIFCON.

3.2.2.2   SIFCON under Tensile Loading

The paper by Naaman et al., (1993) explained tensile behavior of SIFCON by means of the Figure 3.5 below.
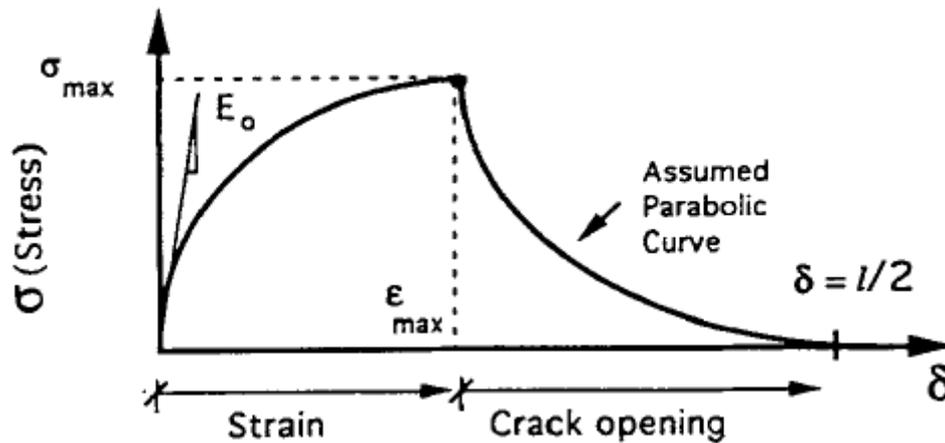
Figure 3.5: Tension curve of SIFCON [Naaman et al., (1993)]

It was implied that, since the average value of the strain can be converted into elongation, the peak load would be translated to a stress-strain curve but the descending portion is defining the opening of a single crack. In Nyström, (2008), the critical crack opening is mentioned to be dependent mainly on the fiber length and can be between $l/2 - l/10$ mm. In Marchand et al., (1998), the tensile

strength of SIFCON is said to be approximately 10-15 percent of the compressive strength which is twice the value of normal concrete and is more ductile reaching 2.5 percent strain.

3.2.2.3   SIFCON under Bending

According to the test conducted to examine the difference between SIFCON beams with DRAMIX 30/50 and reinforced concrete, the maximum tested load for the plane which is perpendicular to the referred fiber orientation was 60051 N, and the load tested for the plane which is parallel to referred fiber orientation is 17793 N. The modulus of rupture for 60051 N loading is 15.17 MPa and for 17793 N, it is 4.34 MPa. Using these values, the maximum moments for these two loads are 2635 Nm and 754 Nm respectively.

On the other hand, these values of maximum moment could be obtained for reinforced concrete beams with 34.47 MPa concrete strength and 344.74 MPa yield strength of reinforcement for 0.75-1.0 percent tensile reinforcement.

3.3   TÜBİTAK Project No: 106M497 Experiments

As part of the scope of TÜBİTAK Project No: 106M497, experiments concerning the impact weapon resistance of reinforced concrete, SFRC, and SIFCON specimens were conducted. Unfortunately not all of the specimens had high speed camera views with velocity data, hence only those which did will be compared with the computation results mentioned here. From this point on, all of the information regarding the experimental work including figures and tables are taken from Gülkan et al. (2009). Consequently, the characteristics of these specimens, material test results of them, features of projectile and execution of experiments will be given in the Sections 3.3.1, - 3.3.4. Results of these experiments in terms of crater depth-diameter with impact-residual velocity will be given together with computational results of the dissertation in Chapter 5.

3.3.1 Target Specimens

In this section, target specimens used in the experiments, their contents and characteristics with reinforcement configurations will be explained.

3.3.1.1   Reinforced Concrete Specimens

These specimens, properties of which can be seen in Table 3.1, do not contain fiber of any type, only reinforcement steel. There are low (C30) and high (C55) compressive strength specimens. Although high strength concrete was expected to be C70, it turned out to possess C55 strength, similarly, low strength concrete was expected to be C25 strength but it showed C30 strength according to the material tests. Henceforth, it will be referred to as C55 instead of C70 and C30, instead of C25. Features of concrete and reinforcement steel with its configuration in the specimen will also be mentioned consequently.

Table 3.1: Properties of the reinforced concrete specimens

No	Dimensions (m)			Compressive strength (MPa)	Reinforcement configuration (mm)	Fiber content (%)	Type of cement
	Length	Width	Depth				
1-1	2	2	0.4	30	$17\phi18$-$\phi10/20$	-	PC 42.5
1-2	2	2	0.4	55	$17\phi18$-$\phi10/15$	-	PC 42.5
1-3	2	2	0.6	30	$17\phi22$-$\phi10/20$	-	PC 42.5

PC = Portland Cement

3.3.1.1.1 Concrete

Content of the concrete mixtute is given in Table 3.2. The distribution of the aggregates and their characteristics are given in Table 3.3, -Table 3.5.

Table 3.2: Content of concrete mixture

Material	C30	C55
Portland cement 42.5 (kg/m^3)	305	650
Fly ash (kg/m^3)	80	196
Water (kg/m^3)	177.7	223.7
Fine aggregate (kg/m^3)	936	411
Coarse aggregate (kg/m^3)	848	744
Normal plasticizer (kg)	2.44*	-
Hyper plasticizer (kg)	-	16.9**

* 0.8 percent of cement

** 2 percent of cement

Table 3.3: Aggregates used in C30 concrete

0-4 mm		8-16 mm		16-25 mm	
Siew	Undersize (%)	Siew	Undersize (%)	Siew	Undersize (%)
4	100	16	92	25	100
2	73	14	69	22.4	82
1	52	12.5	50	20	50
0.5	35	11.2	36	16	7
0.25	23	10	21	-	-
0.063	12	8	8	-	-

Table 3.4: Distribution of the aggregates used in C55 concrete

0-4 mm		8-16 mm	
Siew	Undersize (%)	Siew	Undersize (%)
4	100	16	92
2	73	14	69
1	52	12.5	50
0.5	35	11.2	36
0.25	23	10	21
0.063	12	8	8

Table 3.5: Characteristics of aggregates used in C30 and C55

	0-4 mm	8-16 mm	16-22.4 mm
Density (g/cm^3)	2.65	2.7	2.7
Water Absorption Capacity, (%)	1.65	0.55	0.48

3.3.1.1.2 Reinforcement

According to TM 5-855-1, (1998), Fundamentals of Protective Design For Conventional Weapons, A 615 Grade 400 is recommended to be used for protective structures, the features of which coincide with S 420a type of steel in TS 708 (1996). The percentage of steel is 0.5 percent of the cross sectional area of the specimen in both directions for all top, bottom and middle parts. Mechanical characteristics of S 420a type of steel are given in Table 3.6, and the configuration of reinforcement used in the specimens is shown in Figure 3.6 and Figure 3.7.

Table 3.6: Reinforcement steel mechanical features, [TS 708, (1996)]

Mechanical Characteristics	Hot-rolled			Cold-rolled		
	S 220a	S 420a	S 500a	S 420b	S 500bs	S 500bk
Minimum Yield Strength (MPa)	220	420	500	420	500	500
Minimum Tensile Strength (MPa)	340	500	550	550	550	550
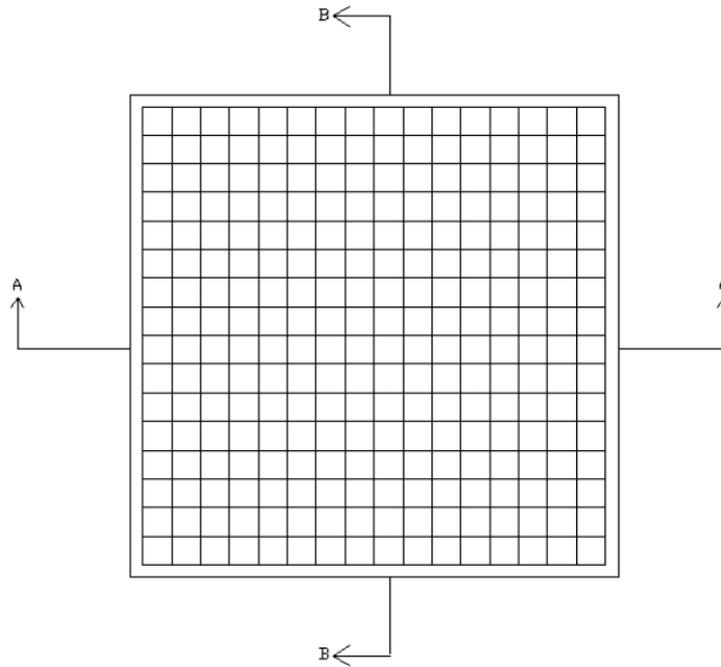
Figure 3.6: Plan view of the reinforcement configuration
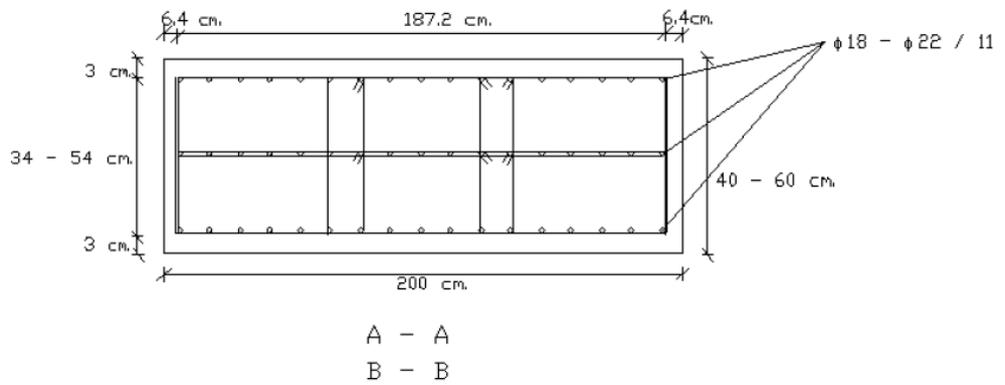
Figure 3.7: Cross-sectional view of the reinforcement configuration

3.3.1.2   Steel Fiber Reinforced Concrete (SFRC) Specimens

During construction of SFRC, in one of the specimens Portland cement 42.5, in other of the specimen, calcium aluminate cement was used. Since no high

speed camera images are available for specimens containing calcium aluminate cement, they will not be mentioned.

In SFRC specimens, the same reinforcement configuration of the reinforced concrete specimens is used. Adding to this configuration, these specimens also contain 2 percent volumetric content of steel fiber Dramix RC - 80/60- BN. Properties of the Portland cement used specimens are given in Table 3.7 below. Information about both concrete and reinforcement will be given in the next sections.

Table 3.7: Properties of the SFRC specimens

No	Dimensions (m)			Compressive strength (MPa)	Reinforcement configuration (mm)	Fiber content (%)	Type of cement
	Length	Width	Depth				
2-2	2	2	0.6	61	$17\phi22$-$\phi10/20$	2	PC 42.5
2-3	2	2	0.6	61	$17\phi22$-$\phi10/20$	2	PC 42.5

3.3.1.2.1 Concrete

Content of the concrete mixture is shown in Table 3.8 below. The distribution of the used aggregates and their characteristics are given in Table 3.9, Table 3.10.

Table 3.8: Content of the concrete mixture

Material	Specimens 2-1, 2-2, 2-3
Portland cement 42.5 (kg/m^3)	400
Fly ash (kg/m^3)	30
Water (kg/m^3)	170
Fine aggregate (kg/m^3)	1091
Coarse aggregate (kg/m^3)	730
Hyper plasticizer (kg)	5.20
Steel fiber (kg/m^3)	40

Table 3.9: Distribution of the aggregates used in the SFRC concrete

0-4 mm		0-7 mm		7-15 mm	
Siew	Undersize (%)	Siew	Undersize (%)	Siew	Undersize (%)
16	100	16	100	16	100
8	100	8	100	8	57.31
4	91	4	92.74	4	5.95
2	60	2	59.18	2	2.83
1	41	1	38.46	1	2.56
0.5	30	0.5	27.25	0.5	2.42
0.25	23	0.25	20.48	0.25	2.27
0.125	17	0.125	14.03	0.125	1.37

Table 3.10: Characteristics of aggregates used in SFRC concrete

Aggregate size	0-4 mm	8-16 mm	16-22.4 mm
Density (g/cm^3)	2.66	2.61	2.65
Water absorption capacity, (%)	1.22	2.20	0.80

3.3.1.2.2 Reinforcement

As mentioned, the same configuration of reinforcement steel was used in these specimens.

3.3.1.2.3 Steel Fibers

Specimens contain Dramix RC -80/60- BN steel fibers of 2 percent by volume (40 kg/m^3). Dramix RC -80/60- BN is a cold drawn wire fiber, with hooked ends, and glued in bundles. [Dramix RC-80/60-BN, (2005)]. Characteristics and view of Dramix RC -80/60- BN is shown in Table 3.11 and Figure 3.8.

67

Table 3.11: Characteristics of Dramix RC -80/60- BN

Characteristics	Explanation
R	Hooked-end
C	Glued fiber
B	Bright
N	Low carbon
Length (mm)	60 mm
Diameter (mm)	0.75 mm
Aspect ratio	80
Tensile strength (MPa)	1050
Coating	None
Number of fibers/kg	4600

Figure 3.8: View of Dramix RC -80/60- BN

3.3.1.3 Slurry Infiltrated Fiber Concrete (SIFCON)

The matrix of SIFCON is slurry flowing cement mortar [Rao et al., (2009)], so the composition of SIFCON is very different from SFRC. In these experiments, Dramix RL -45/30- BN fibers with 12 percent volume contents were used. Although very high compressive strengths (> 140 MPa) could be obtained, material test results revealed that SIFCON specimens used in these experiments have an average compressive strength value of 58 MPa. Properties of the SIFCON

specimens are given for in Table 3.12. Properties of SIFCON concrete and reinforcement will be given consequently.

Table 3.12: Properties of the SIFCON specimens

No	Dimensions (m)			Compressive Strength (MPa)	Reinforcement Configuration (mm)	Fiber Content (%)	Type of Cement
	Length	Width	Depth				
3-2	2	2	0.6	58	-	12	PC 42.5
3-3	2	2	0.6	58	-	12	PC 42.5

3.3.1.3.1 Concrete

The content of slurry flowing cement mortar is given in Table 3.13 as follows:

Table 3.13: Content of slurry flowing cement mortar

Material	Quantity
Portland cement 42.5, (kg/m^3)	1400
Silica fume, (kg/m^3)	50
Water, (kg/m^3)	450
Hyper plasticizer (Glenium 51), (kg)	22
Steel fiber,(kg/m^3)	792

3.3.1.3.2 Steel Fibers

Dramix RL -45/30- BN fibers by 12 percent volumetric content (792 kg/m^3) are used here. Dramix RL -45/30- BN which can be viewed in Figure 3.9 is a loose cold drawn wire fiber, with hooked ends [Dramix RL-45/30-BN, (2005)]. The characteristics of this fiber are given in Table 3.14.

69

Table 3.14: Characteristics of Dramix RL-45/30-BN

Characteristics	Explanation
R	Hooked-end
L	Loose fiber
B	Bright
N	Low carbon
Length (mm)	30 mm
Diameter (mm)	0.62 mm
Aspect ratio	48
Tensile strength (MPa)	1270
Coating	None
Number of fibers/kg	13000

Figure 3.9: View of Dramix RL-45/30-BN

3.3.2 Material Tests

Concrete specimens undergo uniaxial compression and beam deflection tests and reinforcement bars undergo rebar tensile tests. Results of uniaxial compression tests are given in Table 3.15 and beam deflection tests are given in Figure 3.11, Figure 3.12, Figure 3.13 and Figure 3.14.

3.3.2.1 Uniaxial Compression Tests

Compressive strength of the concrete is determined by the uniaxial compression test. In the book of Ersoy et al., (2004), this test is explained in this fashion:

28 day old concrete specimens are tested under monotonic uniaxial compression in order to define their compressive strength. Although in some countries, 200x200x200 mm and 150x150x150 mm cubic specimens are still being used; the universal standard for concrete testing specimen is cylindrical with the diameter 150 mm a height of 300 mm. The ratio of cylindrical strength to the cubic strength varies between 0.7 and 1.1. During experiments, lubrication may be applied to the top and bottom faces of the specimen which are in contact with the loading surfaces.

The material tests for these experiments are conducted with cylindrical specimens. Results are shown in Table 3.15.

Table 3.15: Results of uniaxial compression tests

Specimen No	Specimen age (day)	Average compressive strength (MPa)
1-1, 1-3	28	30
1-2	28	55
2-2, 2-3	28	61
3-2, 3-3	28	58

3.3.2.2 Flexural Strength Tests

In order to determine the flexural strength of the specimen, midspan applied load of flexural strength test is conducted. In the book of Lamond and Pielert (2006), this test is named as ASTM C293 and information about this test is given as follows:

In ASTM C29, testing specimen experiences the maximum moment at the midspan. Sides should be at right angle to the top and bottom faces while surfaces

which are in contact with the loading block being flat. The loading apparatus must apply force perpendicularly to the face of the beam without eccentricity and reactions should be applied parallel to the loading direction. The first half of the load is applied rapidly while afterwards, the loading rate should produce a tensile stress between 861 MPa/min and 1207 MPa/min. The central point loading moment diagram is given in Figure 3.10.
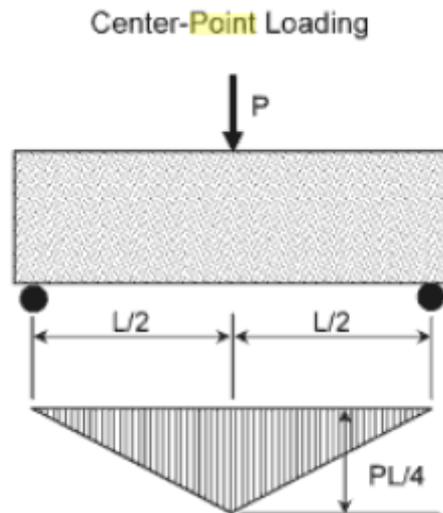
Figure 3.10: Moment diagram of center point loading [Lamond, Pielert , (2006)]

Results of beam deflection test for C30 specimens are shown in Figure 3.11 below.
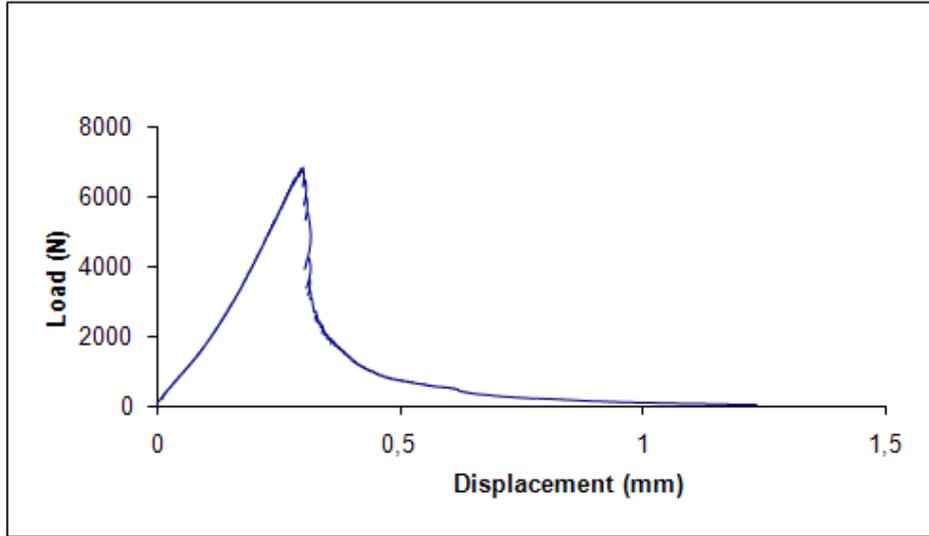
Figure 3.11: C30 Beam deflection test results

Results of beam deflection test for C55 specimens are shown in Figure 3.12 below.
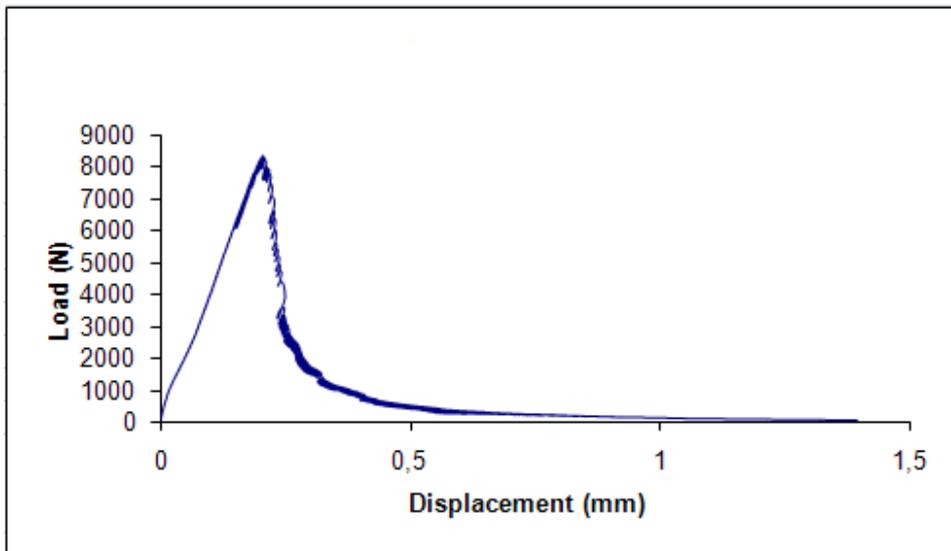
Figure 3.12: C55 Beam deflection test results

Results of beam deflection test for SFRC specimens are shown in Figure 3.13 below.
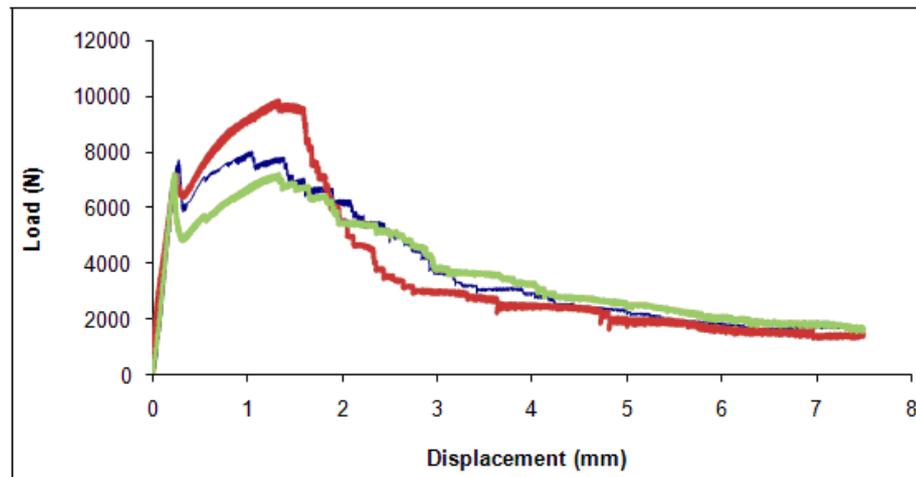
Figure 3.13: SFRC Beam deflection test results

Results of beam deflection test for SIFCON specimens are shown in Figure 3.14 below.
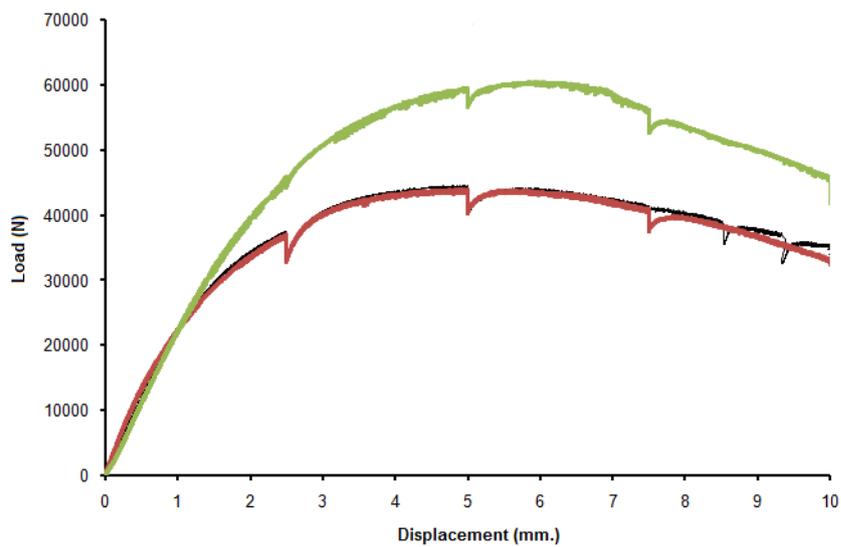
Figure 3.14: SIFCON Beam deflection test results

3.3.2.3   Rebar Tensile Tests

Reinforcement bars of $\phi 10$, $\phi 18$, $\phi 22$ which are used in the specimens, are tested to determine the yield and tensile strengths. In this test, specimens with the same diameter are cut to equal lengths, and by the aid of the testing machine, tensile stress is applied to the both end of the specimens uniaxially and stress-strain curves for specimens are obtained. Table 3.16 shows the results for the material tests of the reinforcement bars used in the experiments.

Table 3.16: Rebar tensile test results for reinforcement bars

No	$\phi 10$		$\phi 18$		$\phi 22$	
	1	2	3	4	5	6
Diameter (mm)	9.85	9.85	18.13	18.13	22.1	22.1
Cross-sectional area (mm2)	76.16	76.16	258	258	383.4	383.4
Yield load (N)	43000	48500	128000	120000	184000	182000
Yield strength (MPa)	564.5	636.5	496	464.8	479.9	474.5
Maximum load (N)	51000	56000	164000	150000	256000	254000
Tensile strength (MPa)	669.6	734.9	635.5	581	667.7	662.1
Length (mm)	100	100	260	260	260	260
Total elongation (mm)	120	118	310	315	306	310
Strain (%)	20	18	19.2	21.2	17.6	19.2

3.3.3   Features of the Projectile

The projectile idealized for this study is similar to one used by the Turkish Armed Forces. The characteristics of the projectile used in the experiments are shown in Table 3.17.

Table 3.17: Characteristics of the projectile

Length of the projectile to strike (mm)	372
Mass (kg)	5.57
Material	Tungsten alloy
Average exit velocity (m/s)	1485

3.3.4   Execution of the Experiments

For reasons of confidentiality, the type of the instrument used to fire the projectile, views of undeformed-deformed specimens, high speed camera images, pictures from the execution of the experiments, or details of this process cannot be given. The only information that can be shared is the configuration of the targets according to their materials which is reported upon in subsequent sections.

3.3.4.1   Reinforced Concrete

Specimens 1-3, 1-1, 1-2 were placed with 2 m distance between them, while 1-3 was the first to face the projectile. The velocity of the projectile was calculated by dividing this fixed distance of 2 m by the necessary time to cross this distance Δt, gained from high speed camera videos. Calculations of projectile velocities for all other group of specimens were done in the same manner.

3.3.4.2   SFRC

2-2 and 2-3 specimens were also placed with 2 m distance between them, and 2-2 was hit by the projectile first.

3.3.4.3   SIFCON

Just as SFRC and reinforced concrete specimens, 3-2 and 3-3 are placed with 2 m difference. Projectile hit 3-2 specimen first.

CHAPTER 4

COMPUTATIONAL WORK

4.1   Introduction

Details and procedure of the analyses, results of which are compared with the experiments, are explained in this chapter. In order to understand the materials' behavior under impact loading, analyses were conducted with ANSYS AUTODYN Version 11.0.00 which is powerful software with its explicit time integration technique usage.

The problem of the dissertation was to determine the failure pattern of concrete targets under high velocity projectile impact loading and to obtain crater radius-volume together with the residual velocities of the projectiles. Analyses were carried out for 2D and axisymmetrical idealization. The dimension of the analyses models for target and projectile were the same in the x axis and half of the experimental one in the y axis. Directions of x and y axes can be seen in Figure 4.1 as projectile heading parallel to being the x axis while the y axis is perpendicular to it. By the help of mirror image (symmetry) option that the software enables, analyses could be observed with actual dimensions. The reason behind conducting analyses in 2D axisymmetric environment instead of the 3D one with actual dimensions was this: since target dimensions were quite large for finite element analysis (2m*2m*0.6m -2m*2m*0.4m), and computer resources were limited, making a simulation in 3D with real dimensions resulted in enormous computational time (1 month or more) even for a larger mesh size. Hence, in order to obtain reasonable results with an appropriate mesh size, analyses were done in 2D and axisymmetrical idealization. Use of axisymmetry

was helpful in reaching the solution much faster compared to actual size modeling in 2D. Reduction of the computation time with the help of 2D and axisymmetry enabled also use of the same projectile in layered targets. Meaning of it is: projectile deformed by striking the former target could be used to strike the latter one with new initial velocity conditions. This was a chance to increase accuracy since in the experimental stage, problem conformed to this idealization. Examples for the view of the undeformed projectile which is about to strike the first target and deformed projectile which is about to strike second target can be seen in Figure 4.1 and Figure 4.2. The pictures were taken from the screenshots of the analyses before projectile hitting first and second SIFCON targets. In these figures projectile and target are colored according to material location whereas in general of the thesis, pictures of analyses are colored according to material status.
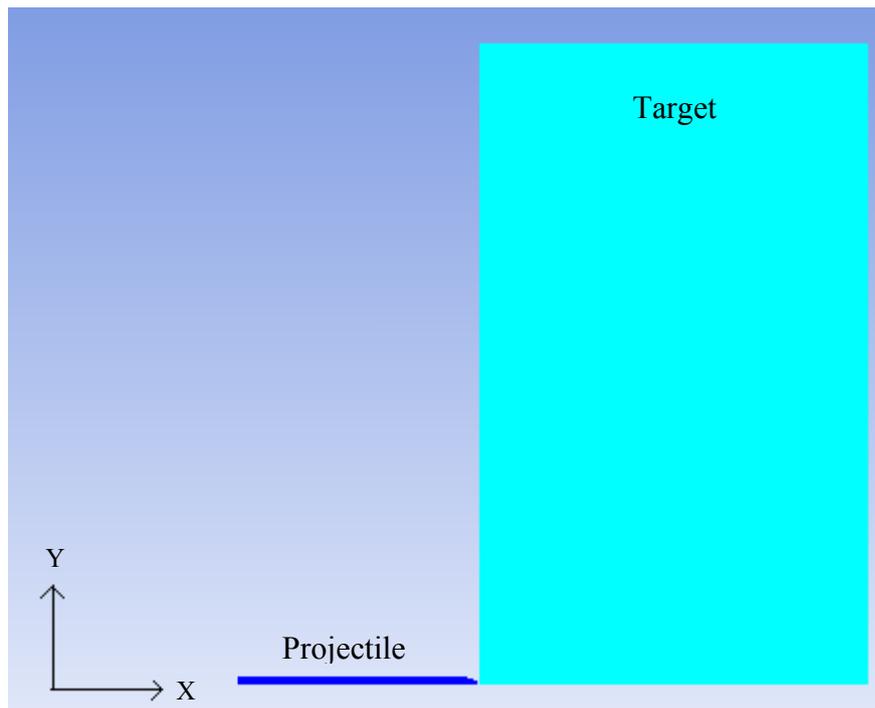
Figure 4.1: Undeformed projectile- first SIFCON wall before strike
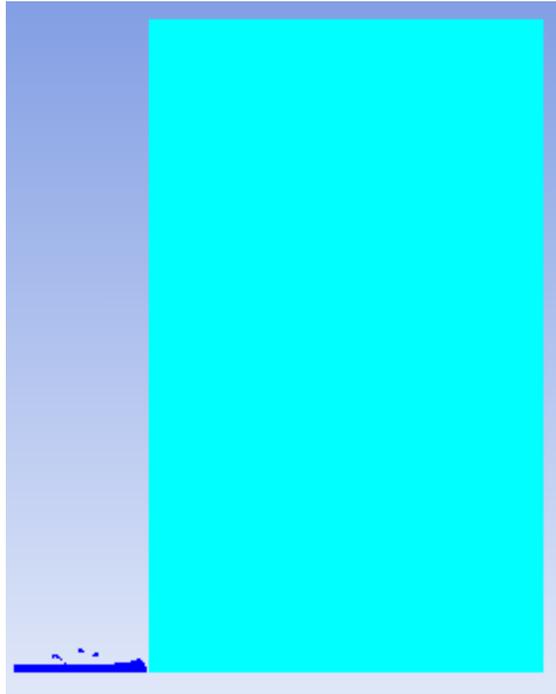
Figure 4.2: Deformed projectile- second SIFCON wall before strike

The only disadvantage of using 2D and axisymmetry was: although in the experiments there existed reinforcement bars in 2 percent SFRC and reinforced concrete targets, these bars were not allowed to be modeled in a 2D axisymmetric model. Hence, analyses were made for plain concrete and by changing failure conditions, for SIFCON and 2 percent SFRC without reinforcement bars. In order to see effects of failure parameters changes on accuracy of results, several simulations were conducted. Results of these analyses are given in Chapter 5. In this chapter, in order to make the reader understand the general working scheme of the AUTODYN, summary of the explicit time integration technique are given. After this explanation, descriptions of how the meshing is formed, the strength models, the EOS (equation of state), the failure and erosion criteria that were used for computation of the analyses are provided.

4.2   Explicit Time Integration Technique

In the analyses of the dissertations explicit time integration technique with the Lagrangian Computational Method was used to solve dynamic problems. The explanation below for the explicit integration technique is a summary of information given by Zukas, (2004).

The outline seen in Figure 4.3 below is referred to as central difference method and is used in many production wave propagation codes. Difference of implicit and explicit integration lays in the second step of it. In the explicit time integration what is necessary to calculate the next step which is the left side of the equilibrium can be gained easily since the right part of the equilibrium is already at hand. Having determined velocities and displacements in the second step, strain rates, stress, strains, pressures and nodal forces can be obtained. To repeat the caveat of Section 1.4 strain rate effects were not considered in this work.
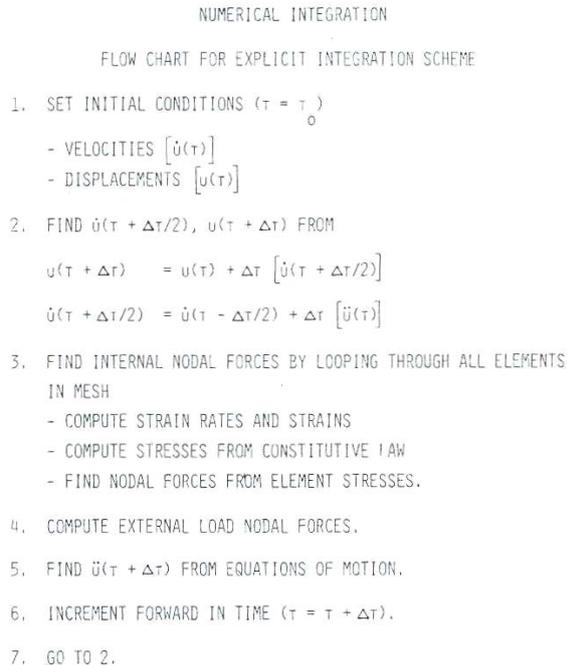
Figure 4.3: Implementation of the Central Difference Scheme [Zukas J.A., (2004)]

The calculations of the displacement and the velocity are straightforward but this technique has the disadvantage that is being only conditionally stable where the time step Δt is determined as:

$$\Delta t = \frac{k^* * l^*}{c} \qquad (4.1)$$

k= stability fraction (on the order of 0.6-0.9)

l^* = smallest mesh dimension

c= soundspeed

Implicit integration on the other hand, is unconditionally stable and allows larger time step in the calculations however, it is more complex. In Figure 4.4, Newmark β method, a widely used implicit scheme, is given

NUMERICAL INTEGRATION

IMPLICIT: DISPLACEMENTS AT $t + \Delta t$ CANNOT BE FOUND WITHOUT KNOWLEDGE OF ACCELRATIONS AT THE SAME TIME.

NEWMARK-β METHOD:

$$\dot{u}(t + \Delta t) = \dot{u}(t) + \Delta t \left[(1-\gamma)\ddot{u}(t) + \gamma\ddot{u}(t + \Delta t) \right]$$

$$u(t + \Delta t) = u(t) + \Delta t \dot{u}(t) + \Delta t^2 \left[(\tfrac{1}{2}-\beta)\ddot{u}(t) + \ddot{u}(t + \Delta t) \right]$$

PROCEDURE:

COMBINE ABOVE WITH EQUATIONS OF MOTION.

OBTAIN A SET OF SIMULTANEOUS EQUATIONS IN $u(t + \Delta t)$.

SOLVE IF LINEAR.

IF NONLINEAR, LINEARIZE IN SOME FASHION, THEN SOLVE SYSTEM OF EQUATIONS FOR $u(t + \Delta t)$.

Figure 4.4: Implementation of the Newmark β Method [Zukas J.A., (2004)]

If attention is paid to this scheme, it can be seen that in order to obtain velocity and displacement unknowns of the next time step ($t + \Delta t$), another unknown of advanced time acceleration must be used on the right side of the equilibrium. Hence, instead of solving equations easily as in the explicit integration, a number of simultaneous and mostly nonlinear equations must be solved here, after being linearized. Advantages of larger time step and unconditional stability are achieved in this manner.

Preference of the explicit integration for the problem of a hypervelocity projectile striking a plate lays in the total occurrence of the problem for a real physical environment being in the range of microseconds. This is also the appropriate time step for explicit integration to keep the scheme stable and failure is caused with just a few reverberations of wave instead of cumulative action for the multiple wave reverberations.

4.3   Meshing

In order to make simulations in 2D or in 3D, a real life continuous form had to be modeled by using discrete elements of simple geometry such as triangle, rectangle, cube etc is called meshing.

Both projectile and target were meshed by the help of meshing tool that was implemented in ANSYS AUTODYN software. Details for both target and projectile part are given in the following sections.

4.3.1   Projectile Meshing

Geometry of the projectile was drawn and meshed as half of the experimental one in AUTODYN.

Using the mirror in y plane option, full view of the half projectile could be obtained. Figure 4.5 shows meshed view of the projectile, while length of it is parallel to x axis and y axis being perpendicular to it.
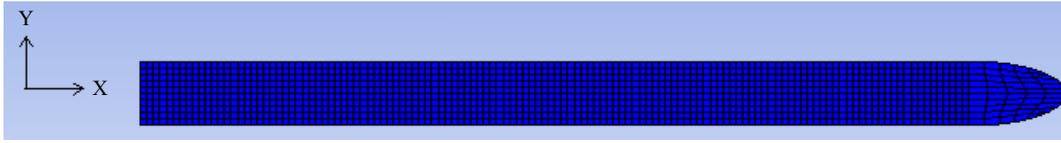
Figure 4.5: Full view of the projectile mesh by the help of mirror in y-plane option

Total length and radius of the projectile drawn were 372 mm, 13 mm respectively and dimension of projectile head in x direction was 39 mm. These represent the geometry similar to the one used by the Turkish Armed Forces. Projectile body was meshed with 2.6 mm both in x any y direction, while projectile head was configured as the implementation of the quarter circle in front of the projectile body and scaling it in the x direction to reach the actual simulation geometry.

4.3.2 Target Meshing

In the target meshing also, advantage of the axisymmetry was used. Since both target and projectile were symmetric in the y plane, the number of the element used in the calculation decreased into the half due to modeling only the half of the y dimension. Hence target dimensions became 400 mm in the x, 1000 mm in the y axes for two targets and 600 mm in the x, 1000 mm in the y axes for the remainder.

Size of the meshing is a very important issue especially in the target part, since failure of the concrete is the main consideration. In order to reach the convergence of the results, several mesh sizes were tried in the analyses. Mesh dependence of the solution can be seen clearly in the following section.

4.3.2.1   Mesh Dependence

General logic of the finite element analysis from mesh size point of view is that; as mesh size decreases, accuracy increases. But decrease in mesh size results in much longer time of simulation which is neither preferable nor efficient. In order to reach the adequate results from finite element analysis, variation of the solution according to the mesh size and for what size of meshing, convergence would occur with a meaningful computation time must be investigated. In this study, four different runs of simulations on a specific problem were conducted. All values of the parameters, including mesh sizes of the projectiles were the same in all four shots, except for concrete target mesh size. Concrete mesh size varied as 10 mm, 5 mm, 3 mm and 2 mm. From coarser to denser size, results of the solution can be seen in Figure 4.6-4.9. The color scale on the left of Figure 4.6 is omitted in similar figures in the sequel.
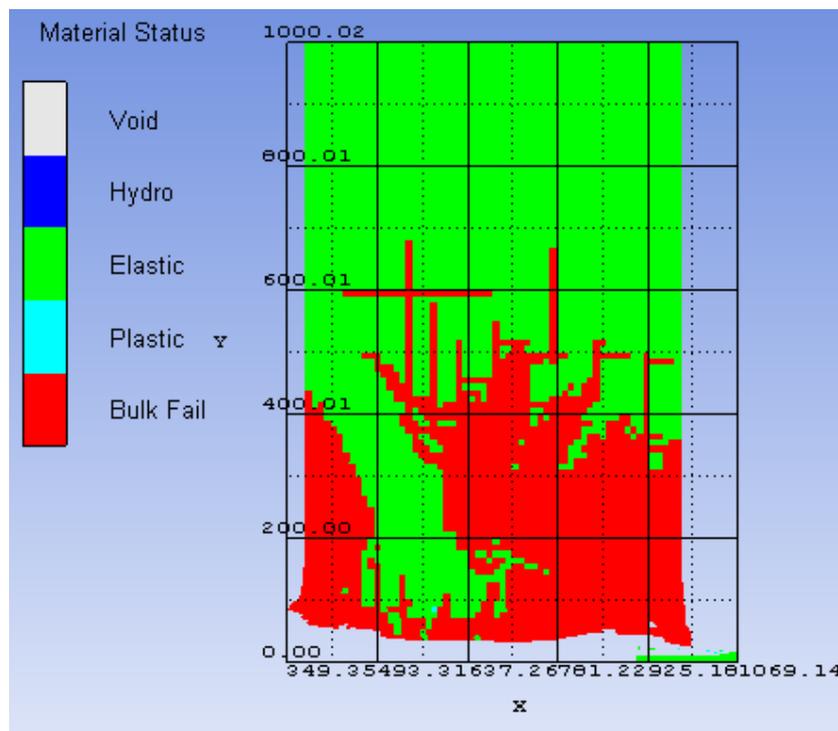
Figure 4.6: Result of projectile Impact on concrete target-10 mm mesh size
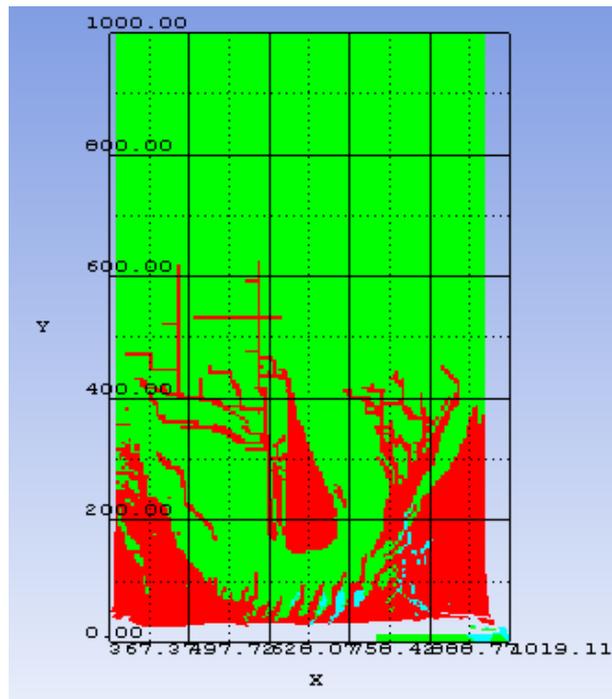
Figure 4.7: Result of projectile Impact at concrete target-5 mm mesh size
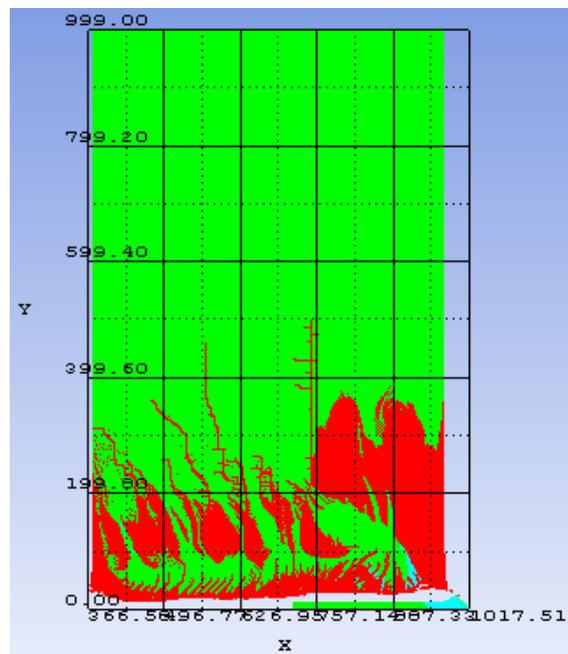
Figure 4.8: Result of projectile Impact at concrete target-3 mm mesh size
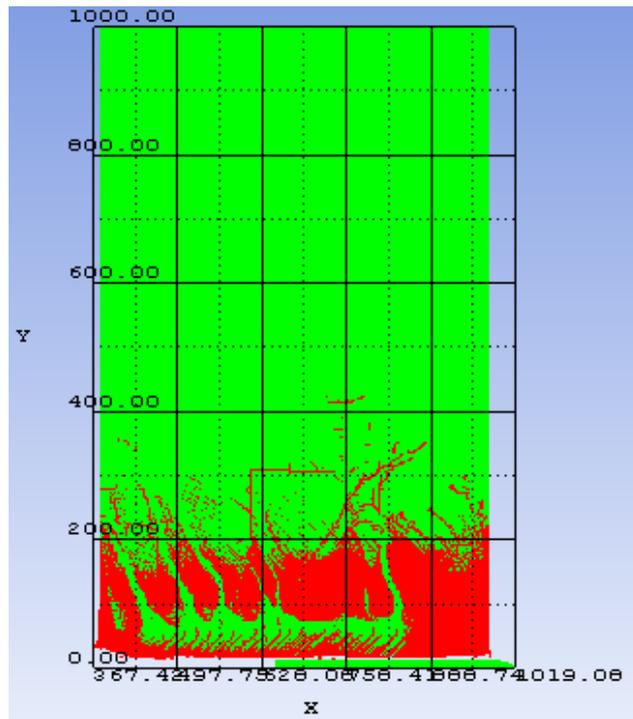
Figure 4.9: Result of projectile Impact at concrete target-2 mm mesh size

As can be viewed, when mesh size became smaller, accuracy became higher and crack pattern could be detected better, but it has to be kept in mind that, at some point, time required for solution becomes enormous and there existed no further efficiency in it. For this reason and being able to see the occurrence of convergence in 3 mm mesh size, this was chosen as mesh dimension throughout the study.

Another point that has to be mentioned is the effect of mesh size on the fracture energy calculations made for SIFCON and steel fiber reinforced concrete (SFRC) which are expressed in Section 4.5.2 in a detailed way. In order to calculate the SFRC and SIFCON fracture energy, plain concrete fracture energy has to be calculated firstly. In Nyström, (2008), fracture energy of the plain concrete ($G_{F.NSC}$) was said to be calculated in AUTODYN as:

$$G_{F.NSC} = \frac{f_t * \varepsilon_u * l_{el}}{2} \qquad (4.2)$$

$G_{F.NSC}$ = fracture energy for normal concrete.

f_t = tensile strength of the concrete

ε_u = crack strain (set to 0.01)

l_{el} = crack extensional length

This can be viewed schematically as:
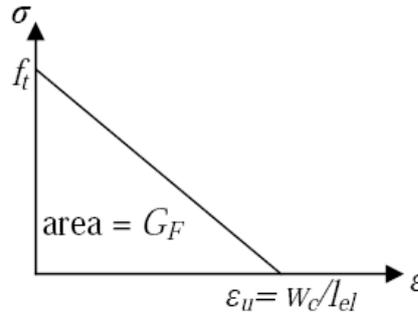
Figure 4.10: Linear crack softening relation used in AUTODYN

[Nyström, (2008)]

In the same reference, for the relationship between l_{el} and mesh size in AUTODYN 3D, l_{el} was said to be the diameter of the sphere which had the same volume as the three-dimensional mesh element. This relationship can be shown as:

$$l^{*3} = \frac{4}{3} * \pi * \left(\frac{l_{el}}{2}\right)^3 \qquad (4.3)$$

$$l^* = 0.806 * l_{el} \qquad (4.4)$$

l^* = side length of the meshed used

As can be seen, fracture energy value is mesh dependent and as mesh size increases value of fracture energy becomes larger.

4.4 Strength Models Used in the Computations

In the analyses of the dissertation, Drucker-Prager strength model was used to represent concrete material strength behavior while in order to demonstrate Tung.Alloy material strength behavior, Johnson-Cook strength model was used. Information about both of these strength models is given in the subsequent sections.

4.4.1 Drucker-Prager Model

The von Mises yield criterion was extended by Drucker and Prager, (1952), to include the effect of hydrostatic pressure on shearing resistance of the material. In Drucker-Prager model, the yield surface has a circular cross section on deviatoric planes. In order to give the theoretical background of the Drucker-Prager model, information gained from Chen, (1982) is summarized in this section.

The yield criterion then took the simple form, α^* and k^{**} being positive material constants.

$$f = \sqrt{J_2} + \alpha^* * I_1 = k^{**} \tag{4.5}$$

$$I_1 = \sigma_1 + \sigma_2 + \sigma_3 \tag{4.6}$$

$$J_2 = \frac{1}{6} * \left[\left(\sigma_x - \sigma_y \right)^2 + \left(\sigma_2 - \sigma_3 \right)^2 + \left(\sigma_3 - \sigma_1 \right)^2 \right] + \tau_{xy}^2 + \tau_{yz}^2 + \tau_{zx}^2 \tag{4.7}$$

The above equation can also be considered as a proper generalization of the Mohr-Coulomb criterion with a smooth surface in stress place. Stress-strain

88

relationship for this function is which shows plastic deformation must be accompanied by an increase in volume if $\alpha \neq 0$ which is also known as dilatancy:

$$d\varepsilon_{ij} = \frac{ds_{ij}}{2*G} + \frac{dI_1}{9*K}*\delta_{ij} + d\lambda*(\frac{s_{ij}}{2*\sqrt{J_2}} + \alpha^{**}*\delta_{ij} \tag{4.8}$$

$$d\lambda = \frac{\left(G/\sqrt{J_2}\right)*s_{mn}*de_{mn} + 3*K*\alpha^{**}*d\varepsilon_{kk}}{G + 9*K*\alpha^2} \tag{4.9}$$

$$d\varepsilon_{kk}^p = 3*\alpha^{**}*d\lambda \tag{4.10}$$

s_{ij} = deviatoric stress tensor.

ε_{ij} = strain in ij direction.

I_1 = mean normal strain.

δ_{ij} = Kronecker delta.

J_2 = octahedral shearing strain.

$s_{mn}*de_{mn}$ = rate of work due to distortion.

α^{**} = dilatancy factor.

G = shear modulus.

K = bulk modulus.

For the issue of Drucker-Prager material with a cap displaying isotropic hardening and softening, as a consequence of the normality plane, considerable dilatancy effect are introduced by the associated flow rule for Drucker-Prager model. The inelastic volumetric response can be controlled by a volume-dependent cap surface under hydrostatic compression. The introduction of a spherical end cap to the Drucker-Prager was made by Drucker et al., (1975).
The simple plane-cap model is described below:

Simple plane-cap model: Loading function for this model consists of tension-cutoff limits and hydrostatic hardening function in addition to usual

Drucker-Prager type of failure function, in this model, hardening function under hydrostatic loading is improved. This model's loading function consists of three surfaces:

- Drucker-Prager type of yield surface for loading and failure:

$$F_l = \alpha * I_1 + \sqrt{J_2} - k * (\varepsilon_p)$$ (4.11)

ε_p = effective plastic strain.

- A compression plane-cap surface

$$F_c = I_1 - x * (\varepsilon_{kk}^p) = 0$$ (4.12)

x= hardening function

ε_{kk}^p = plastic volumetric strain

- A tension-cutoff limit plane

$$F_t = I_1 - T = 0$$ (4.13)

T= tension-cutoff limit.

Scheme of this plane-cap model can be seen in Figure 4.11.
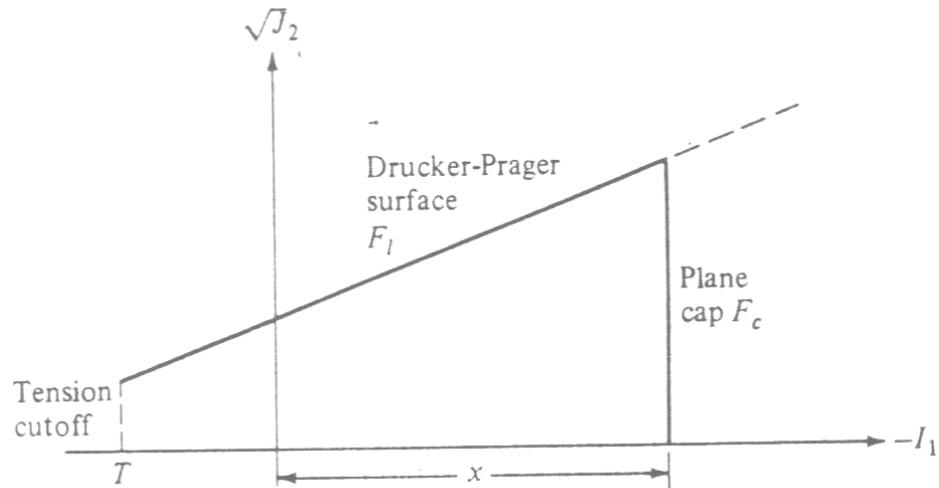
Figure 4.11: Drucker-Prager simple plane cap model [Chen, 1982]

The summary below is the Mohr-Coulomb Model of AUTODYN (2007), which explains where the use of Drucker-Prager model is appropriate. Drucker-Prager model is used in AUTODYN to represent the behavior of dry soils, rocks, concrete and ceramics where the cohesion and compaction behavior of the materials result in an increasing resistance to shear up to a limiting value of yield strength as the loading increases. In the analyses, Piecewise Drucker-Prager model function is used. This model consists of up to 10 pressure-yield stress points to define material strength curve. In tension (negative values of p), such materials have little tensile strength and this is modeled by dropping the curve for Y(p) rapidly to zero as p goes negative in order to give a realistic value for the limiting tensile strength. Scheme of the piecewise Drucker-Prager function can be seen below Figure 4.12.

Piecewise

Yield stress Y varies with pressure as a piecewise linear
function. Constant shear modulus G
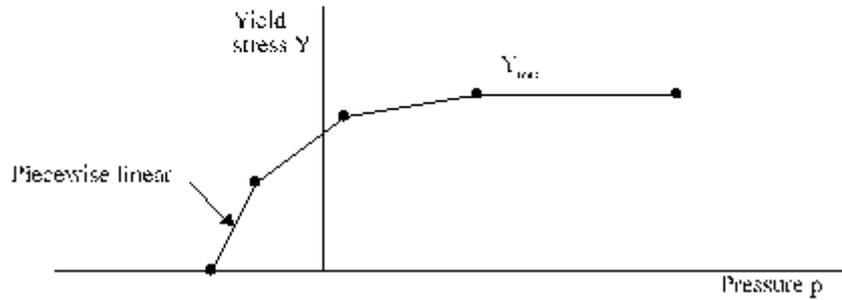
Figure 4.12: Piecewise yield stress versus pressure model used in AUTODYN
[AUTODYN, (2007)]

Values used for Drucker-Prager Strength Model which was implemented
in Concrete-L material model that existed in the library of AUTODYN and
conversion of 48 MPa Drucker- Prager concrete strength data that took place in
the paper of Tham, (2005), are shown in tabular form Table 4.1 and Table 4.2 and
as yield stress versus pressure in Figure 4.13 and Figure 4.14.

Table 4.1: Concrete-L Drucker-Prager strength data [AUTODYN, (2007)]

Concrete-L material model Drucker-Prager strength data	
Shear modulus (kPa)	7.88e+6
Pressure hardening type	Piecewise
Pressure #1 (kPa)	0.000000
Pressure #2 (kPa)	8.00e+4
Pressure #3 (kPa)	1.10e+5
Pressure #4 (kPa)	2.00e+5
Yield stress #1 (kPa)	2.50e+4
Yield stress #2 (kPa)	1.10e+5
Yield stress #3 (kPa)	1.60e+5
Yield stress #4 (kPa)	1.95e+5
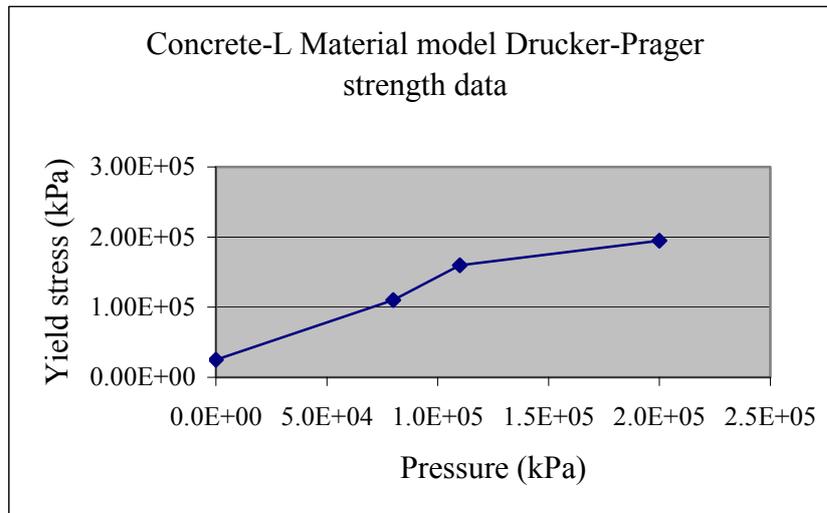
Figure 4.13: Concrete-L Drucker-Prager strength data in terms of yield stress versus pressure, [AUTODYN, (2007)]

Table 4.2: Concrete 48 MPa material model Drucker-Prager strength data, [Tham, (2005)]

Concrete 48 MPa material model Drucker-Prager strength data	
Shear modulus (kPa)	7.88e+6
Pressure hardening type	Piecewise
Pressure #1 (kPa)	-4.000e+3
Pressure #2 (kPa)	0.000
Pressure #3 (kPa)	1.600e+4
Pressure #4 (kPa)	1.545e+5
Pressure #5 (kPa)	2.670e+5
Pressure #6 (kPa)	5.193e+5
Pressure #7 (kPa)	6.136e+5
Yield stress #1 (kPa)	0.000
Yield stress #2 (kPa)	9.600e+3
Yield stress #3 (kPa)	4.800e+4
Yield stress #4 (kPa)	1.600e+5
Yield stress #4 (kPa)	2.190e+5
Yield stress #4 (kPa)	3.194e+5
Yield Stress #4 (kPa)	3.194e+5
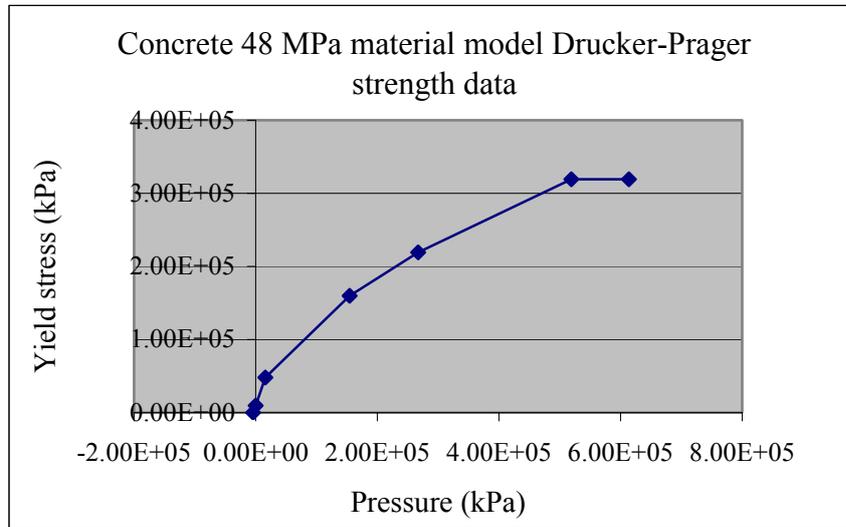
Figure 4.14: Concrete 48 MPa material model Drucker-Prager strength data in terms of yield stress versus pressure, [Tham, (2005)]

4.4.2 Johnson-Cook Model

Vedantam et al., (2006) state that dynamic events often involve high strain rate and to predict the response of a material accurately, high strain rate effects on the flow stress must be included in the constitutive models. Johnson-Cook model of AUTODYN, (2007) provided much of the information in this section. This model was implemented in AUTODYN to represent the strength behavior of the materials subjected to large strains, high strain rates and high temperatures that might occur in problems of intense impulsive loading due to high velocity impact loading.

In Johnson-Cook model, the yield stress (and the radius of the von Mises cylinder) varies depending on strain, strain rate and temperature. Yield stress is defined as:

$$Y = [A + B * \varepsilon_p^n] * [1 + C * \ln \varepsilon_p^*] * [1 - T_H^m] \qquad (4.14)$$

ε_p =effective plastic strain

ε_p^* =normalized effective plastic strain rate

$$\frac{T - T_{room}}{T_{melt} - T_{room}} \qquad (4.15)$$

T_H = homologous temperature = $\dfrac{T - T_{room}}{T_{melt} - T_{room}}$

A= basic yield stress at low strains

B and n= represents effect of strain hardening.

The expression in the first set of brackets gives the stress as a function of strain when ε_p^* = 1.0sec^{-1} and T_H= 0 (i.e. for laboratory experiments at room temperature).

The second and third sets of brackets represent the effects of strain rate and temperature, respectively. The latter relationship models the thermal softening so that the yield stress drops to zero at the melting temperature T_{melt}

The constants in these expressions (A,B,C,n,m, T_{melt}) were obtained by Johnson and Cook empirically by means of dynamic Hopkinson bar tensile tests over a range of temperatures with other tests and checked by calculations of Taylor tests of impacting metal cylinders on rigid metal targets which provided strain rates in excess of 10^5 sec^{-1} and strains in excess of 2.0. The plastic flow algorithm for this model has an option of rate correction to reduce high frequency oscillations that are sometimes observed in the yield surface under high strain rates.

Values of Johnson-Cook strength data for Tung.Alloy material model originally placed in the library of the software is shown in Table 4.3

Table 4.3: Tung.Alloy material model Johnson-Cook strength data, [AUTODYN, (2007)]

Johnson-Cook strength data	
Shear modulus (kPa)	1.600e+8
Yield stress (kPa)	1.506e+6
Hardening constant (kPa)	1.770e+5
Hardening exponent	0.120
Strain rate constant	0.016
Thermal softening exponent	1.000
Melting temperature (K)	1.723e+3
Ref. strain rate (/s)	1.000
Strain rate correction	1st order

4.5   Equation of State (EOS)

In the material models part of AUTODYN, (2007), a simple definition is given to state that the EOS is used to represent the material's hydrostatic response which is the general behavior of gases and liquids that can sustain no shear. Response of gases and liquids to dynamic loading is strictly hydrodynamic, with pressure varying as a function of density and internal energy. Similarly, this is also the primary behavior of solids at high deformation rates when hydrostatic pressure is far beyond the material's yield stress.

Zukas, (2004), defines EOS according to a shock physicist as an attempt to connect the theoretical predictions of microstructural models of atomic lattices with experimental observations of the microscopic behavior of models. In the same reference it is added that, since there is no general theory to connect atomic considerations to continuum behavior, although interatomic forces in solids result in shear stresses and these shear stresses produce triaxial stress during uniaxial deformation, simplifications will be made and deviatoric (distortional) part will be ignored and condition becomes equal to an equilibrium stress tensor which is spherical and represented by the pressure $P = -\sigma$. Dilatational (state of stress

96

result in volume change without distortion) and deviatoric components of stress tensor is shown below taken from Ugural and Fenster, (2003).

Where $\sigma_m = \dfrac{\sigma_x + \sigma_y + \sigma_z}{3}$

Dilatational stress tensor $= \begin{bmatrix} \sigma_m & 0 & 0 \\ 0 & \sigma_m & 0 \\ 0 & 0 & \sigma_m \end{bmatrix}$

Deviatoric stress tensor $= \begin{bmatrix} \sigma_x - \sigma_m & \tau_{xy} & \tau_{xz} \\ \tau_{xy} & \sigma_y - \sigma_m & \tau_{yz} \\ \tau_{xz} & \tau_{yz} & \sigma_z - \sigma_m \end{bmatrix}$

In Zukas, (2004), it is also implied that, EOS used in the codes are calibrated through plate impact experiments. Because of the laboratory restrictions, upper limit for pressures are said to be around 6 Mbars for metals and curve fitting is applied through the experimental data, so extrapolations from the very extreme data (12-20Mbars) would produce nonsensical results.

In order to see material response of solids under impact loading, EOS must be used. Type of EOS may differ among different materials. For the analyses, Shock EOS was used for tungsten-alloy projectile and Porous EOS (Piecewise-Linear Porous Model) was used for the target.

4.5.1 Shock EOS

Definition of the Shock EOS takes its root from combination of Rankine Hugoniot Equations, shock wave propagation velocity-particle speed relationship and Gruneisen Theory assumption as mentioned in Hiermaier, (2008).

$e_1 - e_0 = \dfrac{1}{2} * (p_1^* + p_0) * (\dfrac{1}{\rho_0} - \dfrac{1}{\rho_1^*})$ is a specific curve representing all

possible peak conditions achieved when a shock wave arises. This curve is called

Hugoniot Curve which is not an equation of state. Adding one more relationship of the shock wave and shock velocity to Rankine Hugoniot Equations related with mass conservation, momentum balance and energy conservation, can be utilized to identify EOS. [Hiermaier, (2008)]

By the help of the relationship of shock velocity and velocity behind shock wave is shown in the equation below, Rankine Hugoniot Equations can be solved:

$$v_S = c_0 + S * v_1 \tag{4.16}$$

In the Shock Equation of State part in AUTODYN, (2007), Mie-Gruneisen form of equation of state based on the shock Hugoniot which can be seen in Equation 4.28 is mentioned to have been established.

$$p = p_H + \Gamma * \rho_0 * (e - e_H) \tag{4.17}$$

$$p_H = \frac{\rho_0 * c_0^2 * \mu * (1 + \mu)}{\left[1 - (s - 1) * \mu\right]^2} \tag{4.18}$$

$$e_H = \frac{1}{2} * \frac{p_H}{\rho_0} * \left(\frac{\mu}{1 + \mu}\right) \tag{4.19}$$

$\rho_0, \rho_1 =$ density of the state ahead and behind the shock

$e_0, e_1 =$ internal energy of the state ahead and behind the shock

$p_0, p_1^* =$ pressure of the state ahead and behind the shock

$v_0, v_1 =$ particle velocity of the state ahead and behind the shock

$$\eta = \frac{\rho_1}{\rho_0} \tag{4.20}$$

$$\mu = \frac{\rho_1}{\rho_0} - 1 \tag{4.21}$$

$S, s =$ slope of the equation

$c_0 =$ soundspeed in the surrounding un-shocked medium

$\Gamma =$ Gruneisen Gama coefficient

$v_s =$ shock wave speed

In the Shock Equation of State part of AUTODYN (2007) it is explained that, relationship of shock velocity and particle velocity does not hold linear for too large a compression. To overcome this nonlinearity, in AUTODYN, the input makes the definition of two linear fits valid to the shock velocity - particle velocity relationship; one holding at low shock compressions defined by v > VB and one at high shock compressions defined by v < VE, region between VE and VB is covered by a smooth interpolation between the two linear relationships. This exposition can be seen in Figure 4.15 below.
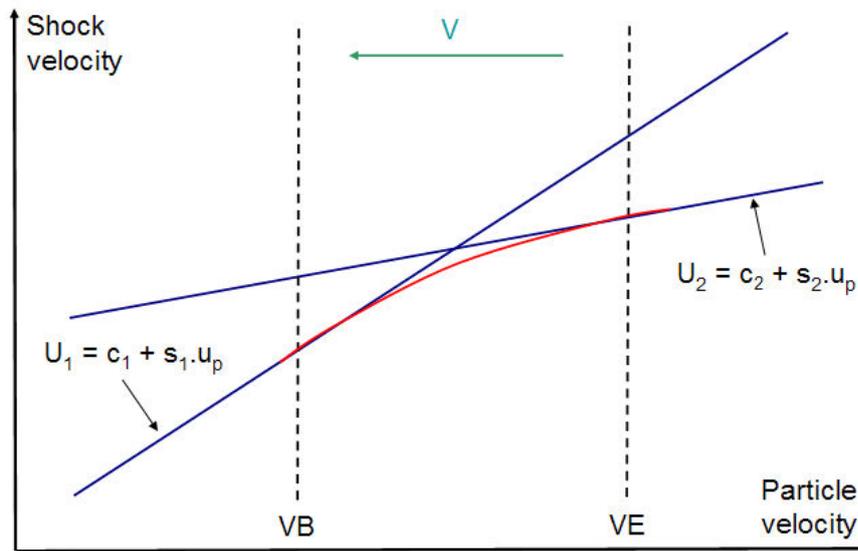
Figure 4.15: The Shock EOS model, [AUTODYN (2007)]

$$U_1 = c_1 + s_1 * u_p \qquad (4.22)$$

$$U_2 = c_2 + s_2 * u_p \qquad (4.23)$$

$$U = U_1 + \frac{(U_2 - U_1) * (v - VB)}{(VE - VB)} \quad \text{for} \quad VE < v < VB \qquad (4.24)$$

The shock equation of state also allows one optionally to include a quadratic shock velocity, particle velocity relation of the form:

99

$$U = C_0 + S_1 * u_p + S_2 * u_p^2 \qquad\qquad (4.25)$$

$U, U_1, U_2 = $ shock wave speed

$S_1, S_2 = $ slope of the equations

Shock EOS parameters in AUTODYN are: $c_1, c_2, s_1 = S_1, s_2$, parameter quadratic S_2 VE/V0, VB/V0, Γ_0 and ρ_0

In the simultations of the models here, TUNG.ALLOY Model which was implemented in ANSYS AUTODYN Library originally was used. Shock EOS values for this model is shown in Table 4.4.

Table 4.4: Tung.Alloy material model Shock EOS data [AUTODYN, (2007)].

Tung.Alloy material model Shock EOS data	
Gruneisen coefficient	1.540
Parameter C1 (mm/s)	4.029e+06
Parameter S1	1.237
Parameter Quadratic S2 (s/mm)	0.000
Relative volume, VE/V0	0.000
Relative volume, VB/V0	0.000
Parameter C2 (mm/s)	0.000
Parameter S2	0.000
Reference Tempreture (K)	300.000
Specific Heat (uJ/kgK)	1.340e+08
Thermal Conductivity (mJ/mKs)	0.000

4.5.2 Porous EOS

It is implied in Tham, (2006) paper that pressure versus volumetric relation of the concrete showing its compressibility, can be modeled using Porous EOS. Porous EOS in AUTODYN consists of five density-pressure points, adding to porous and solid soundspeed inputs. In the same reference it is also implied that the compaction path, which models the collapse and plastic flow of void and cells of the concrete from its porous state to its fully compressed state, begins with an elastic path, followed by a plastic path and extend to a fully compacted path where unloading and reloading at any point along the paths are based on its sound speed.

Piecewise-Linear Porous Model information from AUTODYN (2007) is used to give brief information below for this section. Porous model which has a compaction curve of piecewise linear function can be combined together with any strength model to simulate yielding due to shear deformations. The use of a fixed compaction path is equivalent to using a Mie-Gruneisen equation of state that can be seen in Equation 4.28 with an assumed value of zero for the Gruneisen Gamma and this ignores the pressure enhancement due to the energy absorption which is very significant for porous solids. Hence, in order to get reasonable results from this EOS, either energy increase per second or Gruneisen Gamma of the specimen must be small. Since Gruneisen Gamma for concrete is between 0.1 and 0.3, provided that maximum stress level is not very large, reasonable results can be gained. A schematic Porous EOS curve is given in Figure 4.16.
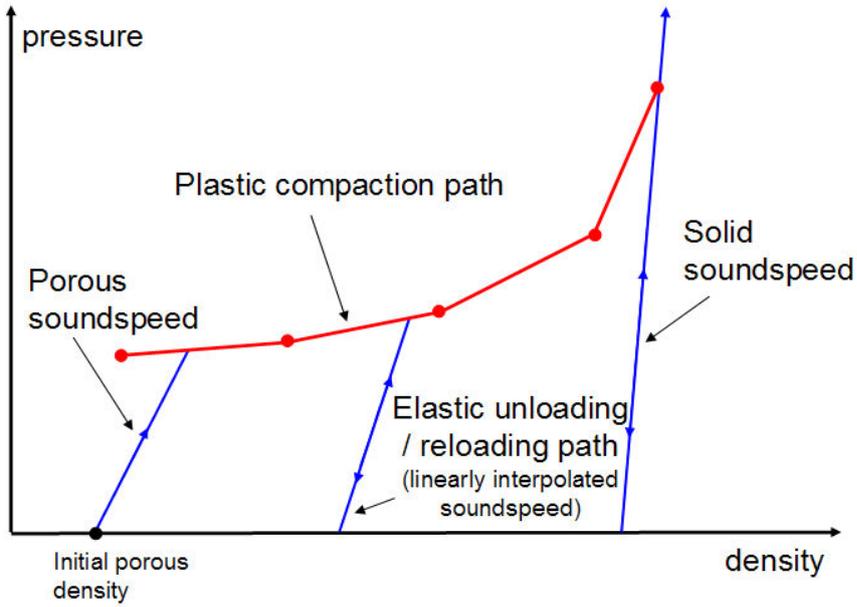
Figure 4.16: The Piecewise-Linear Porous EOS Model, [AUTODYN, (2007)]

Material initially compacts from $\rho = \rho_0$ along an elastic path defined by the differential equation until the pressure reaches the plastic yield stress defined by the value of the pressure in the first pair.

$$\frac{dp}{d\rho} = c_{init}{}^2 \tag{4.26}$$

Subsequent loading takes place along the plastic compaction path until the material is fully compacted then; compression takes place according to the linear relationship:

$$p = c_s^2 * \left(\rho - \rho_{ref} \right) \tag{4.27}$$

As the material compacts, elastic unloading uses a bulk sound speed interpolated between c_{por} and c_s the path is always computed from the first differential equation.

$$c_{int} = c_{por} + \left(c_s - c_{por} \right) * \left[\frac{\alpha - \alpha_1}{1 - \alpha_1} \right]$$ (4.28)

The soundspeed output by AUTODYN represents the combined effects of the bulk soundspeed given above and that due to the presence of strength. Thus if strength is being used, the soundspeed will be:

$$c = c_{int} + \sqrt{\frac{4 * G}{3 * \rho}}$$ (4.29)

ρ_{ref} or ρ_s = reference or solid density (the density at zero pressure of the fully compacted solid)

c_{por} = bulk soundspeed of the porous material

c_s = bulk soundspeed of the solid, fully compacted material

ρ_1 to ρ_{10} and p_1 to p_{10} = up to ten density, pressure pairs defining a piecewise-linear plastic compaction path

ρ_0 = the initial density (defined when the element is filled)

c_{int} = interpolated bulk sound speed

$$\alpha = \rho_{ref} / \rho$$ (4.30)

$$\alpha_1 = \rho_{ref} / \rho_1$$ (4.31)

G = current shear modulus

In the analyses, Concrete-L material model data already existed in the AUTODYN library and concrete 48 MPa Drucker-Prager material model data found through the literature survey [Tham, (2005)] were used. Data of concrete EOS values are shown in Table 4.5 and Table 4.6 pressure versus density diagrams are shown in Figure 4.17 and Figure 4.18.

Table 4.5: Concrete-L material model Porous EOS data [AUTODYN, (2007)]

Concrete-L material model Porous EOS data	
Solid Soundspeed (mm/s)	2.20e+6
Porous Soundspeed (mm/s)	2.20e+6
Density #1(kg/mm^3)	2.34e-6
Density #2 (kg/mm^3)	2.35e-6
Density #3 (kg/mm^3)	2.40e-6
Density #4 (kg/mm^3)	2.46e-6
Density #5 (kg/mm^3)	2.50e-6
Pressure #1 (kPa)	0.000000
Pressure #2 (kPa)	2.50e+4
Pressure #3 (kPa)	7.00e+4
Pressure #4 (kPa)	1.30e+5
Pressure #5 (kPa)	2.50e+5
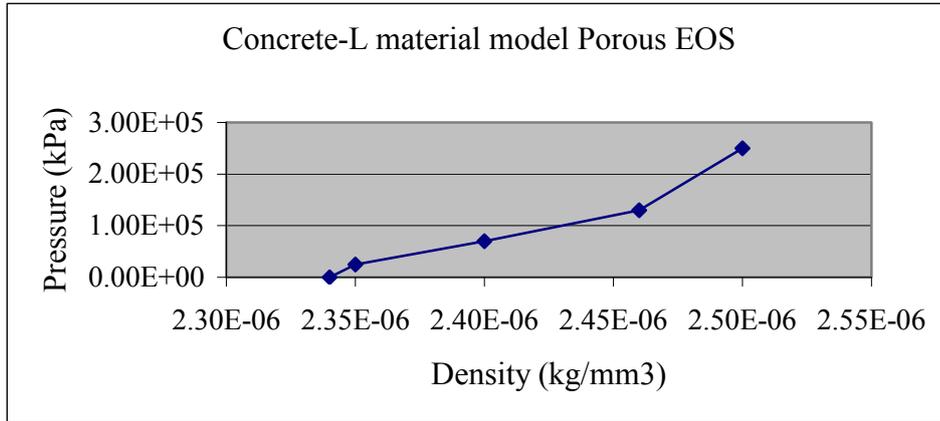
Figure 4.17: Concrete-L material model Porous EOS data in terms of pressure versus density [AUTODYN, (2007)]

Table 4.6: Concrete 48 MPa Drucker-Prager material model Porous EOS Data [Tham, (2005)]

Concrete 48MPa Drucker-Prager material model Porous EOS data	
Solid Soundspeed (mm/s)	3.794e+6
Porous Soundspeed (mm/s)	3.794e+6
Density #1 (kg/mm^3)	2.440e-6
Density #2 (kg/mm^3)	2.442e-6
Density #3 (kg/mm^3)	2.571e-6
Density #4 (kg/mm^3)	2.699e-6
Density #5 (kg/mm^3)	2.828e-6
Pressure #1 (kPa)	0.000000
Pressure #2 (kPa)	1.600e+4
Pressure #3 (kPa)	3.607e+5
Pressure #4 (kPa)	7.053e+5
Pressure #5 (kPa)	1.050e+6
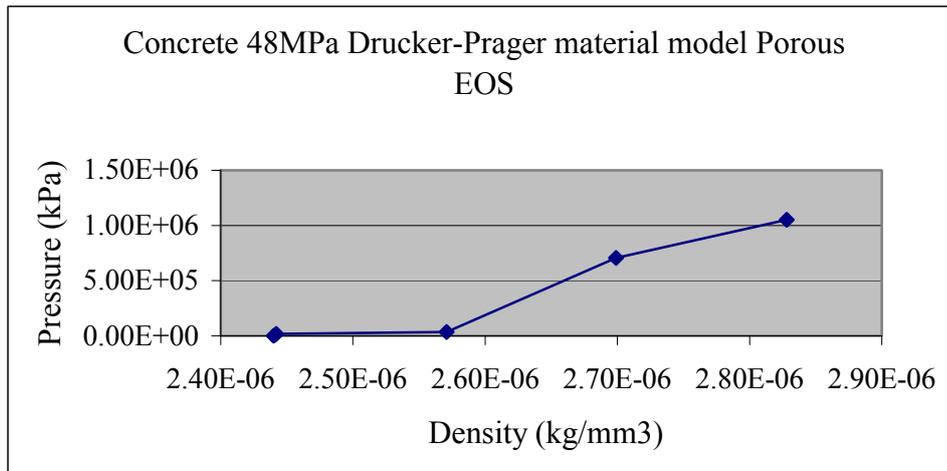
Figure 4.18: Concrete-L 48 MPa material model Porous EOS data in terms of pressure versus density, [Tham, (2005)]

4.6   Failure Model Used in the Computations

For the analyses, failure criterion was defined only for the target. Tung.Alloy type of material which was used to model projectile did not need failure criteria originally hence, only concrete failure occurred. Type of the failure model chosen for the concrete, SFRC and SIFCON was Hydrodynamic tensile failure model (Pmin) which is also the original failure model for Concrete-L material that exists in the library of AUTODYN.

4.6.1   Hydrodynamic Tensile Failure Model (PMIN)

This section is the summary of the information obtained from Bulk Isotropic Models part from AUTODYN (2007). In the reference, it is mentioned that Hydrodynamic tensile failure model is used to apply long periods of time with tensile wave is propagating around the system. It can be used to calculate spalling or cavitations around the system and avoids catastrophic failure and grossly unrealistic solutions occurring but since it is very simple, there can only be a rough approximation of the reality.

In this model, a constant hydrodynamic tensile limit (which must be chosen realistically) is set for the material. If the value of the hydrodynamic pressure in a cell falls below this limit, bulk failure is assumed to have occurred. When there is a bulk failure, the pressure is set to zero, the internal energy is recomputed and the material is assumed to have rehealed so that negative pressures may occur in the next time-step but limited again by the hydrodynamic tensile limit. In analyses reported here, reheal option was generally chosen as "no" to see the larger deformation and be on the safe side. This failure model has an advantage of crack softening which formed the basis of SIFCON and steel fiber reinforced concrete specimens' analyses. The scheme showing hydrodynamic tensile failure model is viewed in Figure 4.19 below.
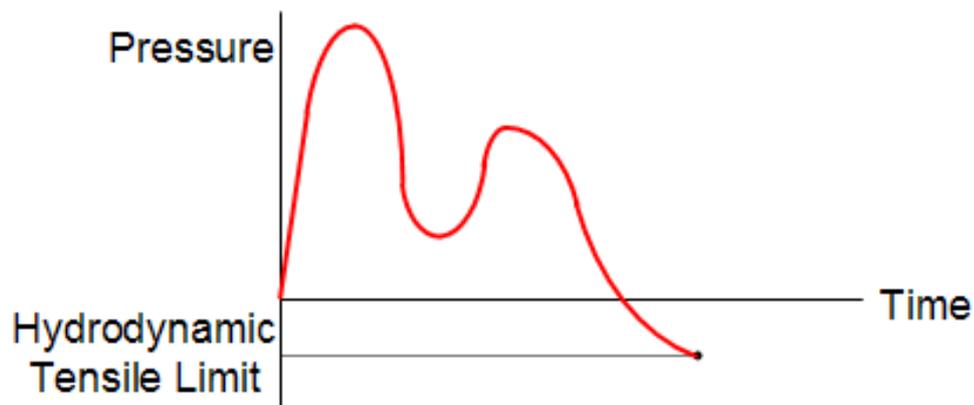
Figure 4.19: Hydrodynamic tensile failure model [AUTODYN, (2007)]

4.6.1.1 Tensile Limit

As mentioned, hydrostatic tensile limit is a parameter to be set carefully, as a matter of fact, it is the most important parameter which is responsible for the amount of failure and crater size. This result comes through several simulaton runs with varying tensile limits. Tensile limits used for different materials and how the value of tensile limits calculated for different materials are given below.

Analyses results for different tensile limits are compared with the experimental data in Chapter 5.

4.6.1.1.1 Plain Concrete Type A (30 MPa)

Concrete-L material model is originally existed in the AUTODYN library. In terms of this material model analyses, several tensile limits equal to or below ten percent of compressive strength of 30 MPa (3 MPa) were tried to see which one would give a closer result for the crater volume. Used values can be seen in Table 4.7 below.

Table 4.7: Tensile limit conditions used in plain concrete type A (30 MPa)

Tensile limit (kPa)	Reheal
-2.5	No
-2.75	No
-3	Yes
-3	No

4.6.1.1.2 Plain Concrete Type B (55 MPa)

Concrete 48 MPa Drucker-Prager material model data found in Tham, (2005), were used for simulations of this concrete. Like 30 MPa compressive strength plain concrete, several tensile limit values below 5.5 MPa were used to reach data closer to experimental results. Used values can be seen in Table 4.8.

Table 4.8: Tensile limit conditions used in plain concrete type B (55 MPa)

Tensile limit (kPa)	Reheal
-1	No
-1.25	No
-1.5	No
-1.75	No
-3	No
-4	No

4.6.1.1.3 2 percent Steel Fiber Reinforced Concrete (SFRC) (61 MPa)

Since experimental values of the specimen did not exist, closest material data found through literature survey which belong to the concrete 48 MPa Drucker-Prager material model were used for the simulation of SFRC however; tensile limit was calculated according to the Chanh (2005) paper.

In Figure 4.20, graph taken from his paper, shows the increase in the tensile strength for 33, 62 and 100 aspect ratios with different fiber contents by weight.
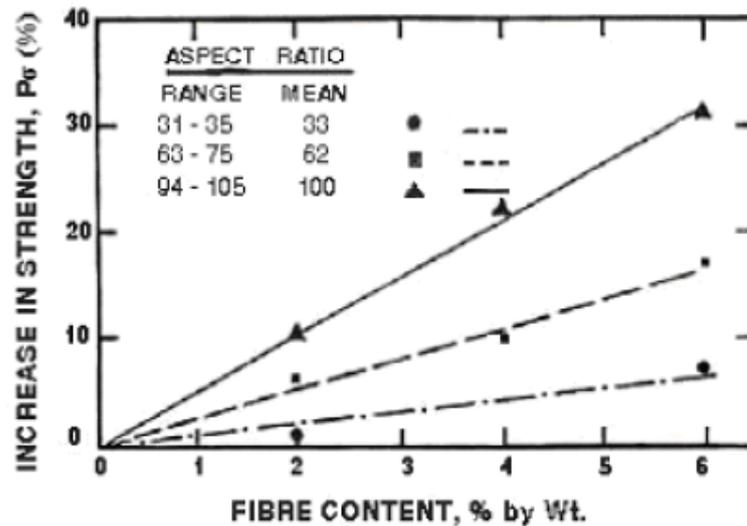
Figure 4.20: Increase in strength according to fiber content and aspect ratio
[Chanh, (2005)]

For the specimens tested in the experimental program, two percent steel fiber reinforcement by volume existed. Dramix RC -80/60- BN with 80 aspect ratio [Dramix RC-80/60-BN, (2005)] was the choice used of the fiber. Curve fitting and linearization were applied to Figure 4.20 in order to reach the 80 aspect ratio data and result of this work is shown in Figure 4.21. Fiber content was determined in terms of volumetric ratio in the experiments however, in the graph, it is calculated by weight hence, a conversion must be applied. In order to make

this conversion, assumptions of fiber density being around 8400 kg/m^3, while concrete density being 2400 kg/m^3 were made. By taking two percent volumetric ratio and related densities, steel fiber reinforcement was determined as 6.7 percent by weight.
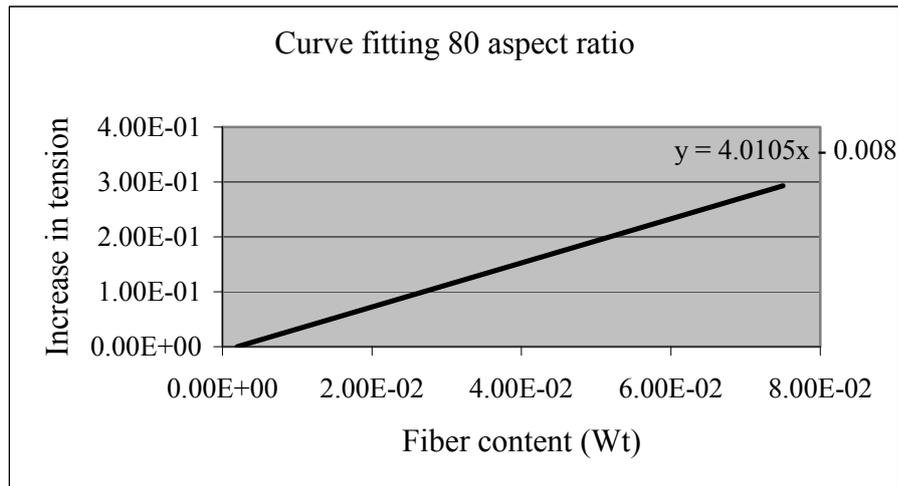
Figure 4.21:Increase in tension versus fiber content for 80 aspect ratio.

In Nyström and Gylltoft, (2008), compressive strength- tensile strength relationship is shown in Figure 4.22.
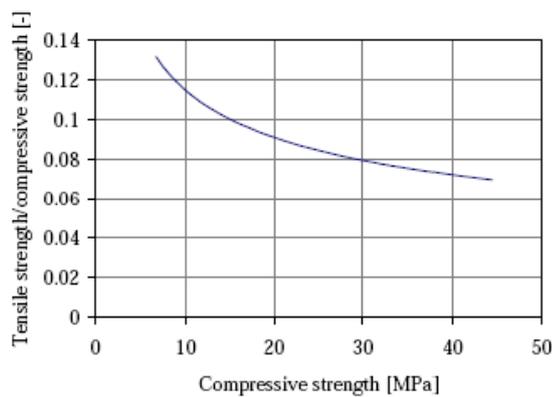
Figure 4.22: Tensile strength/compressive strength versus compressive strength [Nyström and Gylltoft, (2008)].

110

Here also a curve fitting was applied to obtain the value of tensile strength/compressive strength for the plain concrete which had 61 MPa compressive strength. Result of this application can be seen in Figure 4.23.
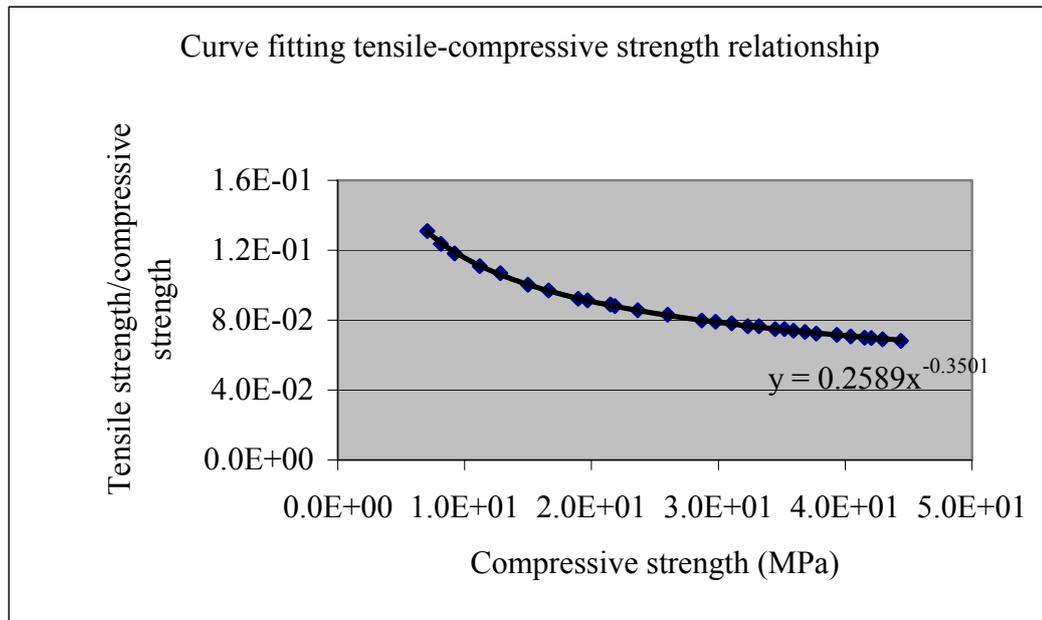
Figure 4.23: Curve fitting application to Figure 4.22

By the help of the curve fitting application in Figure 4.23, tensile strength of the plain concrete which had 61 MPa compressive strength was found to be 3.745 MPa. Percentage of tensile stress increase because of 80 aspect ratio fiber usage was applied to this values and tensile strength of the SFRC specimen was calculated as 4.75 MPa.

4.6.1.1.4 SIFCON (58 MPa)

Since there was no experimental value for SIFCON, here also concrete 48 MPa Drucker-Prager material model values found through literature survey from Tham, (2005), was used for strength model, however, tensile limit was set according to Marchand et al. (1998) paper where the major tensile strength in

SIFCON is mentioned to be approximately twice that expected for standard concrete (approximately 10-15 percent of the compressive strength). Two values were set to see maximum and minimum tensile limit conditions. Values are shown in Table 4.9.

Table 4.9: Tensile limit conditions for SIFCON

Tensile Limit (kPa)	Reheal
-5.8	No
-8.7	No

4.6.2 Crack Softening

Theoretical information used to construct this section is taken from Crack Softening part of AUTODYN, (2007). It is mentioned in AUTODYN (2007) that in principle or material stress/strain failure models, materials lose their strength instantaneously and later on, failed part can only undergo bulk compression. In reality, brittle materials do not fail instantaneously, and they gradually lose their load carrying capacity as cracks propagate through the material, thus, crack softening is implemented in failure models to solve this problem. The current maximum principal tensile stress in the cell is stored as variable Fail.Stres. A softening slope is defined using local cell size and material parameter. After failure takes place, a maximum principal tensile stress failure surface is determined to limit the maximum principal tensile stress in the cell and an associated flow surface is used to accumulate the crack strain. For input parameter of crack softening curve, fracture energy (G_f) is needed, where relationship between fracture toughness (K^*) and fracture energy is

$$K^* = \sqrt{E * G_f} \qquad (4.32)$$

112

Rankine plasticity is used to return trial elastic stresses to the failure surface. For this purpose there are: No Buckling, Buckling and Radial Return options. The Bulking type return algorithm would normally be used in quasi-static applications; however, in this option excessive amount of buckling occurs. Therefore, the default option of associative in π-space (No Buckling) was chosen for the analyses.

Crack softening function in the AUTODYN is linear and shown in Figure 4.24.
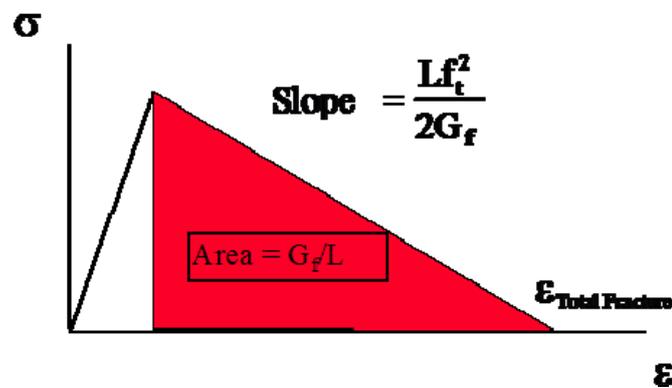
Figure 4.24: Crack softening in AUTODYN [AUTODYN, (2007)]

In the simulations, failure behavior diversities of the concrete, SFRC and SIFCON materials were expressed in material models as use of different tensile limit and different fracture energy values. Since fracture energy of plain concrete was very small compared to SFRC and SIFCON, crack softening option was not used for plain concrete analyses. However, this option played an important role for modeling steel fiber reinforced concrete and SIFCON. Procedures used to calculate fracture energy values of steel fiber reinforced concrete and SIFCON will be mentioned in the following sections.

4.6.2.1   2 percent Steel Fiber Reinforced Concrete (SFRC)

The method based on the work of Löfgren, (2005) which takes place in Nyström, (2008) was used here in order to calculate fracture energy for the steel fiber reinforced concrete. This method is a bi-linear stress-crack opening relation for steel fiber reinforced concrete (SFRC). The Scheme can be seen in Figure 4.25.
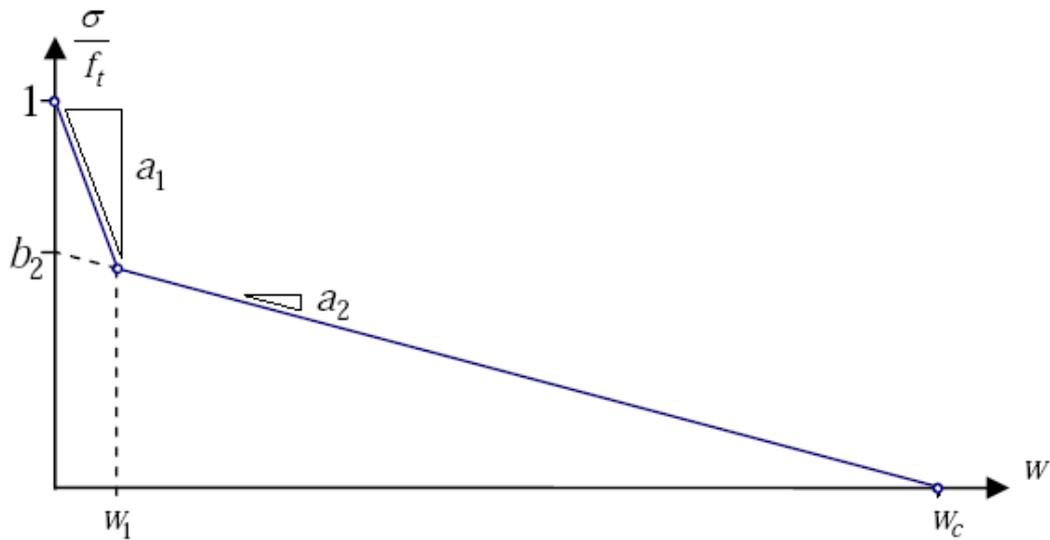
Figure 4.25: Bi-linear stress-crack opening relation for steel fiber reinforced concrete [Nyström, (2008)]

Rate of decrease in stress directly after tensile stress is described by parameter a_1; this parameter is mainly responsible for fracture properties of plain concrete. Parameter a_2 describes the rate of stress decrease related to fiber length. Critical crack opening w_c, is influenced by fiber fracture and whether there is good or poor bonding. w_c can be between $L_f/10$ and $L_f/2$. b_2 is related to dosage of the fiber and increases with the increase in fiber volume.[Nyström, (2008)]

Since during the calculations of b_2, Löfgren's related equations differed a bit from Gylltoft, (1983), Nyström, (2008) made the adjustment between those equations. As a result, b_2 and n_{fibres} are calculated as:

$$b_2 = \frac{1-0.4}{2.6727} * n_{fibres} + 0.4 \qquad (4.33)$$

$$V_f = \frac{n_{fibres}}{2.5396} \qquad (4.34)$$

Calculation of a_1 and a_2 are done in this manner:

$$a_1 = \frac{f_t}{G_{F.NSC}} \qquad (4.35)$$

$$a_2 = \frac{a_1}{200} \qquad (4.36)$$

f_t = tensile strength of the concrete

$G_{F.NSC}$ = fracture energy for normal concrete.

In Löfgren (2005), Dramix RC-65/35 was used and number of fibers per cm^2 calculations were done according to those specific experiments of the thesis. Although, Dramix RC-80/60 was the fiber choice for our SFRC target in the experiments, since we did not have the related tests of number of fibers per cm^2 for our experiments, it was be handled with the equation which takes place in Löfgren (2005).

As can be seen in order to calculate a_1, fracture energy of normal concrete has to be evaluated. Fracture energy calculation of the normal concrete has been given in Equation 4.2.

In our calculation tensile strength of two percent fiber reinforced concrete which had compressive strength of 61 was 4.75 MPa. After mesh dependence

studies, adequate mesh size were set to 3 mm thus, crack extension length was found as 3.72 mm. Using these values, fracture energy of the normal concrete with 4.75 MPa tensile strength turned out to be

$$G_{F.NSC} = 0.088 \frac{Nmm}{mm^2} = 88 \frac{J}{m^2} \tag{4.37}$$

$$a_1(1/mm) = 54 \tag{4.38}$$

$$a_2(1/mm) = 0.27 \tag{4.39}$$

When σ_t was scaled to 1, b_2 was:

$$b_2 = 0.4114 \tag{4.40}$$

In the Figure 4.26 which can be seen below, y axis is arranged as σ_t and x axis arranged as crack opening, w (mm).
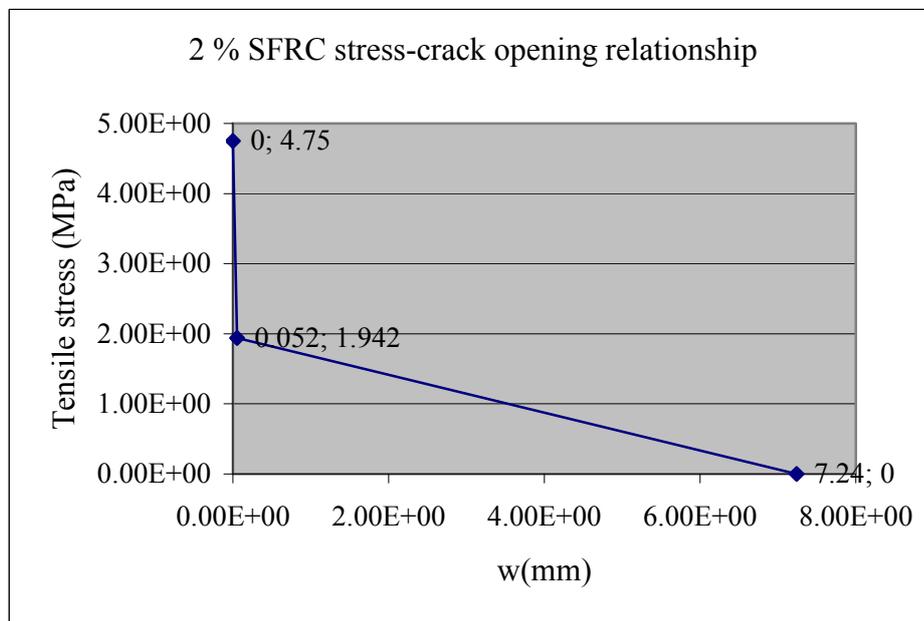
Figure 4.26: Bi-linear stress-crack opening relation for steel fiber reinforced concrete with the method in [Nyström, (2008)]

116

In the same figure, it can be seen that the critical crack opening is 7.24 mm and calculated fracture energy, which is the area under bi-linear stress-crack opening, is:

$$G_F = 7153 \frac{J}{m^2} \qquad\qquad (4.41)$$

4.6.2.2 SIFCON (58 MPa)

Although in Nyström, (2008), it was mentioned that only mixed steel fiber reinforced concrete, with low or moderate addition of fibers were used in the study presented and characterization of the post-fracture behavior in tension was applicable to these cases, and may not be valid for other types (like SIFCON) and higher dosages of fibers, since bi-linear curve of SIFCON material could not be found, this method was used for SIFCON also.

Naaman et al. (1993), explain tensile behavior of SIFCON as in the scheme which is shown in below Figure 4.27.
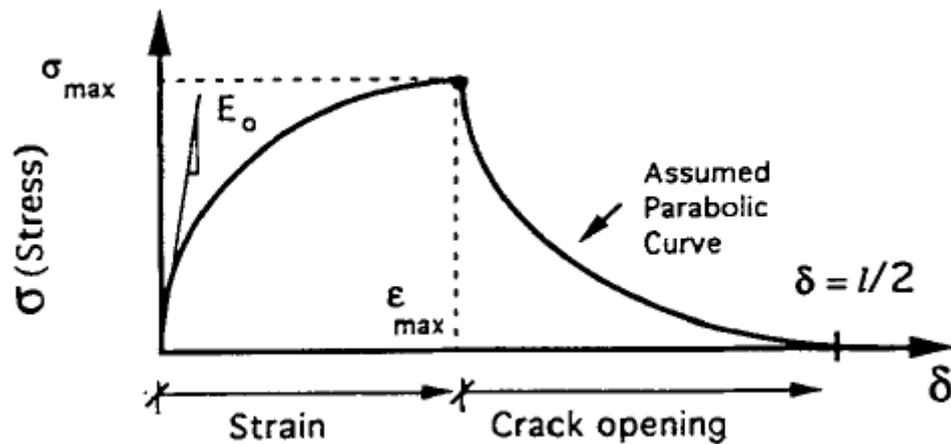
Figure 4.27: Schematic representation of the stress-elongation curve of SIFCON in tension [Naaman et al. (1993)]

117

In order to calculate maximum and minimum fracture energy values for SIFCON, Figure 4.27 was taken as basis. Stress-crack opening relationship can be seen in the second part of the graph which is shows the decrease from σ_{max} to 0, as crack opening value becomes higher. This decrease is defined with an assumed parabolic curve hence, the area under parabola was calculated as $\frac{1}{6}*crackopening*\sigma_{max}$: while assumed tensile strength σ_{max} remained constant, critical crack width changed. As mentioned in Nyström, (2008), w_c can be between $L_f/10$ and $L_f/2$. So, adding to the method used for SFRC, two more values showing maximum and minimum of fracture energy could be gained. As it is expressed in tensile limit section of SIFCON, two values of 5.8 and 8.7 were used for concrete tensile strength and analyses were conducted with three different fracture energy values for each tensile strength. These are shown for each tensile strength in the proceeding sections.

4.6.2.2.1 SIFCON Tensile Limit 5.8

According to the procedure used for SFRC, values of fracture energy were calculated in this manner:

Fracture energy of the 3mm meshed plain concrete which had tensile strength of 5.8 MPa was:

$$G_{F.NSC} = 108 \frac{J}{m^2} \tag{4.42}$$

$$a_1(1/mm) = 54 \tag{4.43}$$

$$a_2(1/mm) = 0.27 \tag{4.44}$$

When σ_t was scaled to 1, b_2 was:

$$b_2 = 0.4684 \tag{4.45}$$

This value was larger than SFRC, since there was two percentage of fiber in SFRC, while in SIFCON there existed twelve percentage of steel fiber.
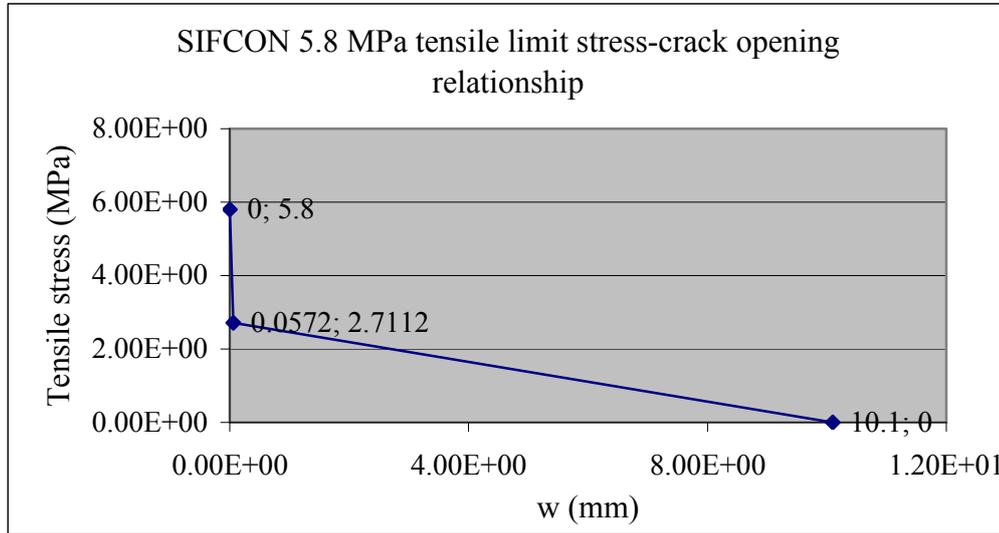
Figure 4.28: Bi-linear stress-crack opening relation for SIFCON (12 percent) with tensile strength 5.8 with the method in [Nyström, (2008)]

Figure 4.28 shows us that critical crack opening is 10.1 mm and fracture energy is found by calculation of area under bi-linear stress-crack opening line as:

$$G_F = 13857 \frac{J}{m^2} \tag{4.46}$$

Fiber used in the SIFCON is Dramix-RL 45/30 which had fiber length of 30 mm. **[Dramix RL-45/30-BN, (2005)].** So minimum and maximum fracture energies were calculated as:

$$G_{F\min} = \frac{1}{6}*5*5.8*10^3 = 5800 \frac{J}{m^2} \tag{4.47}$$

$$G_{F\max} = \frac{1}{6}*25*5.8*10^3 = 29000 \frac{J}{m^2} \tag{4.48}$$

4.6.2.2.2 SIFCON Tensile Limit 8.7

Again according to the procedure used for SFRC, values of fracture energy were calculated in this manner:

Fracture energy of the 3mm meshed plain concrete which had tensile strength 8.7 MPa was:

$$G_{F.NSC} = 108 \frac{J}{m^2} \tag{4.49}$$

$$a_1(1/mm) = 54 \tag{4.50}$$

$$a_2(1/mm) = 0.27 \tag{4.51}$$

When σ_t was scaled to 1, b_2 was:

$$b_2 = 0.4684 \tag{4.52}$$

This value came out to be the same as in the previous SIFCON calculations since here also 12 percent fiber existed in SIFCON.
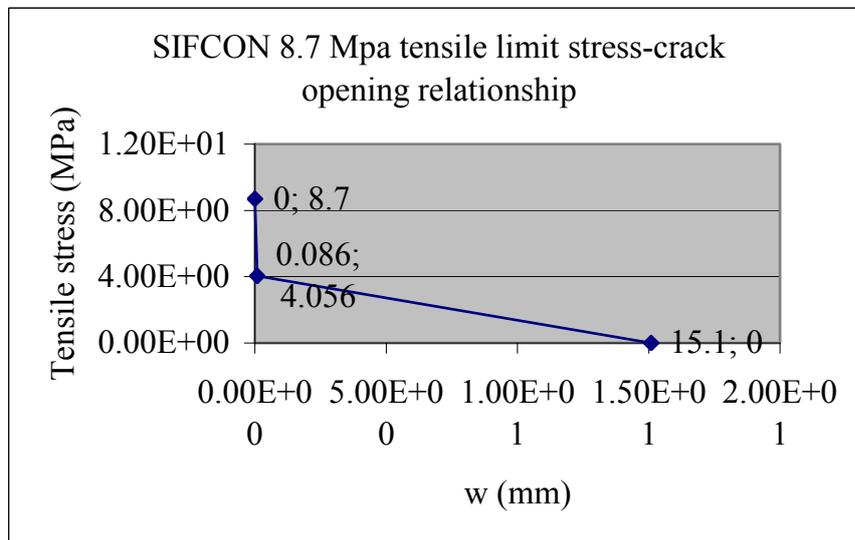
Figure 4.29: Bi-linear stress-crack opening relation for SIFCON (12 percent) with tensile strength 8.7 MPa with the method in [Nyström, (2008)]

It can be seen in Figure 4.29 that critical crack opening is 15.1 mm and fracture energy is found by calculation of the area under bi-linear stress-crack opening line as:

$$G_F = 31000 \frac{J}{m^2} \qquad (4.53)$$

While maximum and minimum fracture energies were calculated in the same manner as:

$$G_{F\min} = \frac{1}{6} * 5 * 8.7 * 10^3 = 8700 \frac{J}{m^2} \qquad (4.54)$$

$$G_{F\max} = \frac{1}{6} * 25 * 8.7 * 10^3 = 43500 \frac{J}{m^2} \qquad (4.55)$$

4.7 Erosion

Erosion Model Part in AUTODYN, (2007) is used to summarize this section.In AUTODYN (2007), it is claimed as during the simulations, some of the Lagrangian cells are distorted very much and if no remedial action is taken, progress of the calculation can seriously be impaired. Therefore procedures of the software permit removal of such Lagrangian cells from the calculation if the pre-defined strain exceeds the specified limit. Erosion is not true modeling of a physical phenomena but a numerical palliative introduced to overcome the problems associated with the mesh distortions caused by gross motions of a Lagrangian grid. There are 3 options for erosion models in AUTODYN:

- Effective plastic strain: Erosion is initiated by effective plastic strain limit
- Incremental Geometric strain: Erosion is initiated by an incremental geometric strain limit
- Instantaneous Geometric strain: Erosion is initiated by an instantaneous geometric strain limit

Chosen for simulations here is the instantaneous geometric strain option. The reason of choosing it among others is: instantaneous geometric strain is directly calculated from principal strain components and therefore, it can increase and decrease by loading and unloading while this behavior is not valid neither for effective plastic strain, nor for incremental geometric strain since they always increase monotonically [AUTODYN Theory Manual, (2005)].Several erosion values were tried to see the effect on both crater diameter and residual impact velocity. These are listed for projectile and target below. Analyses results for different combinations of erosion and failure are shown in Chapter 5.

4.7.1 Projectile-Tung.Alloy Material

In order to model projectile, Tung.Alloy material was used. Different instantaneous geometric strain values used for this material are shown in Table 4.10

Table 4.10: Instantaneous Geometric Strain Values for Tung.Alloy Material

Instantaneous geometric strain values-Tung.Alloy
1
2
4

4.7.2 Target- Plain Concrete Type A (30 MPa)

Concrete-L material model was chosen for the simulation of plain concrete with 30 MPa compressive strength. Different instantaneous geometric strain values used in modeling of Concrete-L material are shown in Table 4.11.

Table 4.11: Instantaneous Geometric Strain Values for Concrete-L Material used in plain concrete type A (30 MPa)

Instantaneous geometric strain values for Concrete-L material model
0.5
2
4

4.7.3 Target- Plain Concrete Type B (55 MPa)

Concrete 48 MPa Drucker-Prager material model values were found as a result of literature survey of the thesis and used for modeling of plain concrete (55 MPa). Instantaneous geometric strain values used for this material are shown in Table 4.12.

Table 4.12: Instantaneous Geometric Strain Values for Concrete 48 MPa Material used in plain concrete type B (55 MPa)

Instantaneous geometric strain values for Concrete 48 MPa material model
0.5
2
4

4.7.4 2 percent Steel Fiber Reinforced Concrete (SFRC) (61 MPa)

2 percent steel fiber reinforced concrete (SFRC) with 61 MPa compressive strength was obtained by the use of concrete 48 MPa Drucker-Prager material model model. Data used for instantaneous geometric strain for this material is shown in Table 4.13 below:

Table 4.13: Instantaneous Geometric Strain Values for CONCRETE 48 MPa
Material used in 2 percent SFRC

Instantaneous geometric strain values for Concrete 48 MPa material model
2

4.7.5 SIFCON (58 MPa)

Like SFRC modeling, SIFCON (58 MPa) was also modeled with some adjustment on concrete 48 MPa Drucker-Prager material model. Instantaneous geometric strain is shown in Table 4.14:

Table 4.14: Instantenous Geometric Strain Values for CONCRETE 48 MPa
Material used in 12 percent SIFCON

Instantaneous geometric strain values for Concrete 48 MPa material model
2

CHAPTER 5

RESULTS AND COMPARISONS

5.1   Introduction

The specimens of the experiments were modeled and analyzed in the same fashion explained in Chapter 4. Outcomes will be mentioned under the target deformations and the residual velocities sections for both computational and the experimental work. Under the target deformations and residual velocities sections, results are divided into three groups named: concrete, SFRC and SIFCON. Comparisons are also executed in the same manner. In order to make comparisons in a more efficient manner, names of the simulated models are given the same as the experimental ones. Discussion of the results takes place at the end of this chapter.

5.2   Results of the Computational Work

5.2.1   Target Deformations

In this section, target deformations belonging to the concrete, SFRC and SIFCON groups will be mentioned subsequently. Black lines drawn on the deformation views were the boundaries where crater radius and depths were approximated.

5.2.1.1 Deformations of the Concrete Group Models

The results of the analyses for Specimens 1-1, 1-2 and 1-3 will be expressed here. Configuration of concrete group specimens is shown according to material location in the Figure 5.1 below.
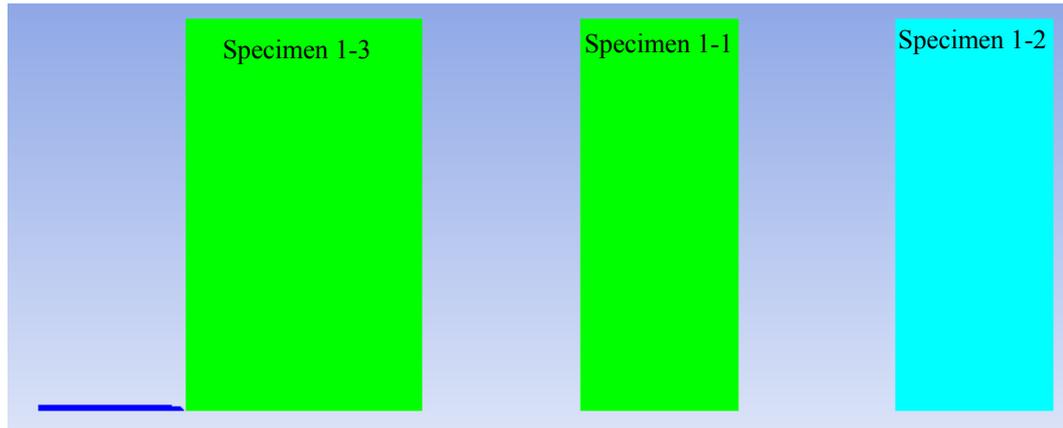
Figure 5.1: Configuration of concrete group specimens

5.2.1.1.1 Deformation of the Specimen 1-3

In order to see the effects of tensile stress and geometric strain parameters on the results of the simulations, five different trials were conducted. In all of them, Concrete-L model strength and EOS data were used for modeling concrete while, Tung.Alloy model strength and EOS data were used for projectile [AUTODYN, (2007)]. Depths of the models were 0.6 m which was the same as the experimental one. View of the deformed target for each trial will be given after input values of changing parameters and the crater radius, depth, volume results for front and back faces are given in a tabular form. Characteristics of these trials can be seen in Table 5.1, Table 5.3, Table 5.5, Table 5.7, Table 5.9, deformations of the trials are explained in Table 5.2, Table 5.4, Table 5.6, Table 5.8, Table 5.10 and deformed images are given in Figure 5.2-5.6.

- First Trial

Table 5.1: Characteristics of the first trial

Trial No	Tensile limit (MPa)	Reheal	Concrete erosion strain	Projectile erosion strain
1	-2.5	No	0.5	4

Table 5.2: Deformations of the first trial

Front face			Back face		
Crater radius (cm)	Crater depth (cm)	Crater volume (cm^3)	Crater radius (cm)	Crater depth (cm)	Crater volume (cm^3)
22	11	5575	35	6.5	8338
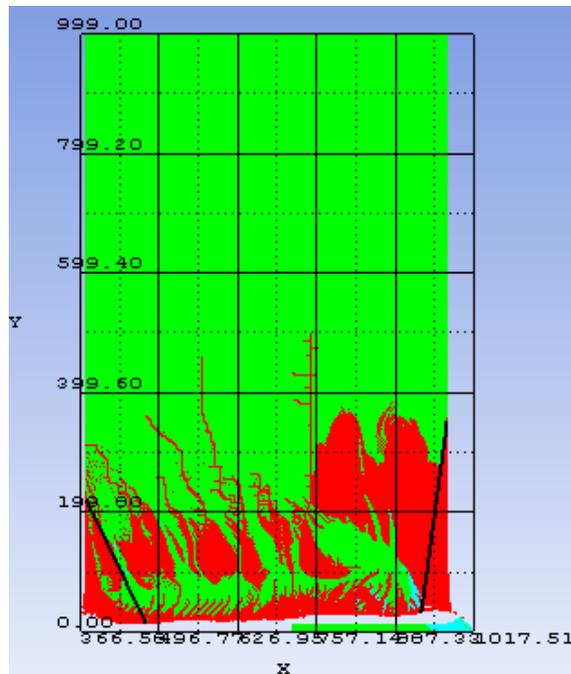
Figure 5.2: Deformed view of the first trial

- Second Trial

Table 5.3: Characteristics of the second trial

Trial No	Tensile limit (MPa)	Reheal	Concrete erosion strain	Projectile erosion strain
2	-2.5	No	4	2

Table 5.4: Deformations of the second trial

Front face			Back face		
Crater radius (cm)	Crater depth (cm)	Crater volume (cm^3)	Crater radius (cm)	Crater depth (cm)	Crater volume (cm^3)
47	30	69397	57	4	13609
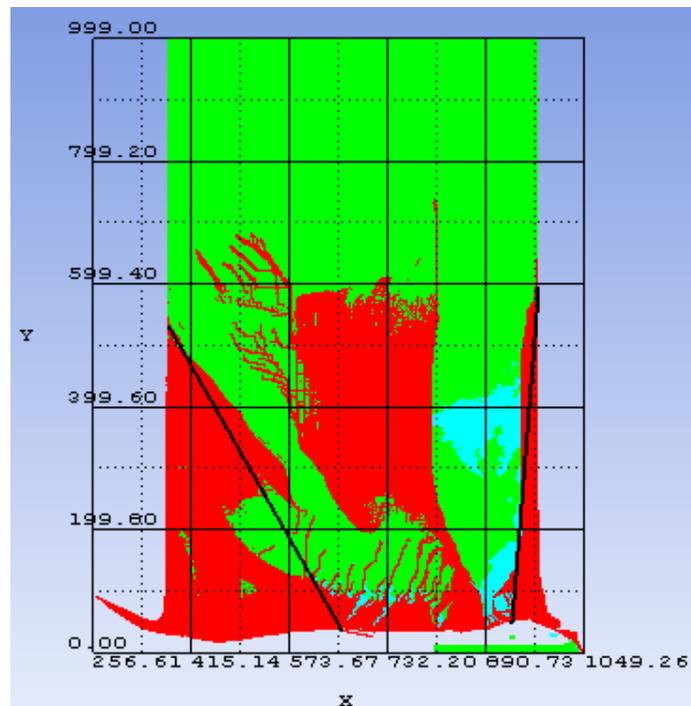
Figure 5.3: Deformed view of the second trial

128

- Third Trial

Table 5.5: Characteristics of the third trial

Trial No	Tensile limit (MPa)	Reheal	Concrete erosion strain	Projectile erosion strain
3	-2.75	No	0.5	4

Table 5.6: Deformations of the third trial

Front face			Back face		
Crater radius (cm)	Crater depth (cm)	Crater volume (cm^3)	Crater radius (cm)	Crater depth (cm)	Crater volume (cm^3)
25	11	7200	38	8	12097
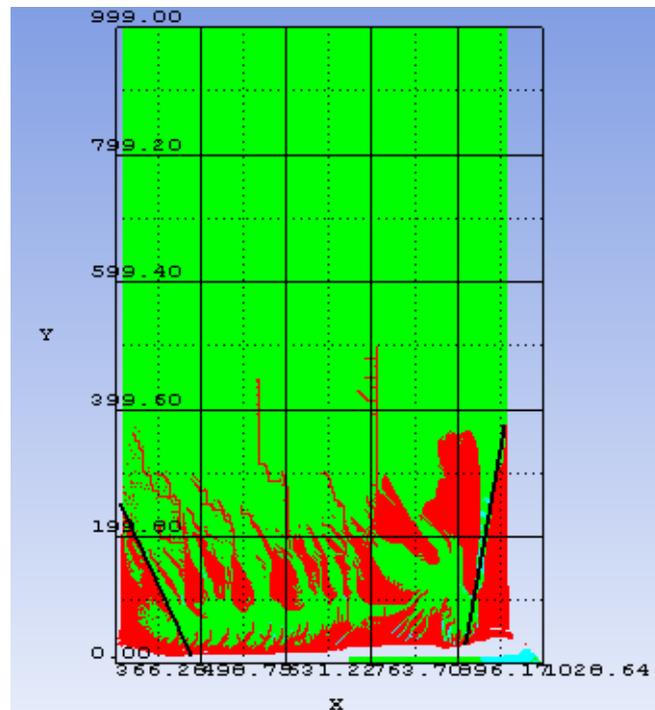
Figure 5.4: Deformed view of the third trial

129

- Fourth Trial

Table 5.7: Characteristics of the fourth trial

Trial No	Tensile limit (MPa)	Reheal	Concrete erosion strain	Projectile erosion strain
4	-3	No	0.5	4

Table 5.8: Deformations of the fourth trial

Front face			Back face		
Crater radius (cm)	Crater depth (cm)	Crater volume (cm^3)	Crater radius (cm)	Crater depth (cm)	Crater volume (cm^3)
20	8	3351	30	5	4712
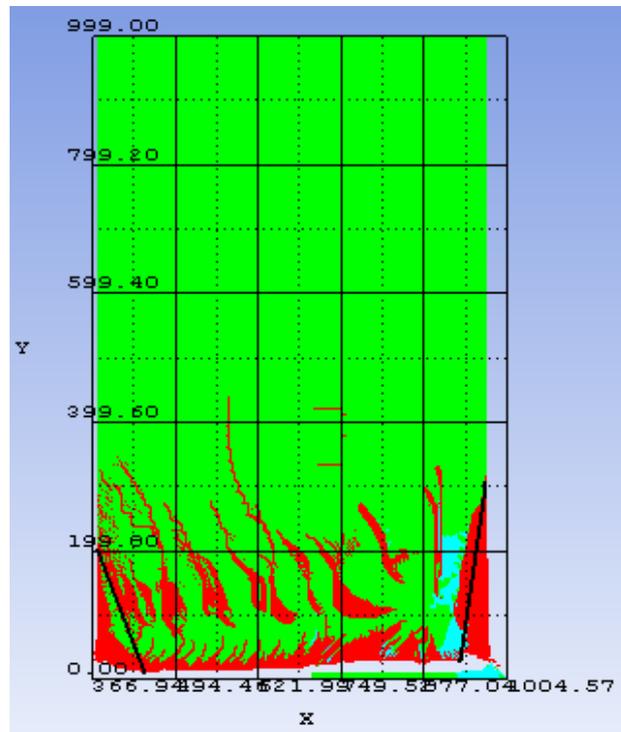
Figure 5.5: Deformed view of the fourth trial

- Fifth Trial

Table 5.9: Characteristics of the fifth trial

Trial No	Tensile limit (MPa)	Reheal	Concrete erosion strain	Projectile erosion strain
5	-3	Yes	2	2

Table 5.10: Deformations of the fifth trial

Front face			Back face		
Crater radius (cm)	Crater depth (cm)	Crater volume (cm^3)	Crater radius (cm)	Crater depth (cm)	Crater volume (cm^3)
11	9	1140	18	2	679
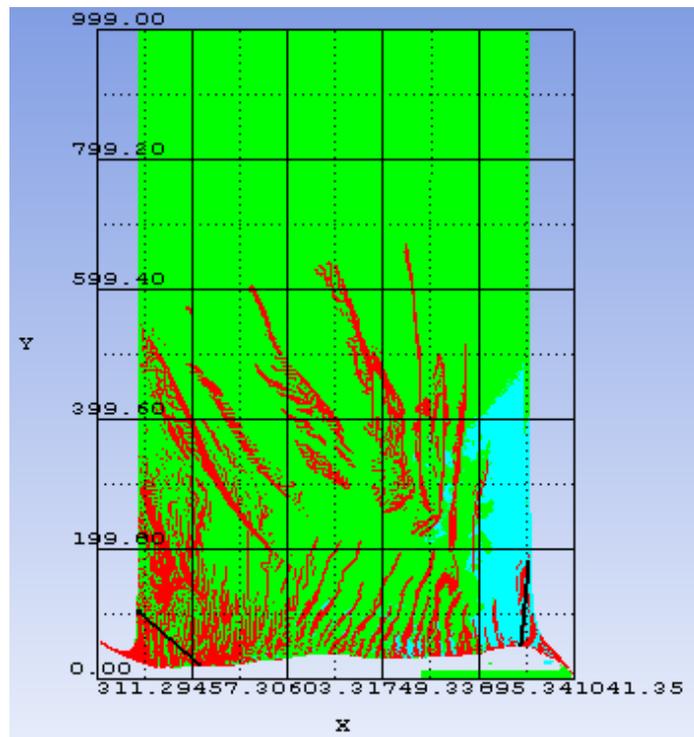
Figure 5.6: Deformed view of the fifth trial

5.2.1.1.2 Deformation of the Specimen 1-1

The analyses of the specimen 1-1, has the same concrete and projectile properties as the specimen 1-3 possesses in default. Concrete-L and Tung.Alloy model properties were used in terms of strength and EOS data for concrete and projectile [AUTODYN, (2007)]. Since results of the Specimen 1-3's third trial was the one closest to experimental value among them (details can be seen in the Comparison section), characteristics of this specimen was chosen to be the same as in the third trial of Specimen 1-3 and deformed projectile was also obtained from the same simulation trial. The only difference in concrete geometry was the depth of concrete target which was 0.4 m in this model. Specimen 1-1 of the experiment also has the same depth. Characteristics and results of Specimen 1-1 can be seen in Table 5.11 and Table 5.12 below. Deformed image of the specimen is shown in Figure 5.7.

Table 5.11: Characteristics of the specimen 1-1

Trial No	Tensile limit (MPa)	Reheal	Concrete erosion strain	Projectile erosion strain
1	-2.75	No	0.5	4

Table 5.12: Deformations of the Specimen 1-1

Front face			Back face		
Crater radius (cm)	Crater depth (cm)	Crater volume (cm^3)	Crater radius (cm)	Crater depth (cm)	Crater volume (cm^3)
43	16	30980	48	11	26540
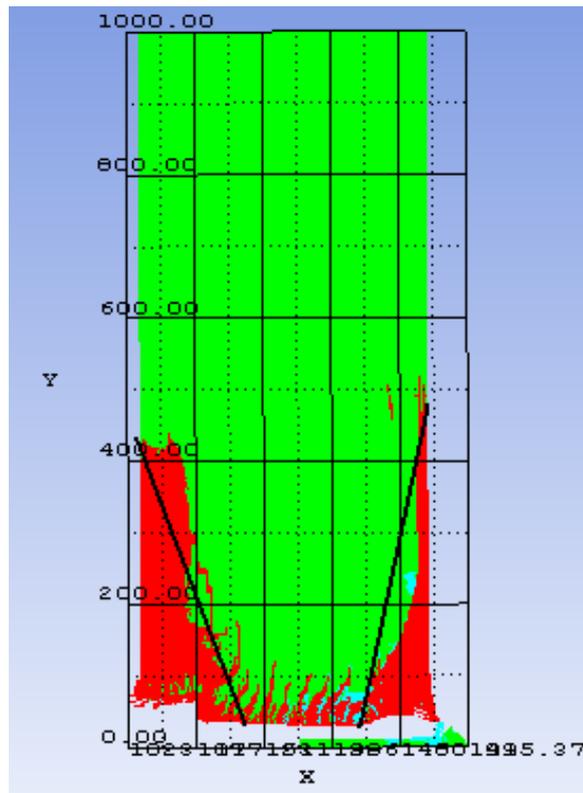
Figure 5.7: Deformed view of the Specimen 1-1

5.2.1.1.3 Deformation of the Specimen 1-2

For the Specimen 1-2 simulations, Concrete 48 MPa Drucker-Prager Model strength-EOS data [Tham, (2005)], and Tung.Alloy model strength-EOS data [AUTODYN, (2007)] were used for concrete and projectile. The deformed projectile of Specimen 1-1 was struck at Specimen 1-3 and target depth was 0.4 m. In other to search the erosion and tensile limit parameters, seven trials were conducted here. Characteristics of these trials can be seen in Table 5.13, Table 5.15, Table 5.17, Table 5.19, Table 5.21, Table 5.23, Table 5.25 deformations of the trials are explained in and Table 5.14, Table 5.16, Table 5.18, Table 5.20, Table 5.22, Table 5.24, Table 5.26 deformed images of are shown in Figure 5.8-5.14.

133

- First Trial

Table 5.13: Characteristics of the first trial

Trial No	Tensile limit (MPa)	Reheal	Concrete erosion strain	Projectile erosion strain
1	-1	No	0.5	1

Table 5.14: Deformations of the first trial

Front face			Back face		
Crater radius (cm)	Crater depth (cm)	Crater volume (cm^3)	Crater radius (cm)	Crater depth (cm)	Crater volume (cm^3)
18	6	2036	75	14	82467
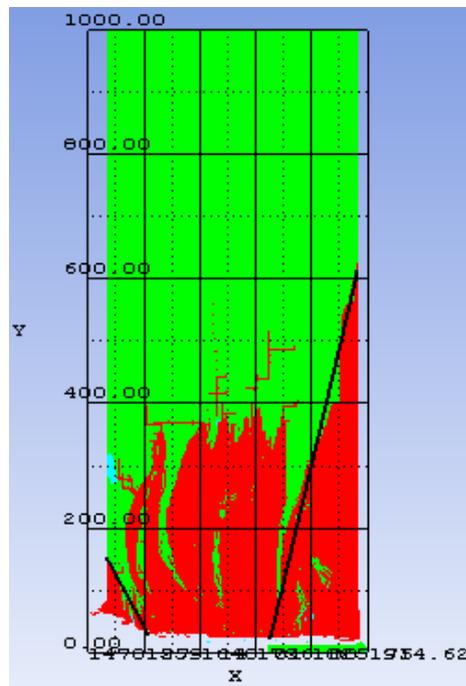
Figure 5.8: Deformed view of the first trial

134

- Second Trial

Table 5.15: Characteristics of the second trial

Trial No	Tensile limit (MPa)	Reheal	Concrete erosion strain	Projectile erosion strain
2	-1.25	No	0.5	1

Table 5.16: Deformations of the second trial

Front face			Back face		
Crater radius (cm)	Crater depth (cm)	Crater volume (cm^3)	Crater radius (cm)	Crater depth (cm)	Crater volume (cm^3)
20	11	4608	17	13	3934
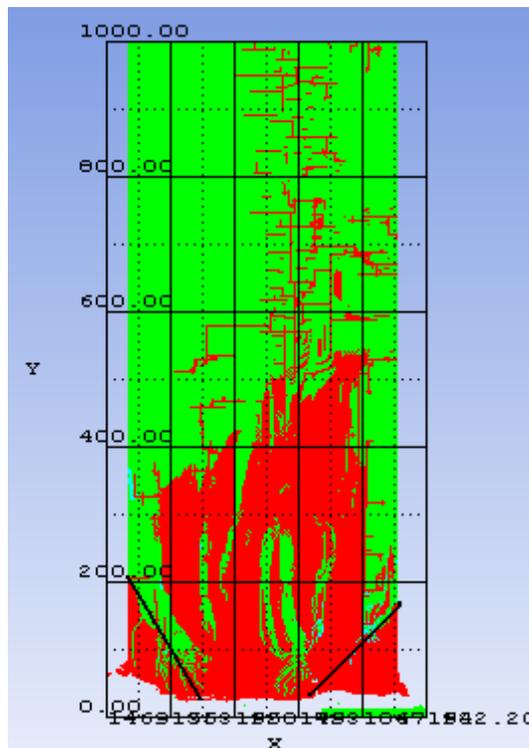
Figure 5.9: Deformed view of the second trial

135

- Third Trial

Table 5.17: Characteristics of the third trial.

Trial No	Tensile limit (MPa)	Reheal	Concrete erosion strain	Projectile erosion strain
3	-1.5	No	0.5	1

Table 5.18: Deformations of the third trial

Front face			Back face		
Crater radius (cm)	Crater depth (cm)	Crater volume (cm^3)	Crater radius (cm)	Crater depth (cm)	Crater volume (cm^3)
16	12	3217	38	7	10585
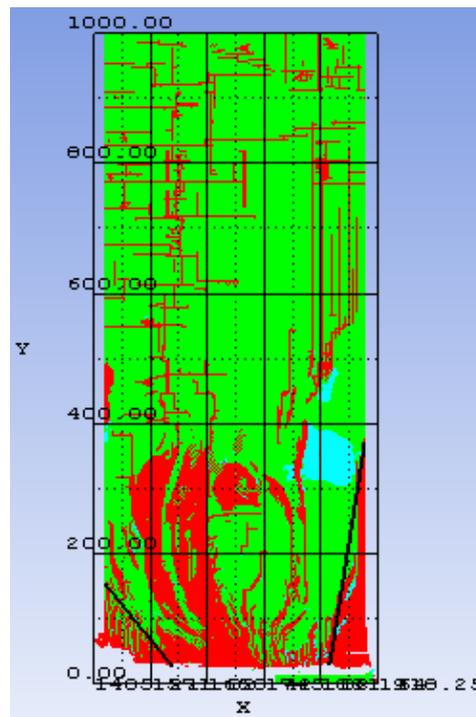
Figure 5.10: Deformed view of the third trial

136

- Fourth Trial

Table 5.19: Characteristics of the fourth trial

Trial No	Tensile limit (MPa)	Reheal	Concrete erosion strain	Projectile erosion strain
4	-1.75	No	0.5	1

Table 5.20: Deformations of the fourth trial

Front face			Back face		
Crater radius (cm)	Crater depth (cm)	Crater volume (cm^3)	Crater radius (cm)	Crater depth (cm)	Crater volume (cm^3)
7	9	462	18	8	2714
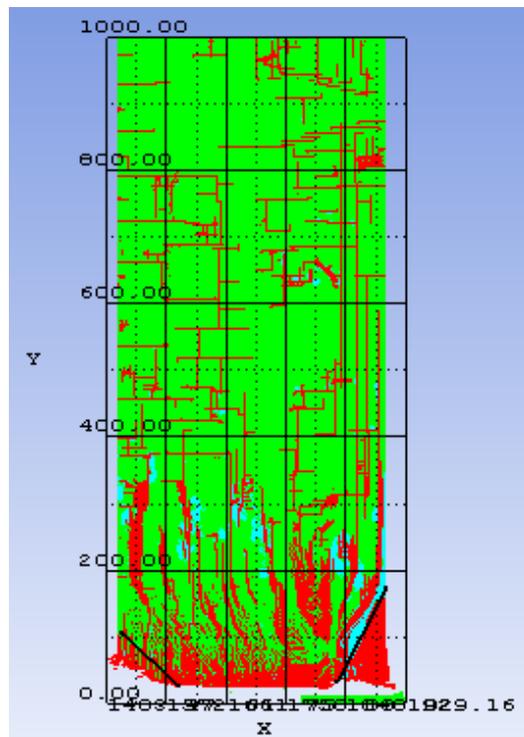
Figure 5.11: Deformed view of the fourth trial

137

- Fifth Trial

Table 5.21: Characteristics of the fifth trial

Trial No	Tensile limit (MPa)	Reheal	Concrete erosion strain	Projectile erosion strain
5	-1.75	No	2	2

Table 5.22: Deformations of the fifth trial

| Front face			Back face		
Crater radius (cm)	Crater depth (cm)	Crater volume (cm^3)	Crater radius (cm)	Crater depth (cm)	Crater volume (cm^3)
17	9	2724	19	7	2646
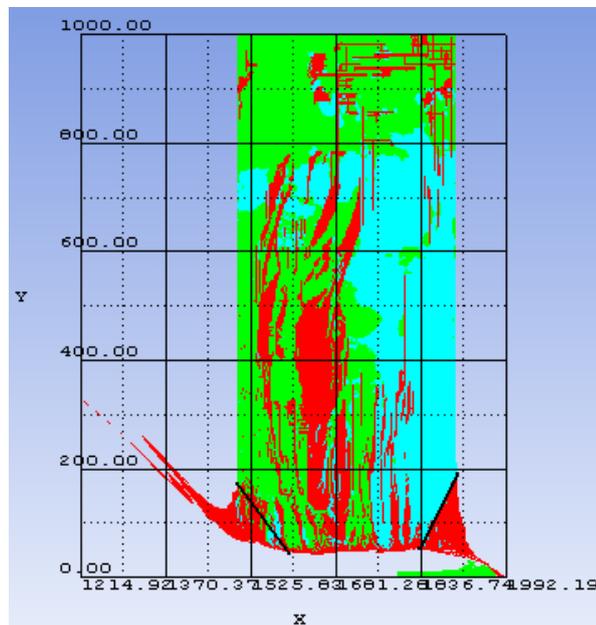
Figure 5.12: Deformed view of the fifth trial

- Sixth Trial

Table 5.23: Characteristics of the sixth trial

Trial No	Tensile limit (MPa)	Reheal	Concrete erosion strain	Projectile erosion strain
6	-3	No	0.5	4

Table 5.24: Deformations of the sixth trial

Front face			Back face		
Crater radius (cm)	Crater depth (cm)	Crater volume (cm^3)	Crater radius (cm)	Crater depth (cm)	Crater volume (cm^3)
13	6	1062	10	10	1047
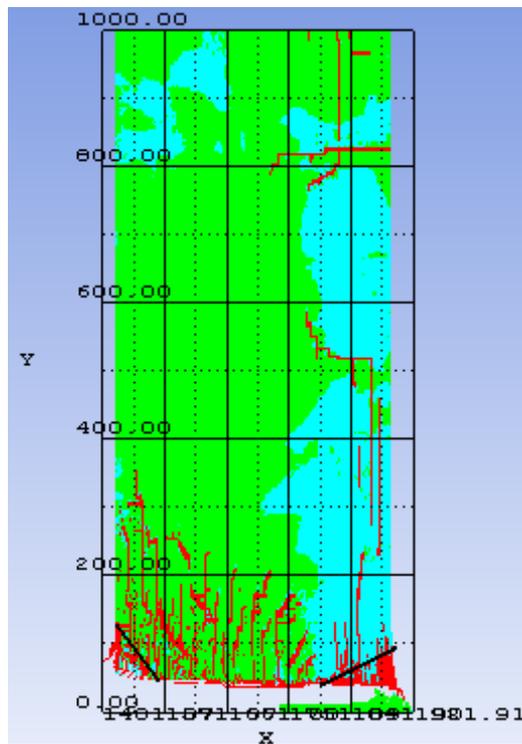
Figure 5.13: Deformed view of the sixth trial

139

- Seventh Trial

Table 5.25: Characteristics of the seventh trial

Trial No	Tensile limit (MPa)	Reheal	Concrete erosion strain	Projectile erosion strain
7	-4	No	0.5	4

Table 5.26: Deformations of the seventh trial

Front face			Back face		
Crater radius (cm)	Crater depth (cm)	Crater volume (cm^3)	Crater radius (cm)	Crater depth (cm)	Crater volume (cm^3)
14	6	1232	8	4	268
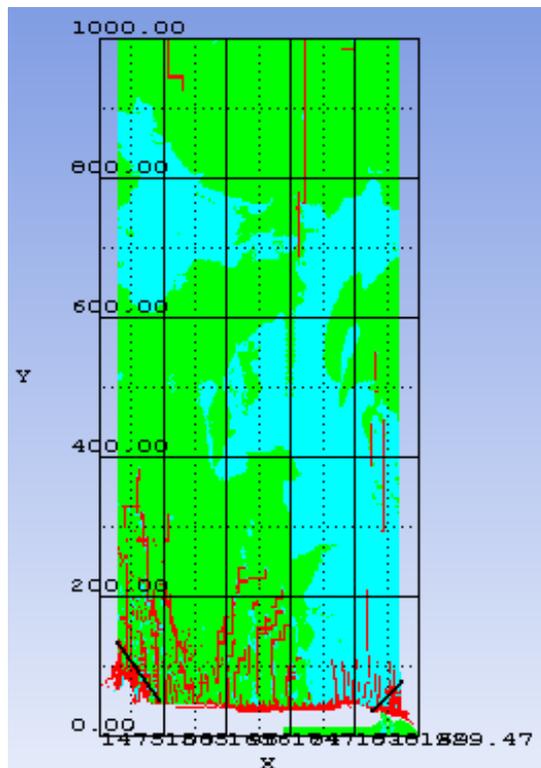
Figure 5.14: Deformed view of the seventh trial

140

5.2.1.2   Deformations of the SFRC Group Models

This group consists of Specimens 2-2 and 2-3. Modeling and analyses of SFRC specimens were conducted in the fashion which have been explained in Chapter 4. Concrete 48 MPa material model strength-EOS data [Tham, (2005)], and Tung.Alloy model strength-EOS data [AUTODYN, (2007)] were used for concrete and projectile in these simulations also. Depth of the target specimens were 0.6 m. Configuration of SFRC group specimens can be seen according to material locations in Figure 5.15. Results for Specimen 2-2 and 2-3 can be seen subsequently.
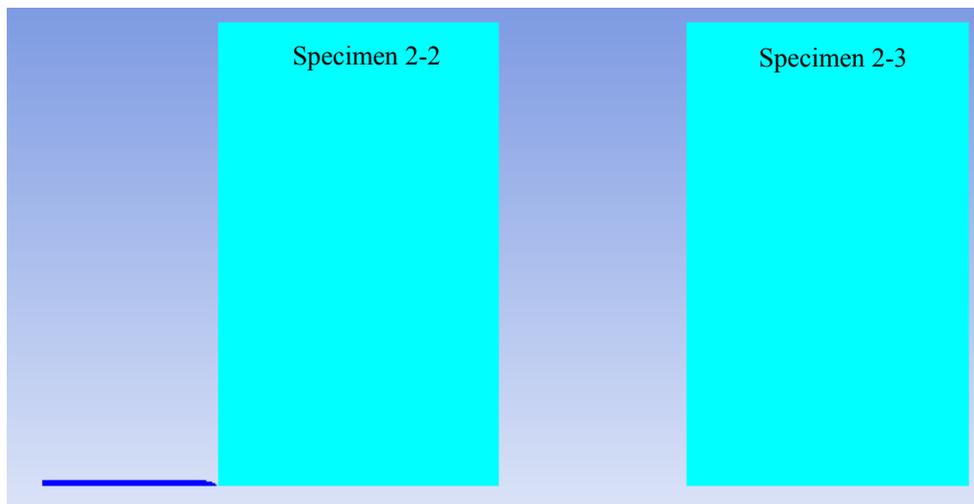
Figure 5.15: Configuration of SFRC group specimens

5.2.1.2.1   Deformation of the Specimen 2-2

The characteristics of the Specimen 2-2 are shown in Table 5.27, deformations are explained in Table 5.28 and deformed images can be viewed in Figure 5.16.

141

Table 5.27: Characteristics of the Specimen 2-2

Trial No	Tensile limit (MPa)	Fracture energy $(\frac{J}{m^2})$	Reheal	Concrete erosion strain	Projectile erosion strain
1	-4.75	7153	No	2	4

Table 5.28: Deformations of the Specimen 2-2

| Front face			Back face		
Crater radius (cm)	Crater depth (cm)	Crater volume (cm³)	Crater radius (cm)	Crater depth (cm)	Crater volume (cm³)
7	4	205	14	6	1252
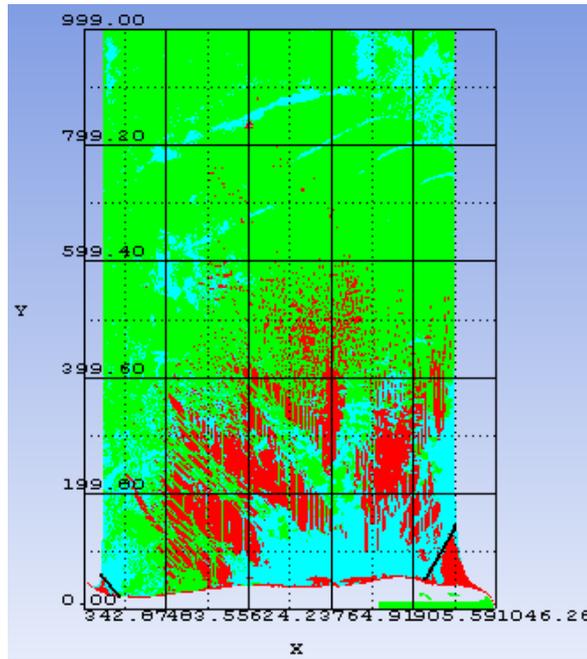
Figure 5.16: Deformed view of the Specimen 2-2

5.2.1.2.2   Deformation of the Specimen 2-3

Specimen 2-3 characteristics are shown in Table 5.29, deformations are explained in Table 5.30 and deformed image of were shown in Figure 5.17. Projectile deformed through Specimen 2-2 was used here.

Table 5.29: Characteristics of the Specimen 2-3

Trial No	Tensile limit (MPa)	Fracture energy ($\frac{J}{m^2}$)	Reheal	Concrete erosion strain	Projectile erosion strain
1	-4.75	7153	No	2	4

Table 5.30: Deformations of the specimen 2-3

Front face			Back face		
Crater radius (cm)	Crater depth (cm)	Crater volume (cm^3)	Crater radius (cm)	Crater depth (cm)	Crater volume (cm^3)
12	11	1660	20	13	5445
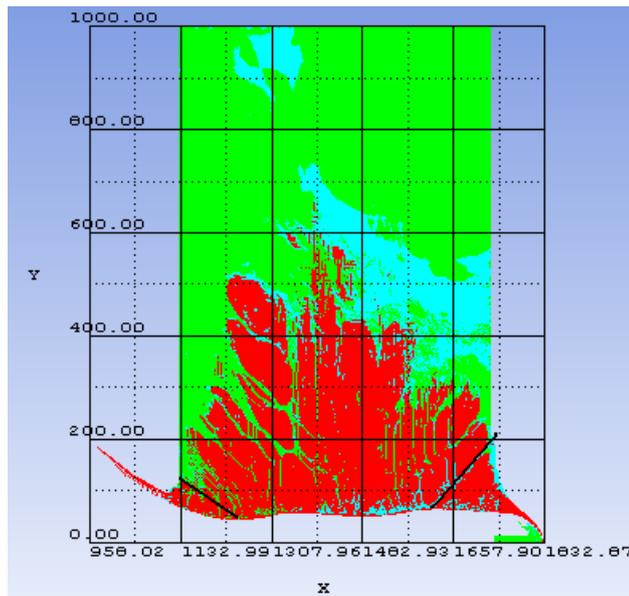
Figure 5.17: Deformed view of the Specimen 2-3

5.2.1.3   Deformations of the SIFCON Group Models

Specimens 3-2 and 3-3 belong to this group. Procedure for SIFCON modeling and simulation has been explained in Chapter 4 just like the previously mentioned two groups. Concrete 48 MPa Drucker-Prager Model [Tham, (2005)], strength-EOS data and Tung.Alloy model strength-EOS data [AUTODYN, (2007)] were used in these models also. Target depth was 0.6 m. For n^{th} trial of Specimen 3-3's projectile, n^{th} trial of Specimen 3-2's deformed one was used. This configuration for SIFCON group specimens can be seen according to material locations in Figure 5.18. Both of the specimens' characteristics together with craters' radius, depth, volume and deformed images are explained successively.

144
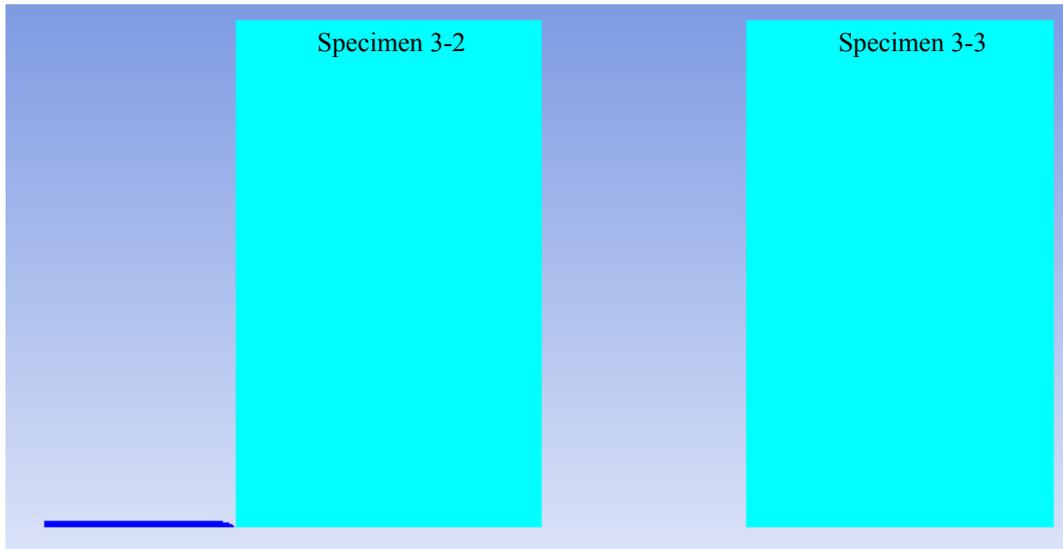
Figure 5.18: Configuration of SIFCON group specimens

5.2.1.3.1 Deformation of the Specimen 3-2

The Specimen 3-2 characteristics are shown in Table 5.31, Table 5.33, Table 5.35, Table 5.37, Table 5.39, Table 5.41 deformations of the specimens are explained in Table 5.32, Table 5.34, Table 5.36 , Table 5.38,Table 5.40, Table 5.42 deformed images of are shown in Figures 5.19-5.24.

- First Trial

Table 5.31: Characteristics of the first trial

Trial No	Tensile limit (MPa)	Fracture energy $(\frac{J}{m^2})$	Reheal	Concrete erosion strain	Projectile erosion strain
1	-5.8	5800	No	2	4

145

Table 5.32: Deformations of the first trial

Front face			Back face		
Crater radius (cm)	Crater depth (cm)	Crater volume (cm^3)	Crater radius (cm)	Crater depth (cm)	Crater volume (cm^3)
4	3	50	10	3	314
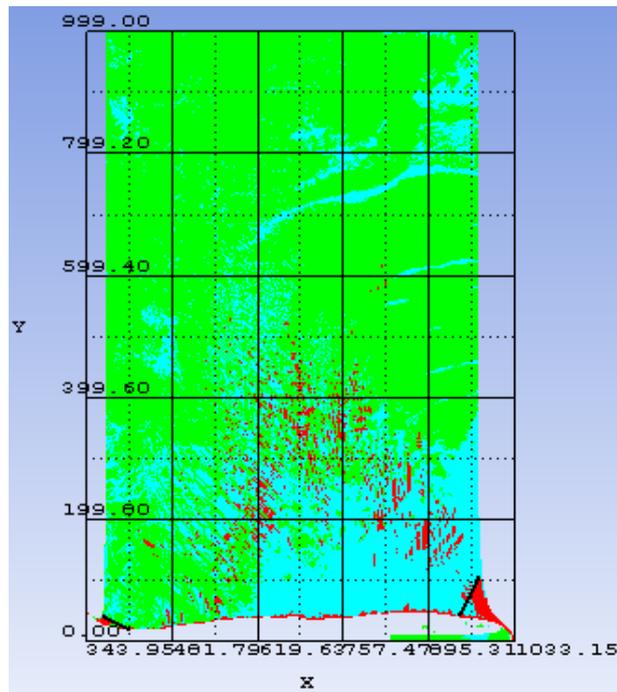
Figure 5.19: Deformed view of the first trial

- Second Trial

Table 5.33: Characteristics of the second trial

Trial No	Tensile limit (MPa)	Fracture energy ($\frac{J}{m^2}$)	Reheal	Concrete erosion strain	Projectile erosion strain
2	-5.8	13857	No	2	4

Table 5.34: Deformations of the second trial

| Front face			Back face		
Crater radius (cm)	Crater depth (cm)	Crater volume (cm^3)	Crater radius (cm)	Crater depth (cm)	Crater volume (cm^3)
4	4	67	10	4	419
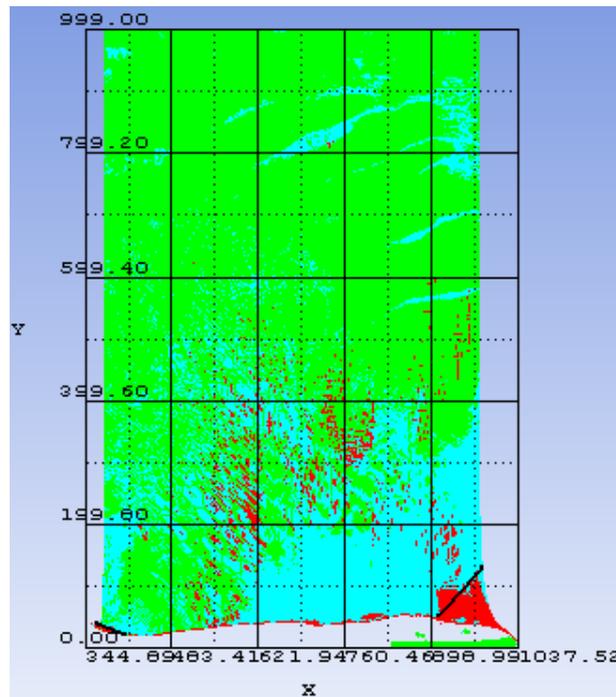
Figure 5.20: Deformed view of the second trial

- Third Trial

Table 5.35: Characteristics of the third trial

Trial No	Tensile limit (MPa)	Fracture energy ($\frac{J}{m^2}$)	Reheal	Concrete erosion strain	Projectile erosion strain
3	-5.8	29000	No	2	4

147

Table 5.36: Deformations of the third trial

| Front face			Back face		
Crater radius (cm)	Crater depth (cm)	Crater volume (cm^3)	Crater radius (cm)	Crater depth (cm)	Crater volume (cm^3)
5	3	79	12	7	1056
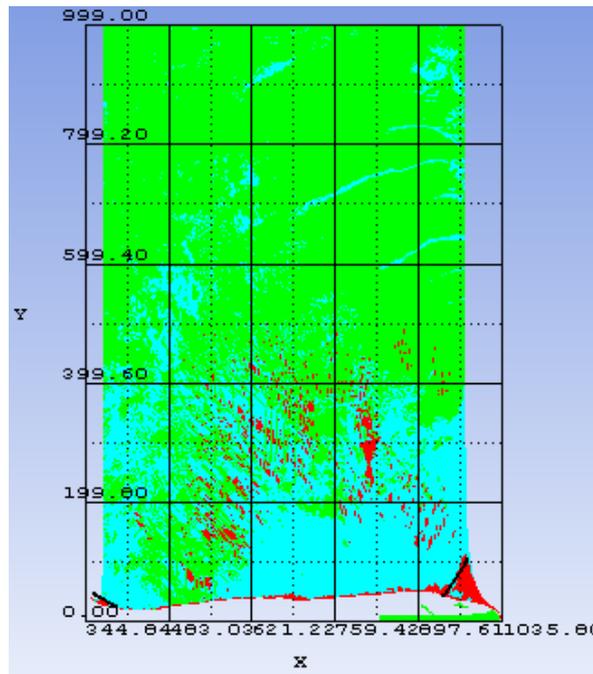
Figure 5.21: Deformed view of the third trial

- Fourth Trial

Table 5.37: Characteristics of the fourth trial

Trial No	Tensile limit (MPa)	Fracture energy ($\frac{J}{m^2}$)	Reheal	Concrete erosion strain	Projectile erosion strain
4	-8.7	8700	No	2	4

Table 5.38: Deformations of the fourth trial

Front face			Back face		
Crater radius (cm)	Crater depth (cm)	Crater volume (cm³)	Crater radius (cm)	Crater depth (cm)	Crater volume (cm³)
4	2	34	13	7	1239
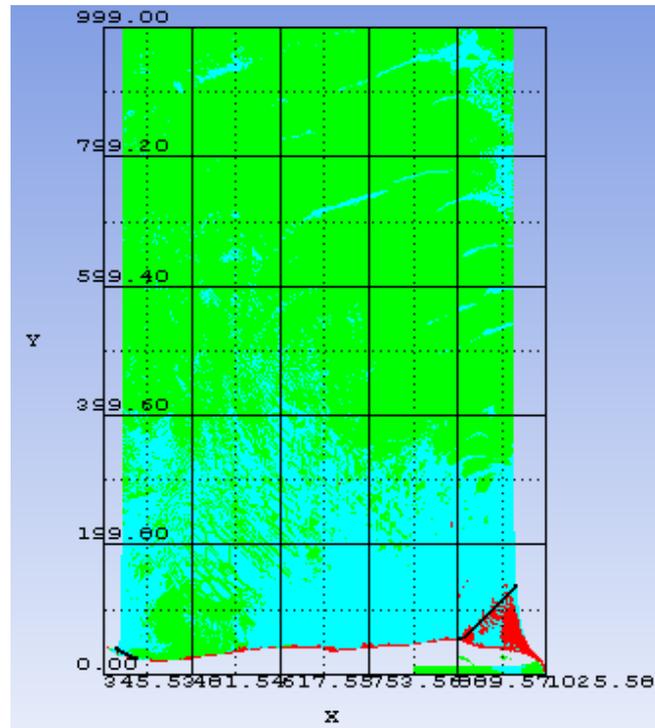
Figure 5.22: Deformed view of the fourth trial

- Fifth Trial

Table 5.39: Characteristics of the fifth trial

Trial No	Tensile limit (MPa)	Fracture energy ($\frac{J}{m^2}$)	Reheal	Concrete erosion strain	Projectile erosion strain
5	-8.7	31000	No	2	4

Table 5.40: Deformations of the fifth trial

Front face			Back face		
Crater radius (cm)	Crater depth (cm)	Crater volume (cm^3)	Crater radius (cm)	Crater depth (cm)	Crater volume (cm^3)
4	3	50	8	6	402
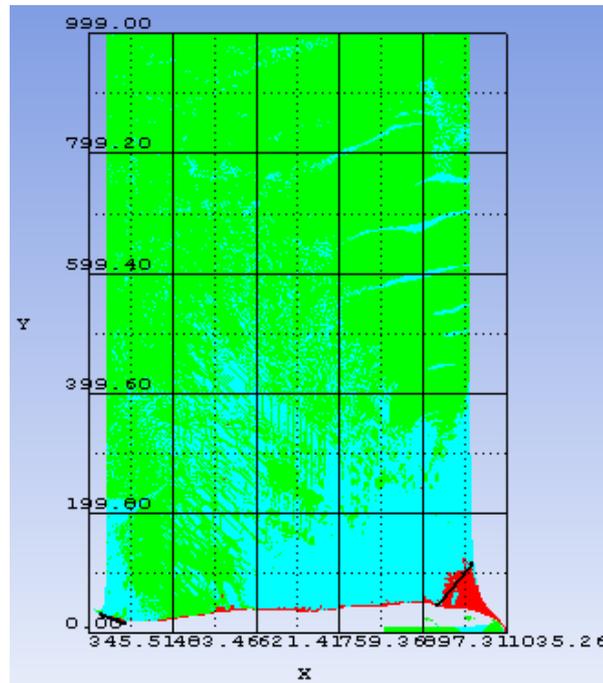
Figure 5.23: Deformed view of the fifth trial

- Sixth Trial

Table 5.41: Characteristics of the sixth trial

Trial No	Tensile limit (MPa)	Fracture energy ($\frac{J}{m^2}$)	Reheal	Concrete erosion strain	Projectile erosion strain
6	-8.7	43500	No	2	4

Table 5.42: Deformations of the sixth trial

Front face			Back face		
Crater radius (cm)	Crater depth (cm)	Crater volume (cm^3)	Crater radius (cm)	Crater depth (cm)	Crater volume (cm^3)
5	4	105	9	4	339
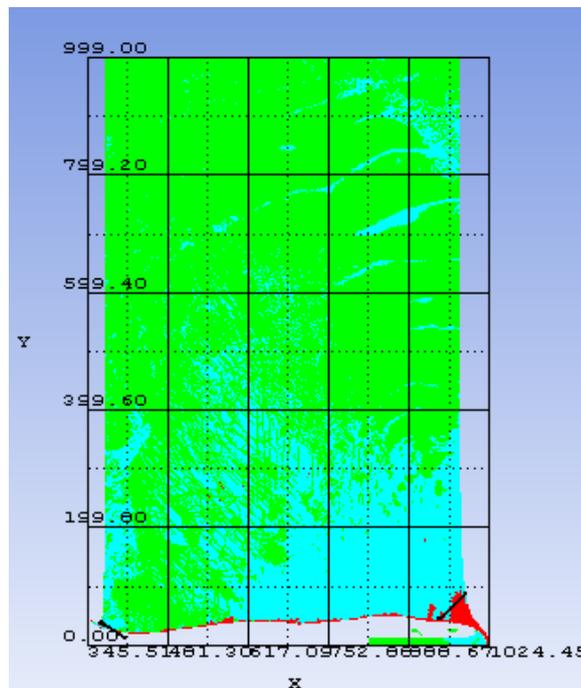
Figure 5.24: Deformed view of the sixth trial

5.2.1.3.2 Deformation of the Specimen 3-3

Characteristics of the Specimen 3-3 are shown in Table 5.43, Table 5.45, Table 5.47, Table 5.49, Table 5.51, Table 5.53 deformations of the specimens are explained in Table 5.44, Table 5.46, Table 5.48, Table 5.50, Table 5.52, Table 5.54 and deformed images are shown in Figures 5.25-5.30.

- First Trial

Table 5.43: Characteristics of the first trial

Trial No	Tensile limit (MPa)	Fracture energy ($\frac{J}{m^2}$)	Reheal	Concrete erosion strain	Projectile erosion strain
1	-5.8	5800	No	2	4

Table 5.44: Deformations of the first trial

Front face			Back face		
Crater radius (cm)	Crater depth (cm)	Crater volume (cm^3)	Crater radius (cm)	Crater depth (cm)	Crater volume (cm^3)
18	11	3732	10	7	733
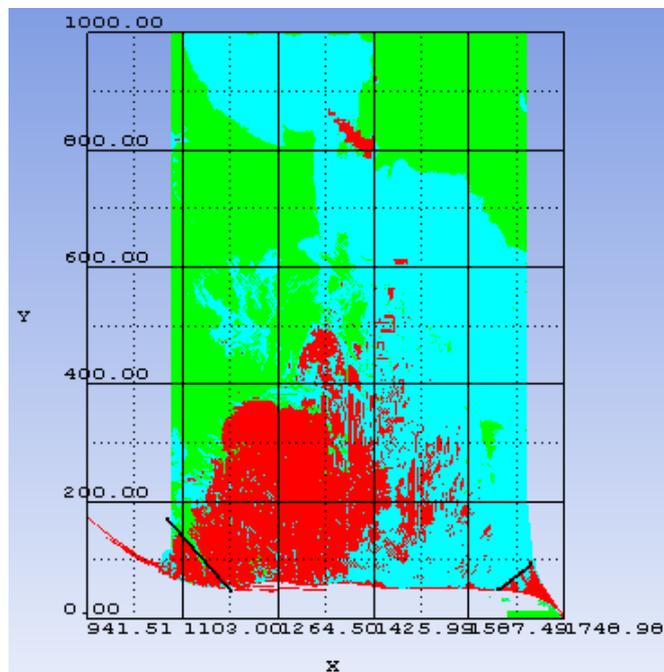
Figure 5.25: Deformed view of the first trial

152

- Second Trial

Table 5.45: Characteristics of the second trial

Trial No	Tensile limit (MPa)	Fracture energy $(\frac{J}{m^2})$	Reheal	Concrete erosion strain	Projectile erosion strain
2	-5.8	13857	No	2	4

Table 5.46: Deformations of the second trial

Front face			Back face		
Crater radius (cm)	Crater depth (cm)	Crater volume (cm^3)	Crater radius (cm)	Crater depth (cm)	Crater volume (cm^3)
17	12	3632	12	8	1206
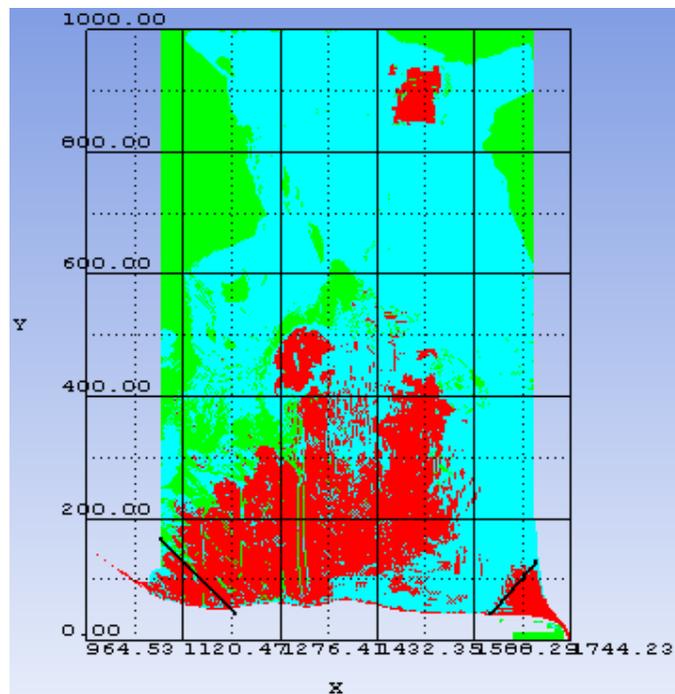
Figure 5.26: Deformed view of the second trial

- Third Trial

Table 5.47: Characteristics of the third trial

Trial No	Tensile limit (MPa)	Fracture energy ($\frac{J}{m^2}$)	Reheal	Concrete erosion strain	Projectile erosion strain
3	-5.8	29000	No	2	4

Table 5.48: Deformations of the third trial

Front face			Back face		
Crater radius (cm)	Crater depth (cm)	Crater volume (cm^3)	Crater radius (cm)	Crater depth (cm)	Crater volume (cm^3)
15	14	3299	10	3	314
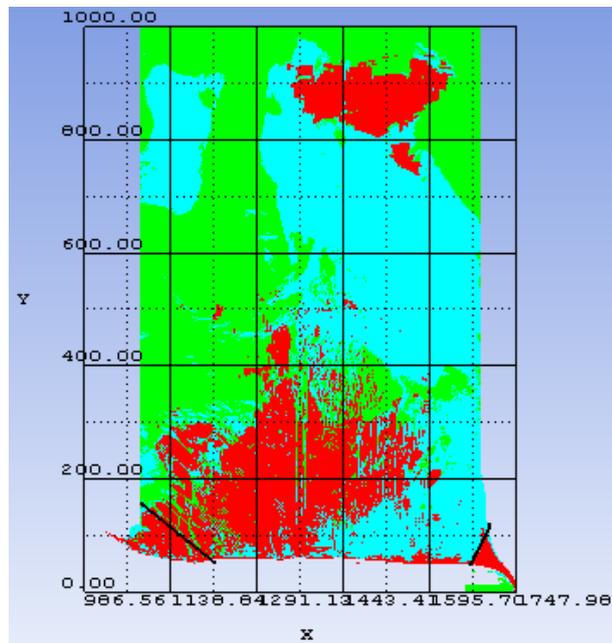
Figure 5.27: Deformed view of the third trial

154

- Fourth Trial

Table 5.49: Characteristics of the fourth trial

Trial No	Tensile limit (MPa)	Fracture energy $(\frac{J}{m^2})$	Reheal	Concrete erosion strain	Projectile erosion strain
4	-8.7	8700	No	2	4

Table 5.50: Deformations of the fourth trial

| Front face			Back face		
Crater radius (cm)	Crater depth (cm)	Crater volume (cm^3)	Crater radius (cm)	Crater depth (cm)	Crater volume (cm^3)
10	3	314	10	17	1780
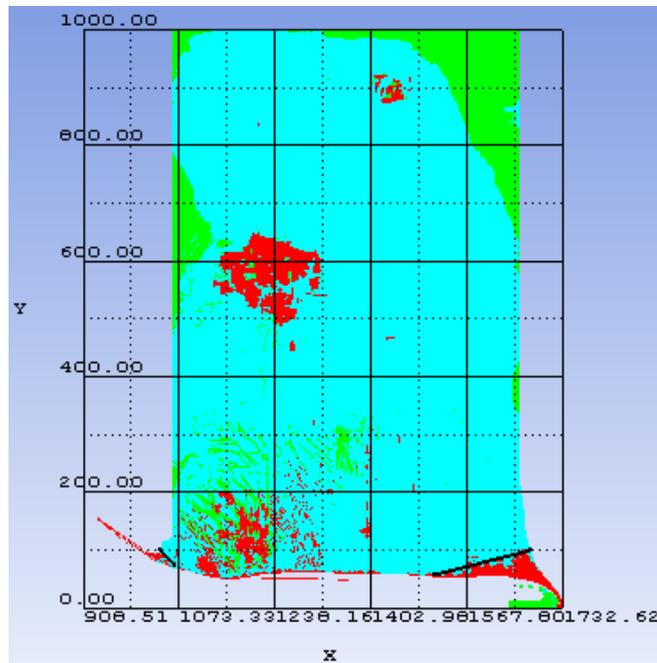
Figure 5.28: Deformed view of the fourth trial

- Fifth Trial

Table 5.51: Characteristics of the fifth trial

Trial No	Tensile limit (MPa)	Fracture energy ($\frac{J}{m^2}$)	Reheal	Concrete erosion strain	Projectile erosion strain
5	-8.7	31000	No	2	4

Table 5.52: Deformations of the fifth trial

| Front face			Back face		
Crater radius (cm)	Crater depth (cm)	Crater volume (cm^3)	Crater radius (cm)	Crater depth (cm)	Crater volume (cm^3)
10	2	209	10	3	314
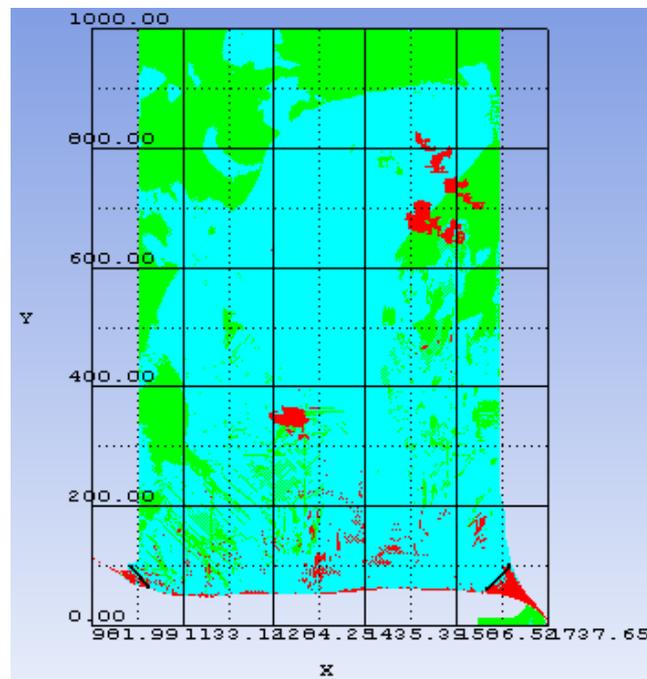
Figure 5.29: Deformed view of the fifth trial

156

- Sixth Trial

Table 5.53: Characteristics of the sixth trial

Trial No	Tensile limit (MPa)	Fracture energy $(\frac{J}{m^2})$	Reheal	Concrete erosion strain	Projectile erosion strain
6	-8.7	43500	No	2	4

Table 5.54: Deformations of the sixth trial

| Front face			Back face		
Crater radius (cm)	Crater depth (cm)	Crater volume (cm³)	Crater radius (cm)	Crater depth (cm)	Crater volume (cm³)
10	3	314	10	14	1466
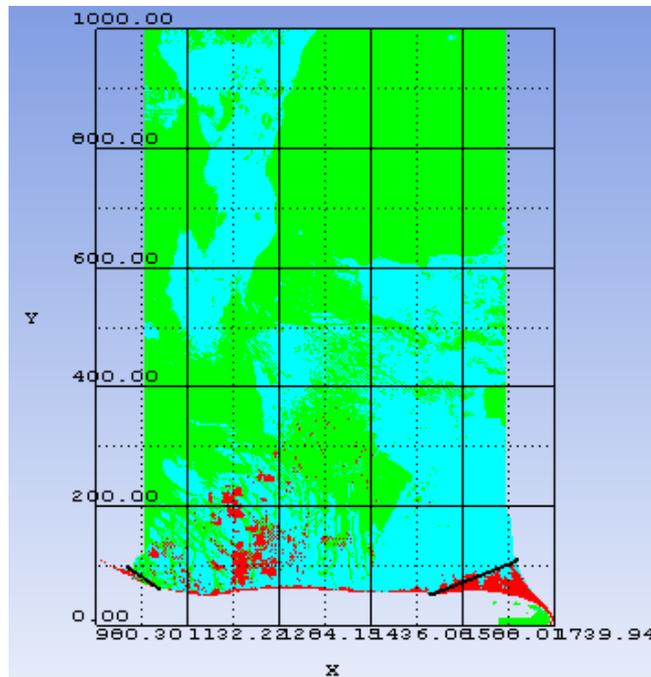
Figure 5.30: Deformed view of the sixth trial

157

5.2.2 Residual Velocities

Under the computational work of the analyses, residual velocities were determined. Results will be given in the same fashion as in the target deformation section according to each group subsequently. Although deformed projectiles of the former simulation were used for the latter ones, the reader should keep in mind that, before each simulation, these velocity initial conditions were set as according to the experimental values.

5.2.2.1 Residual Velocities of the Concrete Group Models

5.2.2.1.1 Residual Velocity for the Specimen 1-3 Model

Values of the residual velocities for trials of the specimen 1-3 are shown in Table 5.55.

Table 5.55: Specimen 1-3 model trails residual velocities

Trial No	Impact velocity (m/s)	Perforation	Residual velocity (m/s)
1	1437	Yes	1256
2	1437	Yes	1163
3	1437	Yes	1253
4	1437	Yes	1252
5	1437	Yes	1167

5.2.2.1.2 Residual Velocity for the Specimen 1-1 Model

Residual velocity result for the specimen 1-1 takes place in Table 5.56.

Table 5.56: Specimen 1-1 model trails residual velocities

Trial No	Impact velocity (m/s)	Perforation	Residual velocity (m/s)
1	1333	Yes	1079

5.2.2.1.3 Residual Velocity for the Specimen 1-2 Model

Results of the residual velocities for trials of the specimen 1-2 are expressed in Table 5.57.

Table 5.57: Specimen 1-2 model trails residual velocities

Trial No	Impact velocity (m/s)	Perforation	Residual velocity (m/s)
1	1143	Yes	860
2	1143	Yes	829
3	1143	Yes	823
4	1143	Yes	843
5	1143	Yes	757
6	1143	Yes	798
7	1143	Yes	792

5.2.2.2 Residual Velocities of the SFRC Group Models

5.2.2.2.1 Residual Velocity for the Specimen 2-2 Model

Residual velocity values for the Specimen 2-2 can be seen in Table 5.58.

Table 5.58: Specimen 2-2 model residual velocity

Trial No	Impact velocity (m/s)	Perforation	Residual velocity (m/s)
1	1450	Yes	1082

5.2.2.2.2 Residual Velocity for the Specimen 2-3 Model

The Specimen 2-3 residual velocity results are shown in Table 5.59.

Table 5.59: Specimen 2-3 model residual velocity

Trial No	Impact velocity (m/s)	Perforation	Residual velocity (m/s)
1	1281	Yes	395

5.2.2.3   Residual Velocities of the SIFCON Group Models

5.2.2.3.1 Residual Velocity for the Specimen 3-2 Model

Residual velocity results for trials of the Specimen 3-2 can be viewed in Table 5.60.

Table 5.60: Specimen 3-2 model trails residual velocities

Trial No	Impact velocity (m/s)	Perforation	Residual velocity (m/s)
1	1450	Yes	1104
2	1450	Yes	1084
3	1450	Yes	1086
4	1450	Yes	1095
5	1450	Yes	1088
6	1450	Yes	1095

5.2.2.3.2 Residual Velocity for the Specimen 3-3 Model

Results of the residual velocities for trials of the Specimen 3-2 are given in Table 5.61.

Table 5.61: Specimen 3-3 model trails residual velocities

Trial No	Impact velocity (m/s)	Perforation	Residual velocity (m/s)
1	1325	Yes	457
2	1325	Yes	475
3	1325	Yes	432
4	1325	Yes	426
5	1325	Yes	494
6	1325	Yes	416

5.3 Results of the Experimental Work

Details of the experimental work in terms of the target contents, reinforcement configurations, general information about the used materials and results of material tests have been given in Chapter 3. The target deformations and the residual velocity outcomes will be given in this section as in the computational results part. However neither images of the deformed specimens nor high speed camera views of the projectiles could be given, since the documents containing these are classified.

5.3.1 Target Deformations

The target deformations in terms of craters' depth, volume and average radius will be given in this section.

5.3.1.1　　Deformations of the Concrete Group Specimens

Experimental results of the concrete group specimens can be viewed in Table 5.62.

Table 5.62: Summary of the concrete group deformation

No	Front face			Back face		
	Average crater radius (cm)	Crater depth (cm)	Crater volume (cm³)	Average crater radius (cm)	Crater depth (cm)	Crater volume (cm³)
1-3	33	14	15966	42.50	13	24590
1-1	43.5	15	29724	50.75	17	45851
1-2	42.5	13	24590	50.50	18	48071

5.3.1.2　　Deformations of the SFRC Group Specimens

The SFRC group specimens' experimental results can be viewed in Table 5.63.

Table 5.63: Summary of the SFRC group deformation

No	Front face			Back face		
	Average crater radius (cm)	Crater depth (cm)	Crater volume (cm³)	Average crater radius (cm)	Crater depth (cm)	Crater volume (cm³)
2-2	24.25	7	4310	37	13	18636
2-3	32.25	9	9802	42.5	16	29909

5.3.1.3   Deformations of the SIFCON Group Specimens

Experimental results of the SIFCON group specimens are shown in Table 5.64.

Table 5.64: Summary of the SIFCON group deformation

No	Front face			Back face		
	Average crater radius (cm)	Crater depth (cm)	Crater volume (cm^3)	Average crater radius (cm)	Crater depth (cm)	Crater volume (cm^3)
3-2	8	4	268	23.5	11	6362
3-3	9.5	5	472	34.25	14	17198

5.3.2   Residual Velocities

Both impact and residual velocities were determined by the aid of high speed camera images. The results are shown in the following sections.

5.3.2.1   Residual Velocities of the Concrete Group Specimens' Projectiles

Projectile residual velocities of the concrete group specimens are given in the Table 5.65.

Table 5.65: Concrete specimens' projectiles residual velocities

No	Impact velocity (m/s)	Perforation	Residual velocity (m/s)
1-3	1437	Yes	1333
1-1	1333	Yes	1143
1-2	1143	Yes	430

5.3.2.2   Residual Velocities of the SFRC Group Specimens' Projectiles

Residual velocities of the SFRC group specimens' projectiles can be seen in the Table 5.66.

Table 5.66: SFRC specimens' projectiles residual velocities

No	Impact velocity (m/s)	Perforation	Residual velocity (m/s)
2-2	1450	Yes	1281
2-3	1281	Yes	1014

5.3.2.3   Residual Velocities of the SIFCON Group Specimens' Projectiles

This group specimens' projectile residual velocities are shown in the Table 5.67.

Table 5.67: SIFCON specimens' projectiles residual velocities

No	Impact velocity (m/s)	Perforation	Residual velocity (m/s)
3-2	1450	Yes	1325
3-3	1325	Yes	1145

5.4   Comparisons

The computational-experimental target deformations and impact velocities are compared in this section.

5.4.1 Comparisons of Target Deformations

Results of the computational target deformations were compared with the experimental ones for each trial of the specimens in terms of crater volume. Ratio of larger result to smaller are shown in the constructed tables. In order to make the reader visualize better, they are given in a graphical form also. The related concrete, SFRC and SIFCON group comparison tables and figures can be seen in the following sections.

5.4.1.1 Comparisons of the Concrete Group

Comparisons for the computational work of Specimens 1-3, 1-1, 1-2 with the experimental ones will be mentioned here.

5.4.1.1.1 Comparison of the Specimen 1-3

Computational deformations of the Specimen 1-3 trials were compared with the outcomes of the experimental one. Results are expressed in a tabular form in the Table 5.68: and in a graphical form in the Figure 5.31.

Table 5.68: Comparison for trials of Specimen 1-3 with the experiment data

Trial No	Crater volume (cm^3) Front face			Crater volume (cm^3) Back face		
	Comp.	Exp.	Exp. / Comp	Comp.	Exp.	Exp. / Comp.
1	5575	15966	2.86	8338	24590	2.95
2	69397	15966	0.23	13609	24590	1.81
3	7200	15966	2.22	12097	24590	2.03
4	3351	15966	4.76	4712	24590	5.22
5	1140	15966	14.00	678	24590	36.27

Comp.= Computational
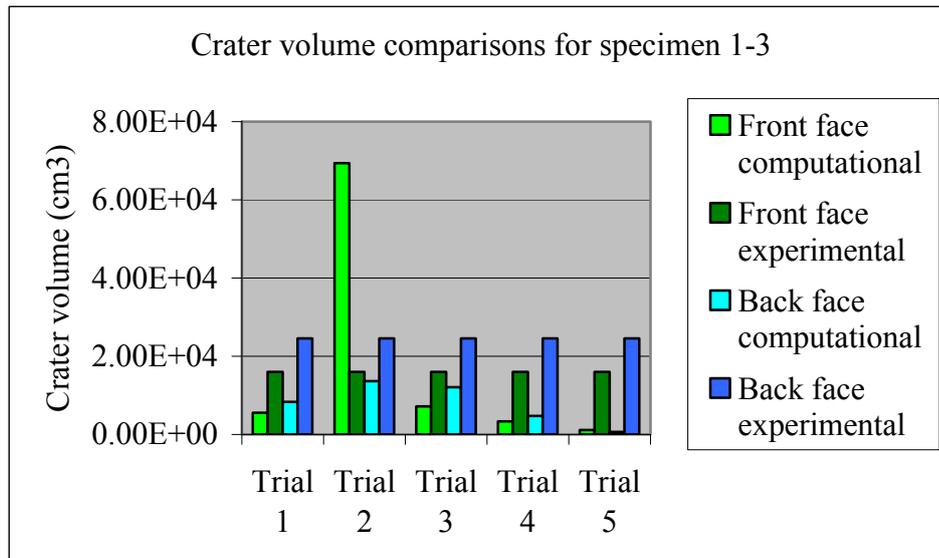
Exp.= Experimental

Figure 5.31: Crater volume comparisons for trials of Specimen 1-3

5.4.1.1.2 Comparison of the Specimen 1-1

Comparison result of the computational deformation of the Specimen 1-1 with the experimental one is given in tabular form in Table 5.69 and graphical form in Figure 5.32.

Table 5.69: Comparison of the Specimen 1-1 with the experiment data

Trial No	Crater volume (cm^3)			Crater volume (cm^3)		
	Front face			Back face		
	Comp.	Exp.	Exp./Comp.	Comp.	Exp.	Exp./Comp.
1	30980	29724	0.96	26540	45851	1.73

Comp.= Computational
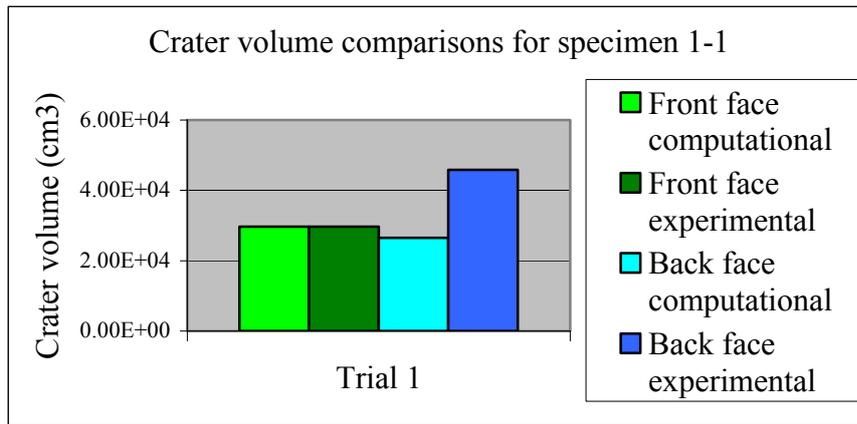
Exp.= Experimental

Figure 5.32: Crater volume Comparisons for Specimen 1-1

5.4.1.1.3 Comparison of the Specimen 1-2

Results of computational deformations of trials of Specimen 1-2 comparisons with the experimental one are expressed tabular form in Table 5.70 and graphical form in Figure 5.33.

Table 5.70: Comparison for trials of Specimen 1-2 with the experiment data

Trial No	Crater volume (cm^3)			Crater volume (cm^3)		
	Front face			Back face		
	Comp.	Exp.	Exp./Comp.	Comp.	Exp.	Exp./Comp.
1	2036	24590	12.08	82467	48071	0.58
2	4608	24590	5.34	3934	48071	12.23
3	3217	24590	7.64	10585	48071	4.54
4	462	24590	53	2714	48071	17.71
5	2724	24590	9.03	2646	48071	18.17
6	1062	24590	23.15	1047	48071	45.91
7	1232	24590	19.96	268	48071	179.37

Comp.= Computational

Exp.= Experimental

167
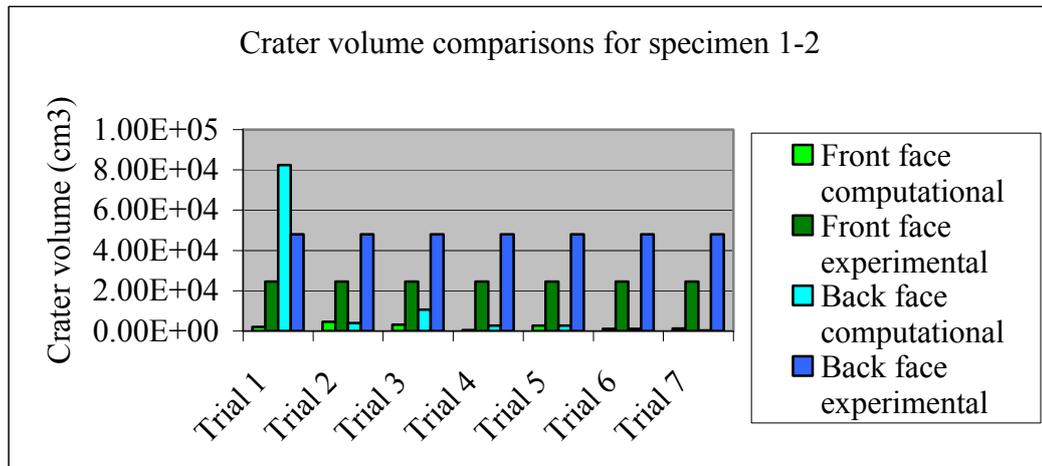
Figure 5.33: Crater volume Comparisons for Specimen 1-2

5.4.1.2 Comparisons of the SFRC Group

Comparison of the computational crater volumes of Specimens 2-2 and 2-3 with the experimental values will be mentioned here.

5.4.1.2.1 Comparison of the Specimen 2-2

Results of the Specimen 2-2 computational deformation comparison with the experimental one are expressed in a tabular form, which is shown in Table 5.71 and in a graphical form as in Figure 5.34.

Table 5.71: Comparison of the Specimen 2-2 with the experiment data

Trial No	Crater volume (cm^3)			Crater volume (cm^3)		
	Front face			Back face		
	Comp.	Exp.	Exp./Comp.	Comp.	Exp.	Exp./Comp
1	205	4310	21.02	1252	18636	14.88

Comp.= Computational

Exp.= Experimental

168
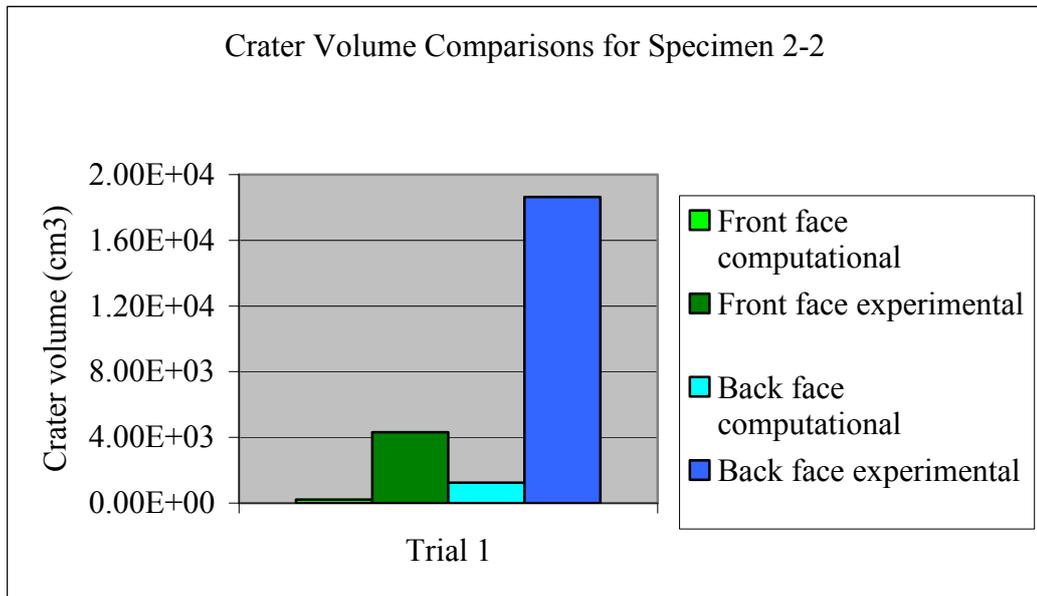
Figure 5.34: Crater volume Comparisons for Specimen 2-2

5.4.1.2.2 Comparison of the Specimen 2-3

The Specimen 2-3 l computational deformation is compared with the experimental one as in Table 5.72 and in Figure 5.35.

Table 5.72: Comparison of the Specimen 2-3 with the experiment data

Trial No	Crater volume (cm^3) Front face			Crater volume (cm^3) Back face		
	Comp.	Exp.	Exp./Comp.	Comp.	Exp.	Exp./Comp.
1	1660	9802	5.90	5445	29909	5.49

Comp.= Computational
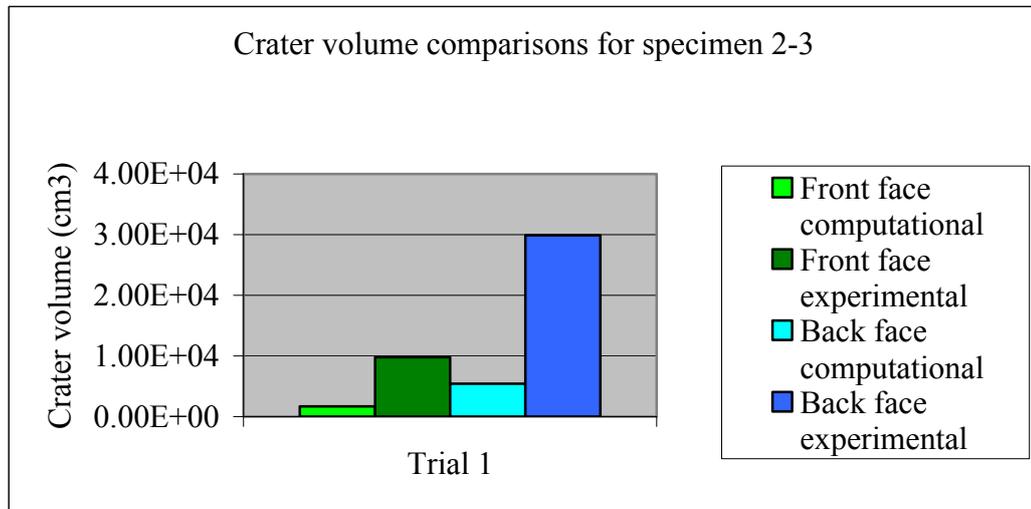
Exp.= Experimental

Figure 5.35: Crater volume Comparisons for Specimen 2-3

5.4.1.3   Comparisons of the SIFCON Group

Comparisons between the computational crater volumes and the experimental ones will be expressed for the Specimens 3-2 and 3-3 in this section.

5.4.1.3.1 Comparison of the Specimen 3-2

Comparison results of the computational deformations of trials of Specimen 3-2 with the experimental one are expressed tabular form in Table 5.73and graphical form in Figure 5.36.

Table 5.73: Comparison for trials of Specimen 3-2 with the experiment data

Trial No	Crater volume (cm³) Front face			Crater volume (cm³) Back face		
	Comp.	Exp.	Exp./Comp.	Comp.	Exp.	Exp./Comp.
1	50	268	5.36	314	6362	20.26
2	67	268	4	419	6362	15.18
3	79	268	3.39	1056	6362	6.02
4	34	268	7.88	1239	6362	5.13
5	50	268	5.36	402	6362	15.83
6	105	268	2.55	339	6362	18.77

Comp.= Computational
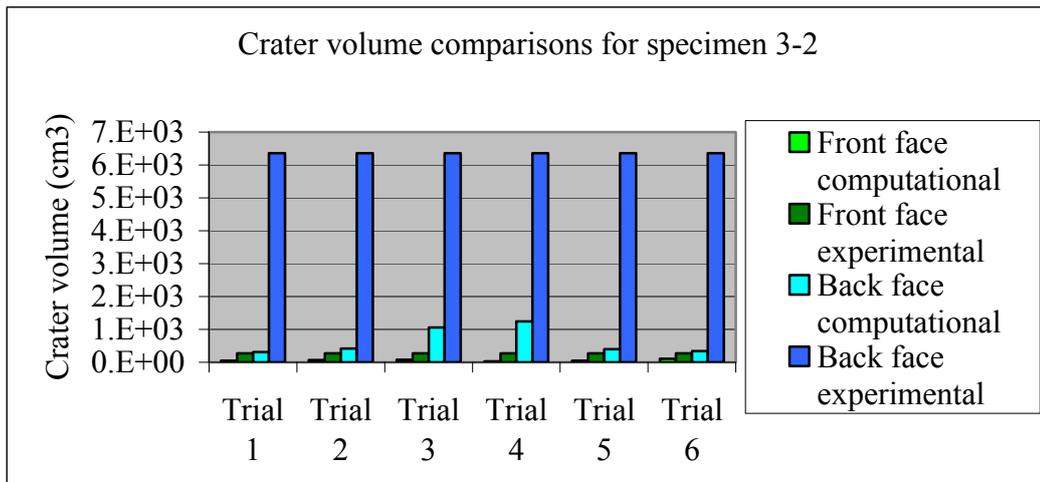
Exp.= Experimental

Figure: 5.36: Crater volume Comparisons for Specimen 3-2

5.4.1.3.2 Comparison of the Specimen 3-3

Comparison results of the computational deformations of trials of Specimen 3-3 with the experimental are given in Table 5.74 and in Figure 5.37.

Table 5.74: Comparison for trials of Specimen 3-3 with the experiment data

Trial No	Crater volume (cm^3) Front face			Crater volume (cm^3) Back face		
	Comp.	Exp.	Exp./Comp.	Comp.	Exp.	Exp./Comp.
1	3732	472	0.13	733	17198	23.46
2	3632	472	0.13	1206	17198	14.26
3	3299	472	0.14	314	17198	54.77
4	314	472	1.50	1780	17198	9.66
5	209	472	2.26	314	17198	54.77
6	314	472	1.50	1466	17198	11.73

Comp.= Computational
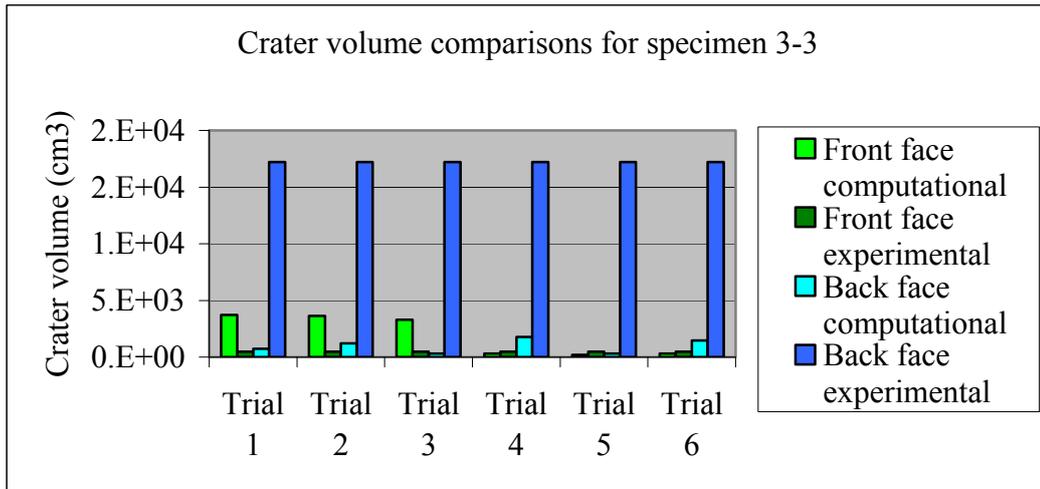
Exp.= Experimental

Figure 5.37: Crater volume Comparisons for Specimen 3-3

5.4.2   Comparison of Residual Velocities

Results of residual velocities gained from computational study of specimen trials were compared to experimental data. Impact velocities in all simulations were identical with the experimental ones. Comparisons are given under concrete, SFRC, SIFCON specimens sections.

5.4.2.1 Comparison of the Concrete Specimens

Residual velocity Comparisons of Specimens 1-1, 1-2, and 1-3 are given in this section.

5.4.2.1.1 Comparison of the Specimen 1-3

Residual velocities comparisons for Specimen 1-3 simulation trials with the experimental value are expressed in Table 5.75. Same outcomes are compared graphically in Figure 5.38.

Table 5.75: Comparison for trials of Specimen 1-3 with the experiment data

Trial No	Comp. residual velocity (m/s)	Exp. residual velocity (m/s)	Exp./Comp.	Comp. velocity loss (%)
1	1256	1333	1.06	12.59
2	1163	1333	1.15	19.08
3	1253	1333	1.06	12.80
4	1252	1333	1.06	12.87
5	1167	1333	1.14	18.79

Comp.= Computational
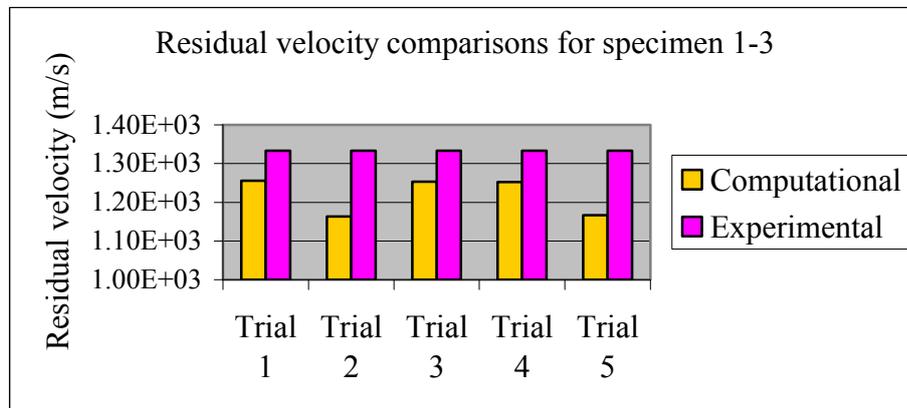
Exp.= Experimental

Figure 5.38: Residual velocity Comparisons for Specimen 3-3

173

5.4.2.1.2 Comparison of the Specimen 1-1

Specimen 1-3 simulation residual velocity comparison with the experimental value is expressed in Table 5.76. Same outcomes were compared graphically in Figure 5.39.

Table 5.76: Comparison for Specimen 1-1 with the experiment data

Trial No	Comp. residual velocity (m/s)	Exp. residual velocity (m/s)	Exp./Comp.	Comp. velocity loss (%)
1	1079	1143	1.06	19.05

Comp.= Computational
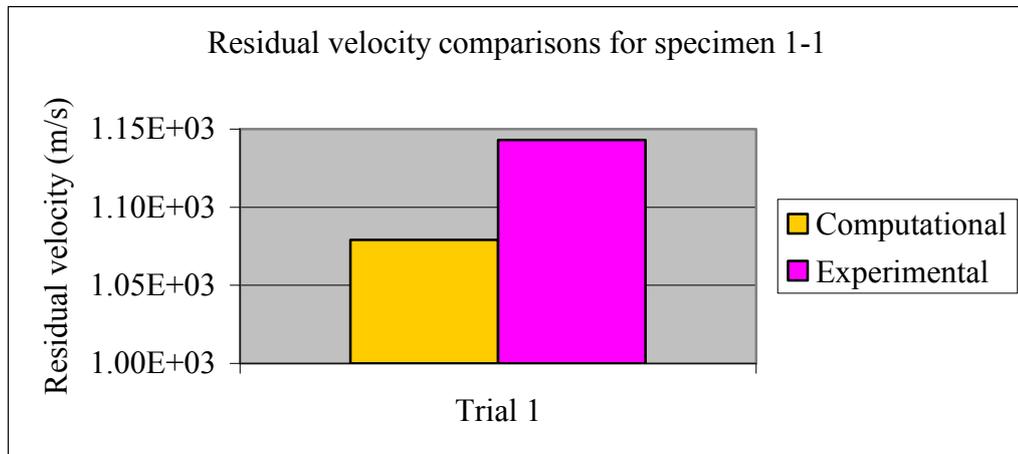
Exp.= Experimental

Figure 5.39: Residual velocity Comparisons for Specimen 1-1

5.4.2.1.3 Comparison of the Specimen 1-2

Comparison of the residual velocities for the Specimen 1-2 simulation trials with the experimental value are expressed in Table 5.77. Outcomes are compared graphically in Figure 5.40 also.

Table 5.77: Comparison for trials of the Specimen 1-2 with the experiment data

Trial No	Comp. residual velocity (m/s)	Exp. residual velocity (m/s)	Exp./Comp.	Comp. velocity loss (%)
1	860	430	0.50	24.76
2	829	430	0.52	27.47
3	823	430	0.52	28.00
4	843	430	0.51	26.25
5	757	430	0.57	33.77
6	798	430	0.54	30.18
7	792	430	0.54	30.71

Comp.= Computational

Exp.= Experimental
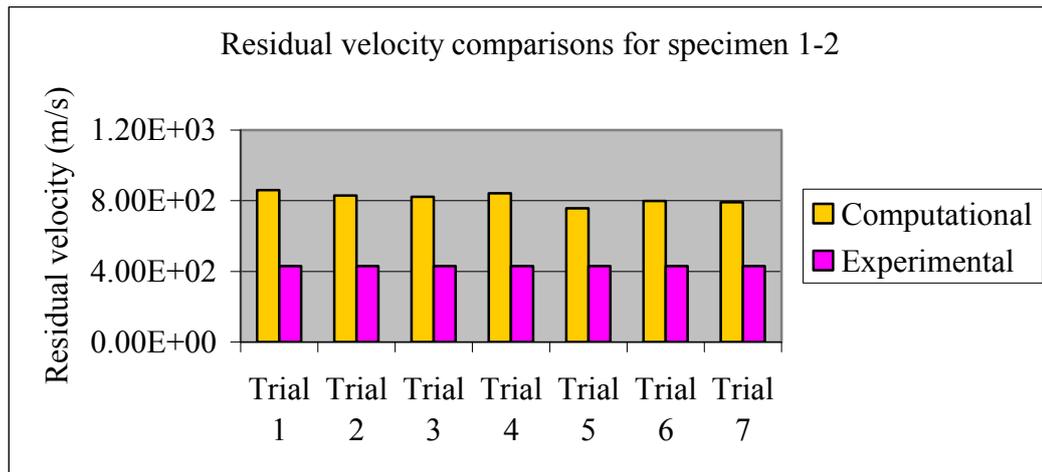
Figure 5.40: Residual velocity Comparisons for Specimen 1-2

175

5.4.2.2 Comparison of the SFRC Specimens

Residual velocity comparisons of the Specimens 2-2 and 2-3 are given in this section.

5.4.2.2.1 Comparison of the Specimen 2-2

Specimen 2-2 simulation residual velocity result was compared with the experimental value. Outcome is expressed in the Table 5.78 and in Figure 5.41.

Table 5.78: Comparison for Specimen 2-2 with the experiment data

Trial No	Comp. residual velocity (m/s)	Exp. residual velocity (m/s)	Exp./Comp.	Comp. velocity loss (%)
1	1082	1281	1.18	25.38

Comp.= Computational
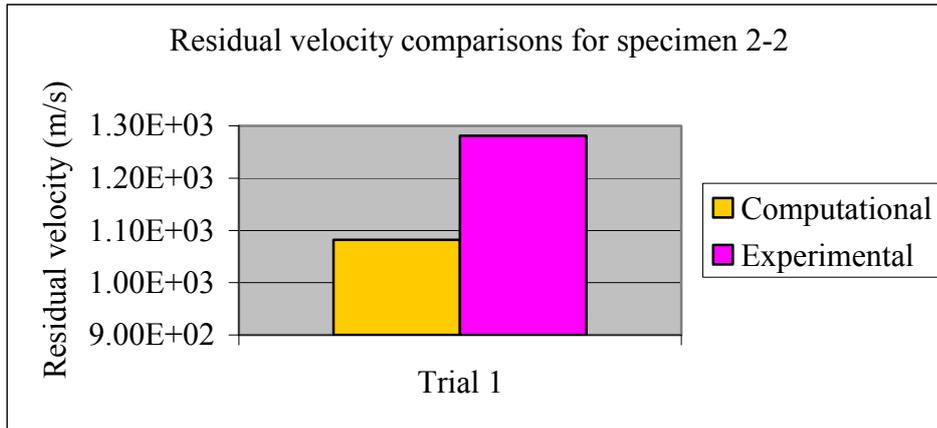
Exp.= Experimental

Figure 5.41: Residual velocity Comparisons for Specimen 2-2

5.4.2.2.2 Comparison of the Specimen 2-3

Comparison of the residual velocity for Specimen 2-3 simulation with the experimental value is expressed in Table 5.79 and in Figure 5.42.

Table 5.79: Comparison for Specimen 2-3 with the experiment data

Trial No	Comp. residual velocity (m/s)	Exp. residual velocity (m/s)	Exp./Comp.	Comp. velocity loss (%)
1	395	1014	2.57	69.16

Comp.= Computational

Exp.= Experimental
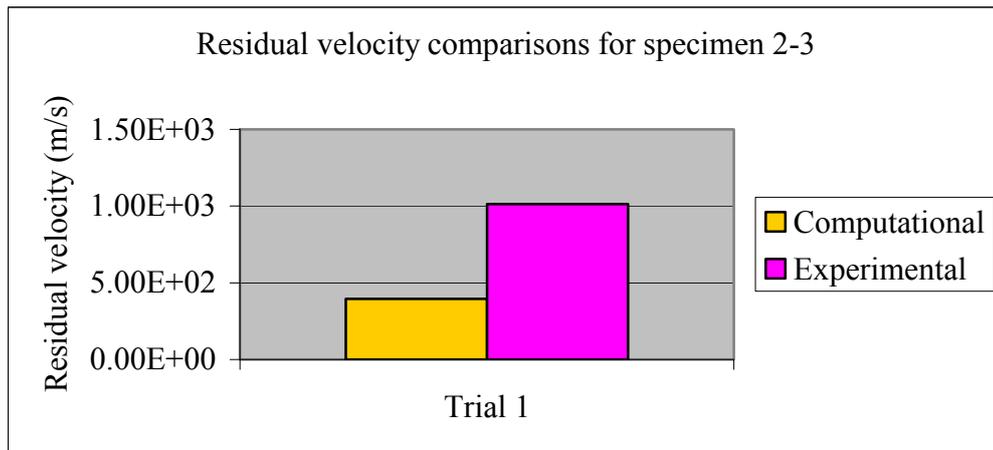
Figure 5.42: Residual velocity comparisons for Specimen 2-3

5.4.2.3   Comparison of the SIFCON Specimens

Residual velocity comparisons of Specimens 3-2 and 3-3 are given in this section.

5.4.2.3.1 Comparison of the Specimen 3-2

Comparison of Specimen 3-2 simulation trials residual velocities with the experimental value are shown in Table 5.80. Results are compared graphically in Figure 5.43.

Table 5.80: Comparison for Specimen 3-2 with the experiment data

Trial No	Comp. residual velocity (m/s)	Exp. residual velocity (m/s)	Exp./Comp.	Comp. velocity loss (%)
1	1104	1325	1.20	23.87
2	1084	1325	1.22	25.24
3	1086	1325	1.22	25.10
4	1095	1325	1.21	24.48
5	1088	1325	1.22	24.97
6	1095	1325	1.21	24.48

Comp.= Computational
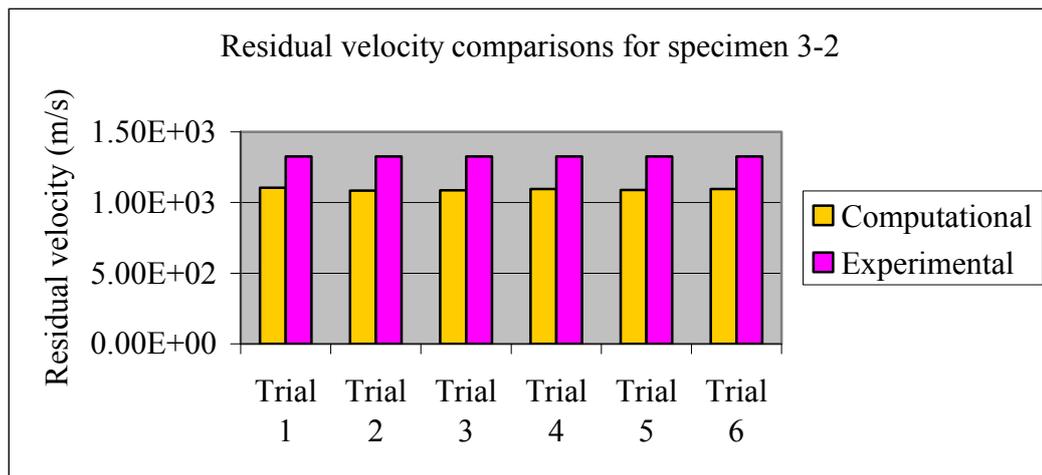
Exp.= Experimental

Figure 5.43: Residual velocity Comparisons for Specimen 3-2

178

5.4.2.3.2 Comparison of the Specimen 3-3

Specimen 3-3 simulation trials residual velocities were compared with the experimental value are expressed in Table 5.81. This can be seen graphically in Figure 5.44 also.

Table 5.81: Comparison for Specimen 3-3 with the experiment data

Trial No	Comp. residual velocity (m/s)	Exp. residual velocity (m/s)	Exp./Comp.	Comp. velocity loss (%)
1	457	1145	2.50	65.51
2	475	1145	2.41	64.16
3	432	1145	2.65	67.40
4	426	1145	2.69	67.85
5	494	1145	2.32	62.72
6	416	1145	2.75	68.60

Comp.= Computational

Exp.= Experimental
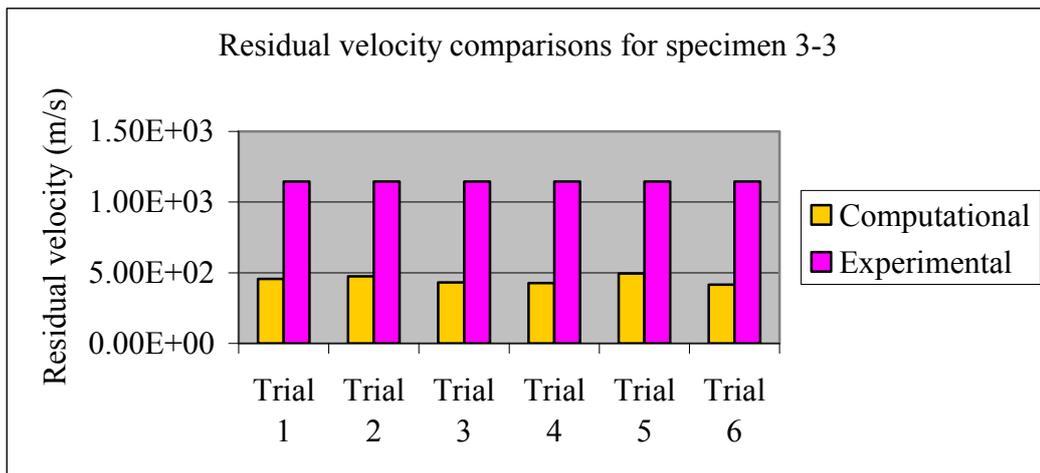
Figure 5.44: Residual velocity Comparisons for Specimen 3-3

5.5   Discussion of the Results

Discussion of the results in terms of target deformation and residual velocities are given in this section subsequently.

5.5.1   Discussion of the Target Deformation Results

Computational results have revealed that, among concrete group models, largest value for crater volume was gained from Specimen 1-1. Average crater volume obtained from Specimen 1-3 was larger than the average crater volume of Specimen 1-2 while it was smaller than Specimen 1-1's related result. Comparison of computational results of concrete group models with the experimental values showed us that, the highest accuracy was gained from Specimen 1-1 of the concrete group. Accuracy of the Specimen 1-3 was poorer than 1-1 and higher than 1-2 except for the comparison of front face crater volume of the Specimen 1-3 second trial. Computed crater volumes for this group of models were generally smaller than the experimental ones.

In SFRC group analyses, crater volume of the Specimen 2-2 was smaller than the crater volume of the Specimen 2-3, while accuracy of the solution belonging to these specimens are is reverse. In the experimental results, Specimen 2-2's crater sizes were also smaller than crater size of Specimen 3-3.

For SIFCON group, analyses have shown that, crater volumes obtained from Specimen 3-2 were smaller than the crater volumes of Specimen 3-3. In this group, simulation models which have tensile strength of -8.7 MPa had better accuracy than the models where concrete tensile strength was -5.8 MPa. In the Specimen 3-2, there was not a significant difference in terms of accuracy between the models and the experimental ones for different tensile strength valued analyses.

Taking into consideration the SIFCON group models with tensile strength of -8.7 MPa and other group of simulation models, it was observed that, SIFCON group models' crater volumes were calculated to be smaller than SFRC ones,

likewise, crater volumes of SFRC group models were smaller than the ones belonging to concrete group model. This behavior was also the same in the experiments.

Reason behind obtaining the poorer accuracy could be not being able to use the specific material data obtained from specimens hence, these tests were not available. During the simulations, in order to model concrete specimen, material data which was found through literature survey and the one that existed in the software material library were used.

5.5.2   Discussion of Residual Velocity Results

General behavior of the residual velocities obtained from simulations was being smaller than the experimental ones. This pattern was different only in Specimen 1-2 of the concrete group. The accuracies of Specimens 1-3 and 1-1 were higher than the ones of Specimens the 2-2 and 2-3 while the accuracy of these specimens were also higher than the ones obtained from Specimens 2-3 and 3-3. Largest error was observed in the Specimen 1-2.

According to the percentage of the velocity losses belonging to computations, highest velocity loss was determined from Specimen 2-3 and 3-3 simulations. These values were larger than the ones observed in Specimen 1-2, 2-2 and 3-2. Minimum velocity loss was gained from Specimen 1-3 and 1-1 residual velocity values.

Looking at the poorer accuracies observed in the residual velocity comparisons, one may conclude that, projectile resistances of targets that took place in the experiments were not as high as the ones belonging to simulations. Higher crater values obtained from experiments also supports this logic.

CHAPTER 6

SUMMARY, CONCLUSION AND SUGGESTIONS FOR FUTURE STUDIES

6.1   Summary

Protective structure design has gained much importance in the past 60 years. Several methods with different materials have been tried in order to increase the resistance of structures to extreme loading. Due to such considerations, the response of reinforced concrete, SFRC and SIFCON specimens to impact loading have been investigated in the experiments supported by TÜBİTAK, under the scope of Project No. 106M497 (Gülkan et al. (2009). However, conducting experiments especially related with the impact loading is a costly issue. Adequate manpower and appropriate conditions are the other necessary parameters for efficient and proper execution of such experiments. Numerical simulations needed to be developed in order to lessen the need of experimental work.

The main objectives of this study were the execution of the computer simulations of the experiments mentioned above, in order to investigate how the change in model parameters would affect the response of the structure in order to increase accuracy and making comparison with the experimental data, furthermore, to check if the constructed model reflects the reality and could be used for the further researches. The aims of the study have been accomplished with success.

In the study of the thesis, the reader was informed in Chapter 2 in a detailed manner about how changes in projectile, impact condition and target

characteristics would affect the ballistic performance. The idea of presenting this chapter was to provide general knowledge about the important impact loading parameters which would be helpful to understand the further sections and conclusions drawn from them.

Experimental work, with which computational studies compared, was explained in the Chapter 3 in a detailed fashion. In this chapter, general information about the materials used for the specimens, the contents of these specimens, material test data gained from them were presented.

The procedure and details of the analyses conducted by using ANSYS AUTODYN Version 11.0 software were given in Chapter 4. Rectangular axisymmetry has been placed by cylindrical axisymmetry in the simulations in the interest of added computational efficiency Brief information about the software used, explicit integration technique, chosen strength, EOS, erosion and failure criteria used to model different materials were explained in a detailed way with their theoretical background in this chapter.

Computational and experimental results were given in Chapter 5. Results of computational work and experimental work were also compared in this section in terms of both target deformations and residual velocity of the projectiles used in them.

6.2   Conclusions

Conclusions drawn from computational results and comparison of experimental values with them are given hereunder in two parts: Conclusions Concerning Target Deformations and Conclusions Concerning Residual Velocities sections.

6.2.1   Conclusions Concerning Target Deformations

Comparison of computational and experimental results indicates the following as conclusions:

- Concrete compressive strength had a great influence on target deformation. Higher concrete strength resulted in smaller target deformation.

- Tensile strength of the concrete was the most dominant parameter that affects the pattern of the deformation and crater size. Higher tensile strength resulted in smaller concrete deformation.

- Change in erosion parameters of projectile and target did not have a significant effect on crater size but it may alter the general pattern of target deformation significantly. Moderate erosion values for concrete instead of higher ones are suggested.

- Magnitude of the fracture energy played a very small role in both general deformation and crater size of the deformed concrete target.

- Generally crater volumes for concrete specimens were higher than SFRC group crater volumes and these values were higher than those for SIFCON specimens. This observation was valid for both experiments and simulations.

- The ratios of experimental to computational results were generally large. Among all simulations, highest accuracy was obtained from the computations where Concrete-L model was used for the targets.

- Poorer accuracy belonging to comparisons may result from not being able to use more specific material data for the computations.

6.2.2 Conclusions Concerning Residual Velocities

Comparisons and analyses results have shown that:

- The change in erosion parameters of target and projectile played an important role in the magnitude of residual velocity.

- Target material tensile limit change seemed to have an insignificant effect on residual velocity.

- Residual velocities obtained from the computations of different target specimens in which only fracture energy differed, came out to be approximately the same.

- Velocity losses obtained from computations were generally larger than the experimental ones which show that in the simulations, targets were more difficult to perforate than the experimental ones.

- Use of concrete target with higher strength resulted in higher percentage of velocity loss.

- In terms of the accuracy, the highest values were obtained from Concrete-L model used simulations.

- Velocity loss percentages were smallest in simulations that employed the Concrete-L model.

6.3   Recommended Future Studies

- Other concrete models in the AUTODYN library might be modified for additional simulations for improved results.

- Analyses could be extended to include strain rate effects.

- Improved material tests could be conducted to gain the required input parameters for the specific materials used in the simulations.

- User defined materials could be created and implemented in the simulations.

- Other software besides LS-DYNA might be used for the computations by the implementation of user defined material data.

REFERENCES

Anderson C.E.,Walker J.D., (1996), On the L/D effect for long-rod penetrator, International Journal of Impact Engineering, Vol. 18, No. 3, 247-264.

Anderson Jr. C.E., Hohler V., Walker J.D., Stilp A.J., (1999), The influence of projectile hardness on ballistic performance, International Journal of Impact Engineering, Vol. 22, No. 6, 619-632.

Anderson J.L.B., Schultz P.H., (2005), The Effect of Projectile Density and Disruption on the Crater Excavation Flow-Field, 36th Annual Lunar and Planetary Science Conference, March 14-18, League City, Texas, abstract no.1773.

ACI 544, (1996), State-of-the-Art Report on fibre Reinforced Concrete. ACI Committee 544 Report 544.1R-96, American Concrete Institute, Detroit, 66 pp.

AUTODYN (2007), AUTODYN –Help Menu, ANSYS Release 11.0 Documentation for ANSYS Workbench, Century Dynamics Inc., Concord. CA. USA.

AUTODYN Theory Manual, (2005), Century Dynamics Inc., Concord.CA.,USA.

Bainbridge P., (1988), World Impact Data–S.R.D. Impact Database Version Pre 3i, CCSD/CIWP (88)107(P).

Bentur A., Mindess S., (2006), Fibre Reinforced Cementitious Composites, Spon Press.

Barros J. A. O., Figueiras J. A.,(1999), Flextural Behavior of SFRC: Testing and Modelling., J. Mat. in Civ. Engrg. Vol. 11, No. 4, pp. 331-339.

Chinella J.F., Pothier B., Wells M.G.H., (1998), Processing, Mechanical Properties and Ballistic Impact Effects of Austempered Ductile Iron, ARL-TR-1741,Army Research Laboratory.

Chanh N.V., (2005), Steel Fibre Reinforced Concrete, The JSCE (Japan Society of Civil Engineers),VIFCEA (Viet Nam Federation of Civil Engineering Associations),Joint Seminar on Concrete Engineering in Ho Chi Minh City University of Technology.

Chen W.F., (1982), Plasticity in Reinforced Concrete, McGraw-Hill Inc., USA

Dancygier A.N., (1997), Technical note-Effect of reinforcement ratio on the resistance of reinforced concrete to hard projectile impact, Nuclear Engineering and Design, 172, 233-245.

Dancygier A.N., (1998), Rear face damage of normal and high-strength concrete elements caused by hard projectile impact, ACI Structural Journal, Vol.95, No. 3, 291–304.

Daneshjou K., Kochakinejad A., Rahimzadeh M., (2005), Numerical Study of Long Rods Penetration Depth in Semi-Infinite Targets in Electromagnetic Launchers-IEEE Transactions on Magnetics, Vol. 41, No. 1, 375-379.

Dramix RC-80/60-BN, (2005), Product Data Sheet, N.V. Bekaert S.A.

Dramix RL-45/30-BN, (2005), Product Data Sheet, N.V. Bekaert S.A.

Drucker D.C., Gibson R.E., Henkel D.J., (1975), Soil Mechanics and Work Hardening Theories of Plasicity, Trans. ASCE, Vol. 122, 338-346.

Drucker D.C., Prager W., (1952), Soil Mechanics and Plastic Analysis or Limit Design, Q. Appl. Math., Vol. 10, No. 2, 157-165).

Ersoy U., Özcebe G., Tankut T., (2004), Reinforced Concrete, Middle East Technical University, Ankara, Turkey.

Ezeldin, A. S., and Balaguru, P. N. (1992). ''Normal and high-strength fiber reinforced concrete under compression.'' J. Mat. in Civ. Engrg.,ASCE, 4(4), 415–429.

Forrestal M.J., Altman B.S., Cargile J.D., Hanchak, S.J., (1994), An empirical equation for penetration depth of ogive-nose projectiles into concrete targets.'' International Journal of Impact Engineering, Vol. 15, No. 4, 395–405.

Fanella, D. A., Naaman, A. (1985), Stress-strain properties of fiber reinforced mortar in compression. ACI J., 82(4), 475–483.

Goldsmith W. (1960), Impact: Theory and Physical Behavior of Colliding Solids, Edward Arnold, London.

Grabarek C.L., (1971), Penetration of armor by steel and high density penetrators BRL MR 2134, Ballistic Research Laboratories, Aberdeen Proving Ground, MD.

Grabarek, C., (1973), Joint Technical Coordinating Group for Munitions Effectiveness, JTCG/ME Working Party for KE Penetrators, Information Exchange Meeting, Ballistic Research Laboratories, Aberdeen Proving Ground, MD, 13-14 February, U.S.A.

Gülkan, P., Tokyay M., Binay S., Korucu H., (2009), TÜBİTAK Report Project No: 106M497, Research on the endurance of buildings constructed with high-performance cement-based composites vis-à-vis the impact caused by conventional weapons, (Yüksek Performanslı Çimento Esaslı Kompozitlerle Insa Edilen Yapıların Konvansiyonel Silah Etkilerine Karsı Dayanıklılığının Arastırılması), Ankara, Turkey .

Gylltoft K., (1983), Fracture mechanics models for fatigue in concrete structures, Doctoral Thesis, Department of Structural Engineering, Lulea University of Technology, Lulea(Sweden), No. 1983:25:D, 210pp.

Hanchak S.J., Forrestal M.J., Young E.R., Ehrgfott J.Q., (1992), Perforation of concrete slabs with 48 MPa (7 ksi) and 140 MPa (20 ksi) unconfined compressive strength, International Journal of Impact Engineering, Vol. 12, No. 1, 1–7.

Hiermaier S.J., (2008), Structures Under Crash and Impact, Springer Science+Business Media, USA.

Klinkrad H.(2006), Space Debris: Models and Risk Analysis, Springer Praxis Books / Astronautical Engineering, Kindle Edition.

Khan W.U., Ansari R., Gupta N.K., (2003), Normal and Oblique Impacts of Hard Projectile on Single and Layered Plates-An Experimental Study-Defence Science Journal, Vol. 53, No. 2,139-146.

Lambert, J.P., Jonas, G.H., (1976), Ballistic Research Laboratory, BRL-R-1852 (ADA021389).

Lambert, J. P., (1978), Ballistic Research Laboratory, ARBRL-TR-02072.

Li Q.M., Chen X.W., (2003), Dimensionless formulae for penetration depth of concrete target impacted by a non-deformable projectile, International Journal of Impact Engineering, Vo. 28, No. 1, 93–116.

Li, Q.M., Reid S.R., Ahmad-Zaidi A.M., (2006), Critical impact energies for scabbing and perforation of concrete target, Nuclear Engineering and Design, Vol. 236, No.11, 1140–1148.

Li Q.M., Tong D.J., (2003), Perforation Thickness and Ballistic Limit of Concrete Target Subjected to Rigid Projectile Impact, Journal of Engineering Mechanics, Vol. 129, No. 9,1083-1091.

Lia Q.M.,Reida S.R., Wenb H.M.,Telford A.R., (2005), Local impact effects of hard missiles on concrete targets, International Journal of Impact Engineering, Vol. 32, No. 1-4, 224–284].

Li V.C., Backer S., Wang Y., Ward R., Green E., (1989), Toughened Behavior and Mechanisms of Synthetic Fiber Reinforced Normal Strength and High Strength Concrete. Fiber Reinforced Cements and Concretes: Recent Developments. International Conference, Sept. 18-20, University of Wales College, Cardiff, U.K.; Ed. by R.N. Swamy and B. Barr, Elsevier Applied Science, London, 420-433.

Löfgren I., (2005), Fibre-Reinforced Concrete for Industrial Construction- a Fracture Mechanics Approach to Material Testing and Structural Analysis, Doctoral Thesis, Department of Civil and Environmental Engineering, Division of Structural Engineering, Chalmers University of Technology, Göteborg (Sweden), 243 pp.

Lamond J., Pielert J.,(2006), STP 169D -Significance of Tests and Properties of Concrete and Concrete-Making Materials, ASTM International.

Marchand K.A.,Nash P.T., Cox P.A., (1998), Tests and Analysis of the Localized Response of Slurry Infiltrated Fibre Concrete (SIFCON) AND Conventional Reinforced Concrete (CRC) Subjected to Blast and Fragment Loading, Journal de Physique Colloque C3, Supplement au n09, Tome 49.

Madhu V.,Balakrishna Bhat T.Gupta N.K., (2003), Normal and Oblique Impacts of Hard Projectile on Single and Layered Plates-An Experimental Study-I, Defence Science Journal, VoI. 53, No. 2, 147-156.

NDRC, (1946), Effects of Impact and Explosion, Summary Technical Report of Division 2, Vol. 1, National Defence Research Committee, Washington, DC.

Naaman A.E., Reinhardt H.W., Fritz C., Alwan J., (1993), Non-linear analysis of RC beams using a SIFCON matrix Materials and Structures,26, 522-531.

Nyström U., (2008), Concrete Structures Subjected to Blast and Fragment Impacts, Licentiate thesis, Department of Civil and Environmental Engineering, Structural Engineering, Concrete Structures, Chalmers University of Technology, Göteborg (Sweden), 117 pp.

Nyström U., Gylltoft K. (2008), Comparative Numerical Studies of Projectile Impacts on Plain and Steel-Fibre Reinforced Concrete,Proceedings Nordic Concrete Research, Bålsta, Sweden, 198-199. ISBN/ISSN: 978-82-8208-007-1 Nr. 78252.

Phillabaum II R.A., Schraml S.J., Summers S.J., Sorensen Brett R., (2008), Consideration of Nose Shape for Thin-Walled Projectile Penetrating Double Reinforced Concrete, ARL-RP-215, U.S. Army Research Laboratory.

Rao H.S., Ghorpade V.G., Ramana N.V., Gnaneswar K., (2009), Response of SIFCON two-way slabs under impact loading, International Journal of Impact Engineering, In Press, Corrected Proof, Available online 13 June 2009.

Reid S.R., Wen H., (2001), Predicting penetration, cone cracking, scabbing and perforation of reinforced concrete targets struck by flat-faced projectiles,UMIST Report ME/AM/02.01/TE/G/018507/Z.

Schultz P.H., (2003), Transient Crater Growth in Low Density Targets, 34th Annual Lunar and Planetary Science Conference, March 17-21, League City, Texas, abstract no.2067.

Tham C.Y., (2005), Reinforced concrete perforation and penetration simulation using AUTODYN-3D, Finite Elements in Analysis and Design, Vol. 41, No. 14, 1401–1410.

Tham C.Y., (2006), Numerical and empirical approach in predicting the penetration of a concrete target by an ogive-nosed projectile, Finite Elements in Analysis and Design, Vol. 42, No. 14-15, 1258-1268.

TM 5-855-1, (1984), Fundamentals of Protective Design for Conventional Weapons, Department of the Army, Washington, DC, USA.

TM 5-855-1, (1986), Fundamentals of Protective Design for Conventional Weapons, Department of the Army, Washington, DC, USA.

TS 708 , (1996), Steel Bars for Concrete, Turkish Standards Institute, Ankara, Turkey.

Ugural A.C., Fenster S.K., (2003), Advanced Strength and Applied Elasticity, Prentice Hall, USA.

Vedantam K., Bajaj D., Brar1 N.S., Hill S., (2006), Johnson-Cook Strength Models for Mild and DP 590 Steels, Shock Compression of Condensed Matter – 2005, Proceedings of the Conference of the American Physical Society Topical Group on Shock Compression of Condensed Matter, AIP Conference Proceedings, Vol. 845, 775-778.

Warrick R.J., Althoff P., Druschitz A.P.,Lemke J.P., Zimmerman K., Mani P.H., Rackers M.L., (2000), Austempered Ductile Iron Castings for Chassis Applications, SAE 2000 World Congress Detroit, Michigan,U.S.A., March 6–9.

Yankelevsky D.Z., (1997), Local Response of Concrete Slabs to Low Velocity Missile Impact, International Journal of Impact Engineering, Vol. 19, No. 4, 331 343.

Zukas J.A., Nicholas T., Swift H.F., Greszczuk L.B., Curran D.R., (1982), Impact Dynamics, John Wiley & Sons, Inc., U.S.A.

Zukas J.A., (2004), Introduction to Hydrocode, Elsevier Ltd., UK.